



THE HONG KONG  
POLYTECHNIC UNIVERSITY

香港理工大學

Pao Yue-kong Library

包玉剛圖書館

---

## Copyright Undertaking

This thesis is protected by copyright, with all rights reserved.

**By reading and using the thesis, the reader understands and agrees to the following terms:**

1. The reader will abide by the rules and legal ordinances governing copyright regarding the use of the thesis.
2. The reader will use the thesis for the purpose of research or private study only and not for distribution or further reproduction or any other purpose.
3. The reader agrees to indemnify and hold the University harmless from and against any loss, damage, cost, liability or expenses arising from copyright infringement or unauthorized usage.

### IMPORTANT

If you have reasons to believe that any materials in this thesis are deemed not suitable to be distributed in this form, or a copyright owner having difficulty with the material being included in our database, please contact [lbsys@polyu.edu.hk](mailto:lbsys@polyu.edu.hk) providing details. The Library will look into your claim and consider taking remedial action upon receipt of the written requests.

**OPTICAL FIBRE SENSORS FOR FLOW  
AND PRESSURE MEASUREMENT IN  
HARSH ENVIRONMENT**

**CHO LOK HIN**

**Ph.D**

**The Hong Kong Polytechnic University**

**2014**

The Hong Kong Polytechnic University

Department of Electronic and Information Engineering

**Optical Fibre Sensors For Flow And Pressure  
Measurement in Harsh Environment**

CHO LOK HIN

A thesis submitted in partial fulfillment of the requirements for  
the degree of Doctor of Philosophy

March 2014

## CERTIFICATE OF ORIGINALITY

I hereby declare that this thesis is my own work and that, to the best of my knowledge and belief, it reproduces no material previously published or written, nor material that has been accepted for the award of any other degree or diploma, except where due acknowledgement has been made in the text.

\_\_\_\_\_ (Signed)

\_\_\_\_\_ CHO, LOK HIN \_\_\_\_\_ (Name of student)

## **Abstract**

Optical fibre sensor can work in harsh environments, which makes it an ideal candidate for many industrial applications. Flow and pressure sensor are two important types of sensors for oil and gas industry to monitor and control the production of their products. The temperature can reach as high as 200°C and located hundreds of meters or even over a kilometer away from the measuring devices. In these applications, remote and harsh environment are often the conditions that the sensors are working in. In this thesis, a number of schemes for implementing thermal anemometer for flow measurement and pressure sensor are proposed and investigated experimentally and theoretically.

The proposed fibre optic thermal anemometer has a pure silica structure, which has never been reported before. Pure silica structure makes it possible for the sensor to work in harsh environment like elevated temperature and corrosive gas measurement. The pure silica structure also makes the sensor structure simpler, making it easier to be fabricated.

The sensor is based on a section of high absorption fibre that absorbs the pumping laser light carried in the core and convert it into thermal energy. As the flow rate of the fluid changes, the rate of convective heat transfer changes and so the temperature of the sensor varies. A pumping laser with constant power output is required. A fibre Bragg grating (FBG) is inscribed in the section of the high absorption fibre to measure the temperature variation. By measuring the temperature of the sensor, the flow rate of the fluid can be found. Other than flow rate, ambient temperature and optical power absorption also affect the measured temperature. Fluctuation of these

two parameters causes measurement errors. Another method is proposed to reduce the sensor's dependency on those two parameters. Instead of applying constant optical power, the pump laser output is modulated on and off. Measuring the time constant of the falling temperature of the sensor when the pumping laser output is off, the flow rate of the fluid can be found. This method is proved to be much less sensitive to absorbed optical power and ambient temperature change. One drawback of such operation is that it only measures the average flow speed during a period of time while constant power operation can tell the instant flow speed. Serial multiplexing of the sensors is realized by shifting the FBGs' wavelength to around 850 nm where the attenuation is low. Multiplexing of three sensors has been realized successfully experimentally.

Another sensor studied in the thesis is a Sagnac-loop based pressure sensor. The fibre used is Blaze Photonics PM-1550-01 polarization maintaining photonic crystal fibre (PM-PCF). The benefit of such design is the low temperature sensitivity. By changing the operation wavelength to 850 nm comparing with previous proposed schemes of operating at 1550 nm, simulation and experimental studies have shown that much higher sensitivity can be achieved. Moving to 850 nm can also enable the use of low cost CCD based optical fibre interrogator. This potentially enables much higher measurement speed and lower system cost comparing with system operating at 1550 nm. Instead of measuring the spectral shift of the sensor's transmission spectrum as in the previous studies, the phase change of the sinusoidal waveform like spectrum obtained from a CCD optical fibre interrogator is employed for pressure measurement. This method enables constant sensitivity to be sustained throughout the whole measurement range. The proposed new method also offers slightly better accuracy than previous proposed spectral shift technique.

## **Acknowledgement**

Thanks to my parents for their life long support throughout my whole study

I would like to express appreciation to my chief supervisor, Prof. Chao Lu, and also Prof. Hwa-Yaw Tam for their guidance and support throughout my PhD study. Also, I appreciate the help from all the colleagues in the research team for their selfless support and help.

Finally, I would like to thank the Research Grant Council of the Hong Kong Government for the financial support during my research study.

# Table of Contents

<b>ABSTRACT</b> .....	<b>I</b>
<b>ACKNOWLEDGEMENT</b> .....	<b>I</b>
<b>TABLE OF CONTENTS</b> .....	<b>1</b>
<b>LIST OF FIGURES</b> .....	<b>3</b>
<b>CHAPTER 1 INTRODUCTION</b> .....	<b>9</b>
1.1 BACKGROUND .....	9
1.2 OBJECTIVES.....	10
1.3 THESIS OUTLINE .....	13
1.4 CONTRIBUTED PUBLICATIONS .....	14
<b>CHAPTER 2 LITERATURE REVIEW</b> .....	<b>15</b>
2.1 FIBRE BRAGG GRATING .....	15
2.1.1 <i>Introduction</i> .....	15
2.1.2 <i>Background</i> .....	16
2.1.3 <i>Thermal Decay</i> .....	19
2.2 FLOW MEASUREMENT .....	26
2.2.1 <i>Introduction</i> .....	26
2.2.2 <i>Non Fibre optics flowmeter</i> .....	27
2.2.3 <i>Fibre optic flowmeter</i> .....	35
2.3 SAGNAC INTERFEROMETER .....	41
2.4 FIBRE OPTIC PRESSURE SENSOR.....	44
2.5 CONCLUSIONS .....	53
<b>CHAPTER 3 FIBRE OPTIC THERMAL ANEMOMETER</b> .....	<b>54</b>

3.1 INTRODUCTION.....	54
3.2 FABRICATION AND STRUCTURE OF THE SENSOR.....	56
3.3 EXPERIMENT DESIGN AND RESULTS.....	58
3.4 EQUATION DEVELOPMENT.....	63
3.5 THERMAL DECAY OF THE SENSOR.....	79
3.5 WATER FLOW MEASUREMENT.....	82
3.6 CONCLUSIONS.....	87
<b>CHAPTER 4 REDUCING POWER/TEMPERATURE DEPENDENCY AND MULTIPLEXING OF THE FIBRE OPTIC THERMAL ANEMOMETER ....</b>	<b>89</b>
3.1 INTRODUCTION.....	89
4.2 EQUATIONS FOR PULSE OPERATION.....	90
4.3 SIMULATION AND EXPERIMENTAL RESULTS.....	96
4.4 SERIAL MULTIPLEXING.....	98
4.5 CONCLUSIONS.....	103
<b>CHAPTER 5 HIGH SENSITIVITY AND LOW COST SAGNAC LOOP BASED PRESSURE SENSOR.....</b>	<b>104</b>
5.1 INTRODUCTION.....	104
5.2 PRINCIPLE.....	105
5.3 EXPERIMENTAL SETUP.....	109
5.4 EXPERIMENTAL RESULTS.....	110
5.5 CONCLUSIONS.....	122
<b>CHAPTER 6 CONCLUSIONS &amp; FUTURE WORKS.....</b>	<b>123</b>
6.1 CONCLUSIONS.....	123
6.2 FUTURE WORKS.....	127
<b>REFERENCES.....</b>	<b>129</b>

## List of Figures

Figure 2.1. Fiber Bragg Grating.....	18
Figure 2.2. Physical model of a) electrons excited by UV are trapped in continuous distribution of traps; b) shallow traps ( $E < E_d$ ) is emptied and deeper traps remain full by thermal depopulation at a given temperature and time.....	20
Figure 2.3. Measured normalized integrated coupling constant of 2 gratings heated to 350°C and 550°C. [14].....	21
Figure 2.4. (a) Power law factor A obtains by curve fitting. (b) Power law factor $\alpha$ obtained by curve fitting [14].....	22
Figure 2.5. Normalized integrated coupling coefficient $\eta$ as a function of the demarcation energy $E_d$ . [14].....	23
Figure 2.6. Decay of grating first at 350 °C then 550 °C [14].....	24
Figure 2.7. (a) A against T and (b) $\alpha$ against of a weak grating [15].....	25
Figure 2.8. Comparison between aging curve approach and power law approach for accelerated aging. Continuous line: Aging curve approach. Dotted line: Power law approach. Square: Experimental results. [15] .....	25
Figure 2.9. Graphical illustration of a drag body flowmeter.....	28
Figure 2.10. Graphical illustration of a vortex flowmeter .....	29
Figure 2.11. Ultrasound time-of-flight flowmeter .....	31
Figure 2.12. Basic hot-wire anemometer [25] .....	33
Figure 2.13. Typical optical configuration of laser Doppler anemometer [31] .....	36
Figure 2.14. Optical setup of PM-PCF based LDA. (1) laser with polarized output; (2) 50/50 beam splitter; (3) Bragg cell; (4) 90° polarisation rotator; (5) polarization beam splitter; (6) beam compressor; (7) micro lens; (8) single mode	

polarization maintaining fibre; (9) polarization beam splitter; (10) measuring volume; (11) receiving multimode fibre; (12) filter; (13) photomultiplier. [32]	36
Figure 2.15. Electric wind measurement with CO <sub>2</sub> laser heating the fibre optic Mach-Zehnder interferometer [41]	39
Figure 2.16. Experimental setup of silver coated self-heating FBG sensors for liquid level and temperature measurement [42]	40
Figure 2.17. Basic sagnac interferometer in free space.	42
Figure 2.18. Cross section of the PM-PCF analyzed in [58]. Structure B was produced by Blaze Photonics Inc [59].	48
Figure 2.19. Calculated group and phase modal birefringence at different wavelength [59].	48
Figure 2.20. (a) (b) Pressure sensitivity of phase and group modal birefringence of structure A; (c)(d) Pressure sensitivity of phase and group modal birefringence of structure B [59].	49
Figure 2.21. Experimental results of the PCF's phase and modal birefringence at different wavelength [60].	50
Figure 2.22. Experimental results on pressure sensitivity of (a) phase (b) group modal birefringence at different wavelength [60].	50
Figure 3.1. Fibre optic heat generating thermal anemometry flow sensor configuration	57
Figure 3.2. Reflection spectrum of the FBG inscribed in the 9.7 dB/cm high absorption fibre	57
Figure 3.3. Temperature rise of the high absorption fibre at different absorbed pump power	58
Figure 3.4. Optical setup of the high absorption fibre for flow measurement	59

Figure 3.5. Flow measurement setup .....	60
Figure 3.6. Response of the sensor at different flow speed .....	60
Figure 3.7(a). Emperical constant A and (b) constant B of the high absorption fibre at different absorbed power level.....	62
Figure 3.8. Sensitivity of the high absorption fibre versus flow speed.....	63
Figure 3.9. Graphical illustration of cross section of the high absorption fibre and the thermal resistance of the cladding and the fluid.....	64
Figure 3.10. Temperature distribution in radial direction of the high absorption fibre with air flow speed at 3 m/s .....	71
Figure 3.11. Temperature difference in the core and cladding at different absorbed power level.....	72
Figure 3.12. Thermal conductivity of fused silica .....	72
Figure 3.13. Percentage difference in thermal conductivity in the cladding. Black line shows the percentage difference between the average of the cladding and the outer surface of the cladding. The red line shows the difference between the cladding average and the core – cladding interface. ....	73
Figure 3.14. Sensitivity against core size at 1 m/s and 243 mW absorbed power....	76
Figure 3.15. Flow response of the single mode (SM) high absorption fibre (core diameter: 8.3 $\mu$ m) and the multimode (MM) high absorption fibre (core diameter: 50 $\mu$ m) and the corresponding simulation results. ....	76
Figure 3.16. Expermental and simulated sensitivity of the single mode high absorption fibre and the multimode high absorption fibre at different flow speed. .....	77

Figure 3.17. Simulated flow sensitivity of the high absorption fibre of different outer diameter at 6 m/s and 1 m/s. The absorbed power used for simulation is 243 mW.....	78
Figure 3.18. Transmission spectrum of the high absorption fibre at about 310 °C at different time.....	80
Figure 3.19. Reflection spectrum of the high absorption fibre at about 310 °C at different time.....	80
Figure 3.20. Decay of FBG inscribed in the high absorption fibre at different temperature and time.....	81
Figure 3.21. The normalized integrated coupling constant of the FBGs inscribed in the high absorption fibre against the demarcation energy .....	82
Figure 3.22. Experimental setup for measuring water flow.....	83
Figure 3.23. Sensor response at different absorbed power level.....	84
Figure 3.24. Constant A and B at different absorbed power level.....	85
Figure 3.25. Response of sensors at different ambient temperature. The absorbed power was 720 mW.....	85
Figure 3.26. Change in constant A and B at different ambient temperature.....	86
Figure 4.1. (a) Optical setup of the experiment. (b) Wind tunnel experimental setup. ....	94
Figure 4.2. Pulsation of sensor's wavelength when the optical switch is open for a time long enough to allow the high absorption to reach steady state.....	96
Figure 4.3. Pulsation of sensor's wavelength when the open time of the optical switch is short and cannot reach steady state.....	96

Figure 4.4. Experimental and simulated response of the falling edge time constant when the sensor's temperature is allowed to reach steady state (long pulse) and too short to reach steady state (short pulse) .....	97
Figure 4.5. Experimental and simulation results of the high absorption thermal anemometer in constant power operation .....	98
Figure 4.6. Experimental optical connection of the serially multiplexed sensor working in around 850 nm .....	99
Figure 4.7. Reflection spectrum of the sensor array .....	100
Figure 4.8. Experimental results of the multiplexed sensor in pulse operation .....	101
Figure 4.9. Experimental results of the multiplexed sensor in constant power operation.....	101
Figure 4.10. Fluctuation in time constant of the 837.9 nm (3 dB/cm high absorption fibre) sensor.....	102
Figure 4.11. Reflection spectrum of the FBGs after the experiment .....	103
Figure 5.1. Experimental setup of the pressure sensor system .....	109
Figure 5.2. Spectrum of the 38 cm long PM-PCF based Sagnac loop at different pressure value.....	110
Figure 5.3. Shift of spectral peak against pressure shift of the 38 cm long sensor.	111
Figure 5.4. Shift of spectral peak against pressure shift of the 68.8 cm long sensor .....	111
Figure 5.5. Spectral peaks wavelength shift against temperature shift of a 25 cm long PM-PCF sensor .....	113
Figure 5.6. Spectral peaks shift against temperature shift of a 21 cm long PM780-HP sensor .....	113

Figure 5.7. Spatial frequency spectrum of the 38 cm sensor at different pressure value. (Low frequencies components only) .....	115
Figure 5.8. Experimental and calculation results of the 38 cm long sensor's frequency shift.....	115
Figure 5.9. Group birefringence of the 38 cm and the 68.8 cm long sensor at different applied pressure .....	116
Figure 5.10. Phase shift of the 38 cm long sensor .....	117
Figure 5.11. Experimental and calculated phase (concatenated) of the sinusoidal waveform at different pressure.....	117
Figure 5.12. Standard deviation of the measured samples by spectral shift and phase shift method.....	119
Figure 5.13. Phase change of the 38 cm long sensor working at 1550 nm.....	119
Figure 5.14. Peaks shift of the 38 cm PM-PCF Sagnac loop pressure sensor working at 1550 nm.....	120
Figure 5.15. comparison of the measured pressure fluctuation of the sensor at 1550 nm by the two methods .....	121

# Chapter 1

## Introduction

### 1.1 Background

Optical fibre is certainly one of the most important inventions. The medium for telecommunication was once mostly based on copper cables. Nowadays, most of the copper cables have been already replaced by optical fibre. Optical fibre offers enormous bandwidth, low loss and is light weight. It is also highly flexible and insensitive to electromagnetic interference (EMI). These make it a great candidate to replace the old copper cable for much faster and reliable telecommunication. The use of optical fibre for telecommunication ranges from intercontinental to inside your home. Its importance is not just limited to telecommunication, one of its other popular applications is optical fibre sensor. Fibre optic sensors offer many advantages over traditional electronic sensor like the ability to withstand high temperature and the ability for remote sensing due to its low attenuation. Due to these advantages, it is now widely used in remote and harsh environment.

Fibre Bragg grating (FBG) based sensor is a commonly used type of optical fibre sensors. An FBG reflects certain wavelengths of the propagating broadband light in the backward direction. The reflected wavelengths change as the measurand changes. To read the sensor, an optical fibre interrogator is needed to measure the optical spectrum. FBG can be fabricated by exposing the fibre to UV light through a phase mask. The phase mask controls the period of the fabricated FBG. Using different phase masks one can fabricate FBGs of different wavelengths. As a result, FBGs with different wavelengths can be serially multiplexed together, easily forming a

network of sensors. As the FBG's reflected wavelength is mainly affected by the refractive index and grating period, strain and temperature affect the reflected wavelength. If the measurand is not strain or temperature, using a transducer to convert the measurand to temperature or strain also allows measurement.

Another type of sensor is based on interferometry. In such systems, a light beam is split into two and travels along different path. The two beams meet together and form an interference pattern. The measurand changes one of the beam paths and thus alternate the interference pattern. One way to read this kind of fibre optic sensor is to read the spectrum of the interference spectrum. A device that can read the optical spectrum is needed. A commonly used interferometer is Sagnac interferometer. A Sagnac interferometer is a loop, a coupler is used to split the incoming light into two and they travel in the opposite direction. The two propagating light then interfere with each other at the coupler again and the interference pattern can be read by an optical fibre interrogator for measuring the desired measurand.

## **1.2 Objectives**

The objectives of the study are to develop optical fibre sensor systems that can potentially be used for oil and gas industry. Two important sensing functions are investigated. These include pressure sensing and sensing of flow rate of gas and liquid. The developed fibre optic based systems offer benefits over the traditional electronic sensing systems. Traditional electronic sensor system is usually very sensitive to noise. The noise can come from EMI and thermal noise. In addition, for remote sensing, the sensors are usually placed far away from the measurement system, which is usually placed indoor. Long copper cables will result in high attenuation. Moreover, long cables will also pick up electromagnetic interference.

These will result in significant amount of noise for detected signal and will compromise sensitivity of the measurement system.

Fibre optic sensors are great candidates for operation in remote and harsh environments, which is typical for oil and gas industry. Optical fibre is immune to EMI and its attenuation can be as low as 0.15 dB/km, which makes it a perfect candidate for such operation environment. The work carried out in the thesis focuses on two types of sensors: flow sensor and pressure sensor. Flow sensor is critical in many different industries as it plays the key role in product quality and quantity control. One kind of flow sensors is hot-wire anemometer. For example, controlling the blend of different fluids and delivering enough coolant, all require flow control. A conventional hot-wire anemometer comprise of a heated resistive wire and control circuit. The resistance of the heated wire is dependent on the temperature. If constant current is applied to the wire, the voltage across the heated wire varies as the flow rate changes. Another common measuring method is to maintain the temperature of the heated wire constant. For measuring flow in pipes, long cables are required which means optical fibre sensors are the ideal candidate due to its low loss. Also, in the case of corrosive fluid flow, the silica structure of the fibre itself is resistant to many different corrosive substances. A pure silica and transducer free design can fully benefit from the characteristic of optical fibre sensor. However, flow sensor design that is pure silica and transducer free is not reported before. It is thus important to study design of such sensors for potential downhole applications. Pressure sensors are also used in downhole applications of oil and gas industry. These applications usually require sensors to be placed quite far or deep underground, and the working environments are usually harsh. This again makes optical fibre pressure sensor the ideal candidate. Despite the long development

history of optical fibre sensor, no effective optical fibre based solution has been proposed prior to this study, especially for flow measurement.

In the thesis, several optical fibre sensing based schemes were investigated and proposed. The major contributions are as follows:

1. Development of a novel pure fibre optic thermal anemometer. Unlike other reported optical fibre based thermal anemometers, this design is based purely on silica fibre without the addition of any other metal and is driven by optical power. This design comprise of a high absorption fibre that absorb optical energy. The absorbed optical power is converted into thermal energy. Convection caused by the flowing fluid alters the sensor's temperature. An FBG was inscribed in that high absorption fibre to instantly measure the sensor's temperature change.
2. A scheme of reducing the ambient temperature and pump power sensitivity of the pure fibre optic thermal anemometer is proposed and demonstrated. The flow speed measurement of the anemometer is realized by measuring the temperature of the high absorption fibre. However, the ambient temperature and optical pump power also affect the temperature. A modulated optical pump power and temperature time constant measurement is proposed and proved to be much less ambient temperature and pump power sensitive. The possibility of sensor multiplexing is also demonstrated with selected FBG's wavelength that suffer much less optical power attenuation, and the same measurement method showed similar response of the multiplexed sensors.
3. Improvements in sensitivity and reliability of previously reported Sagnac loop based temperature insensitive pressure sensor. It has been shown that by moving the operational wavelength to around 850 nm rather than the

operational wavelength of 1300 nm or 1550 nm as in all previously reported studies, the pressure sensitivity of the system is shown to be improved by about 3 times. This will also allow the use of a charge-coupled device (CCD) based optical fibre sensor interrogator that may significantly lower the system cost. A new detection scheme is also proposed and proved to be more consistent in pressure sensitivity than the previously reported methods that measure spectral shift.

### **1.3 Thesis outline**

This thesis is divided into 6 chapters. After introducing motivation, objectives and major contributions in chapter 1, chapter 2 reviews the developments of different flow and pressure sensors and the technique behind.

Chapter 3 introduces the novel pure fibre optic thermal anemometer. The construction and operation of this sensor is discussed. Moreover, equations using purely physical parameters of the sensor's material and the target fluid for simulating the response of sensor are developed. These equations help predict and explain the response of the flow sensor.

Chapter 4 proposes new methods that reduce the anemometer's power and ambient temperature dependency. As the measuring methods used in the previous chapter and also other conventional methods are dependent on the ambient temperature and the absorbed power, a new method is proposed to minimize these effects. Multiplexing of the sensors is also discussed.

Chapter 5 discusses a Sagnac loop based pressure sensor with techniques to enhance reliability and extend measuring range. Through simulation and experimental studies, it has been shown that changing the operating wavelength from 1550 nm to 850 nm

offers nearly 300% sensitivity improvement. Technique based on fast fourier transform (FFT) is proposed to improve the reliability and extend the measuring range.

Chapter 6 draws conclusions on the work and gives direction of future developments.

## **1.4 Contributed publications**

### **Conference**

[1] **L. H. Cho**, H. Y. Fu, C. Wu, C. Lu, and H. Y. Tam, “Low cost pressure sensor system based on polarization-maintaining photonic crystal fiber operating at 850 nm with CCD interrogator,” *Proc. SPIE*, vol. 7753, pp. 77533P-1–77533P-4, May 2011.

### **Journal**

[1] S. Gao, A. Zhang, H. W. Tam, **L. H. Cho**, C. Lu, “All-optical fiber anemometer based on laser heated fiber Bragg gratings,” *Opt. Express*, vol. 19, no. 11, pp. 10124-10130, May 23, 2011.

[2] **L. H. Cho**, C. Wu, C. Lu, H. Y. Tam, “A highly sensitivity and low-cost Sagnac loop based pressure sensors,” *IEEE Sens. J.*, vol. 13, no. 8, pp. 3073-3078, Aug. 2013.

[3] **L. H. Cho**, C. Lu, A. Zhang, H. Y. Tam, “Fiber Bragg grating anemometer with reduced pump power-dependency,” *IEEE Photon. Technol. Lett.*, vol. 25, no. 24, pp. 2450-2453, Dec 2013.

### **Patent Application**

[1] H. Y Tam, A. Zhang, S. Gao, **L. H. Cho**, “Sensor for measuring flow speed of a fluid,” U. S. Patent Application Publication US 2013/0014577 A1, Jan 17, 2013.

# Chapter 2

## Literature review

### 2.1 Fibre Bragg Grating

#### 2.1.1 Introduction

A fibre Bragg grating (FBG) is a periodic or aperiodic modulation of refraction index along the optical fibre core [1]. The grating functions as a filter which reflects selected wavelength of light in the backward direction while letting the others to pass through it. K. O. Hill and his co-workers [2] discovered internally written Bragg gratings accidentally in 1978 during an experiment of study on stimulated Raman (SRS) scattering. Highly germanium (Ge) doped core high-silica fibre was used in their experiment. They launched light with wavelength at 514.5 nm from their argon-ion laser into the fibre core and realised a decrease in the transmitted light. They discovered that light was reflected by a refractive index hologram inside the core, which was written by the sinusoidal standing wave pattern caused by interference of the forward and backward propagating laser light [3]. In 1989, Meltz et al. first reported holographic methods that inscribe gratings in optical fibre by exposing it to the interference pattern of two equal intensity laser beam which is split from a 244 nm laser output [4]. FBG fabricated by this method is not length limited and can be made to offer different transmission or reflection characteristics. Later, in 1993, fabrication of FBG by photolithography was reported [5]. K. O. Hill et al. reported the use of phase mask to imprint FBG onto photosensitive fibre core. A phase mask with suppressed zero order was used. The phase mask was placed in contact or very close to the optical fibre. The UV laser beam pass through the phase mask in normal

and was spatially phase modulated and diffracted beam formed an interference pattern literally that imprinted FBG. Nowadays, using phase mask is a common method to fabricate FBG.

### **2.1.2 Background**

Photosensitivity in the core of optical fibre was observed when laser light was launched into the core and formed gratings [2][3]. This was later shown to be associated with two-photon process [6]. The standing wave pattern was formed by the counter propagating waves in the germanium doped fibre and induced refractive index change in the GeO<sub>2</sub> doped core. Later, fabrication of FBG in germanium doped fibre by side illuminating 244 nm UV light was believed to be due to the germania oxygen vacancy defect which is centred at around 242 nm [4][7].

The photosensitivity of those slightly germanium doped fibres like the standard single mode fibre for telecommunication are usually low, the UV induced refractive changes could be of the order of  $10^{-5}$ . To improve the photosensitivity of those fibres, hydrogen loading technique was developed by P. J. Lemaire et al. [8]. Standard single mode fibre was exposed to hydrogen gas with the pressure ranging from 20 atm to over 750 atm. The peak UV induced refractive index change reached about  $5.9 \times 10^{-3}$ , which improves the photosensitivity over that achieved for fibre without hydrogen loading. The H<sub>2</sub> molecules react at Si-O-Ge sites in the fibre core and form Si-OH and Germania oxygen vacancy defect which means grating can be inscribed by UV light around 242 nm.

In 1994, J. Albert et al. demonstrated FBG that is inscribed using phase mask technique with 193 nm ArF excimer laser. The writing efficiency with 193 nm

excimer laser in hydrogen loaded optical fibre is higher than 248 nm laser [9]. Another mechanism involved in FBG fabrication is by damage mechanism. B. Malo et. al used a high power single 249 nm excimer laser pulse to photo imprint FBG into optical fibre. This single UV pulse fabricate grating with period the same as that of the phase mask [10]. Later, 193 nm excimer laser was found to form negative index gratings. The change in index modulation first goes up and reach the positive maximum and then decrease slowly toward the negative maximum. The stability of the negative index grating was tested to be more stable than positive index gratings fabricated by 193 nm or 248 nm excimer laser. [11]

Fiber Bragg grating (FBG) has long been used as different kind of sensors. A FBG is modulation of refractive index inside the core of the optical fibre. Coupling of FBG occurs between the forward and backward propagating guide modes in the FBG [1].

$$\beta_2 = \beta_1 + m \frac{2\pi}{\Lambda}, \quad (2.1)$$

where

$$\beta = \frac{2\pi}{\lambda} n_{eff}. \quad (2.2)$$

$\beta$  is propagation constant,  $\beta_1$  and  $\beta_2$  is the propagation constant of the forward and backward going light respectively.  $\Lambda$  is the grating period,  $m$  is the order of mode,  $\lambda$  is wavelength and  $n_{eff}$  is the effective refractive index. For first order diffraction,  $m = -1$ . As the coupling is between the forward and backward propagating, so  $\beta_2 = -\beta_1$ .

Then we have

$$\lambda_B = 2n_{eff} \Lambda, \quad (2.3)$$

where  $\lambda_B$  is the center wavelength of the back reflected light. Figure 2.1 shows the simplified structure of a simple FBG.

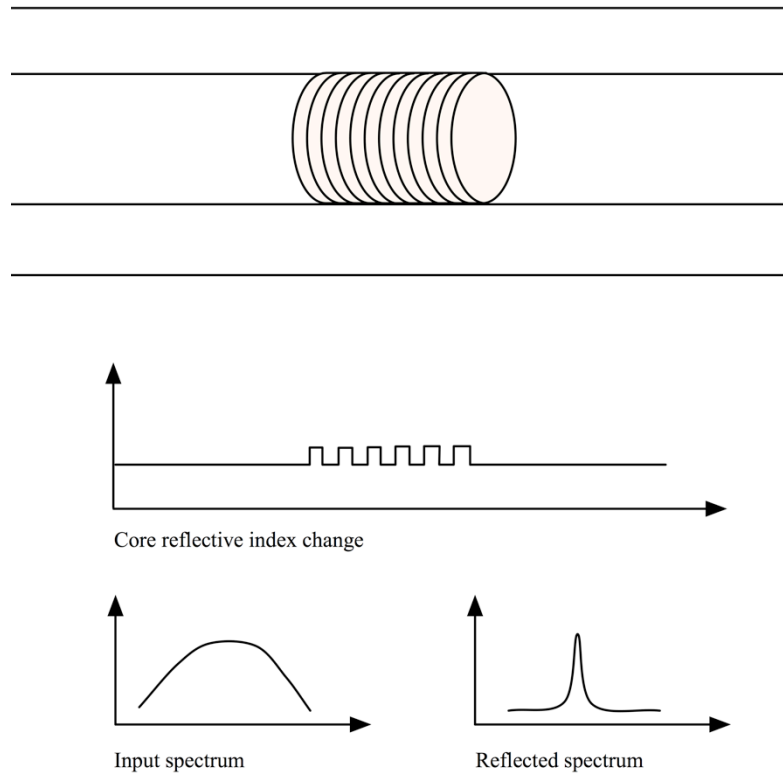


Figure 2.1. Fiber Bragg Grating

The Bragg resonance wavelength is related to the effective refractive index and the period of the grating. If any one of the factors or both of them change, the Bragg resonance wavelength also changes. Strain and temperature can affect these two factors. So it is possible to use FBG to measure strain, temperature or both of them. The change of Bragg resonance wavelength due to change in temperature and strain is given by [12] [13]

$$\Delta\lambda_B = 2 \left( \Lambda \frac{\partial n_{eff}}{\partial \epsilon} + n_{eff} \frac{\partial \Lambda}{\partial \epsilon} \right) \Delta\epsilon + 2 \left( \Lambda \frac{\partial n_{eff}}{\partial T} + n_{eff} \frac{\partial \Lambda}{\partial T} \right) \Delta T \quad (2.4)$$

The first term represents the change of wavelength due to change of strain and the second term represents the change of wavelength due to change of temperature. The effect of strain can be expressed as

$$\Delta\lambda_B = \lambda_B \left\{ 1 - \frac{n_{eff}^2}{2} [p_{12} - \nu(p_{11} - p_{12})] \right\} \epsilon \quad (2.5)$$

where  $p_{11}$  and  $p_{12}$  are components of strain-optic tensor and  $\nu$  is the Poisson's ratio.

The effect of temperature on the change of wavelength can be expressed as

$$\Delta\lambda_B = \lambda_B \left( \alpha + \frac{1}{n} \frac{dn}{dT} \right) \Delta T \quad (2.6)$$

where  $\alpha$  is the thermal expansion coefficient of the fiber and  $\frac{1}{n} \frac{dn}{dT}$  is the thermal-optic coefficient.

### 2.1.3 Thermal Decay

Fibre Bragg gratings are formed when the photosensitive optical fibres or the hydrogen loaded optical fibres are subjected to UV irradiation. These gratings are said to be permanent, but the properties of gratings change over long period or high temperature [11]. Detailed study on thermal decay was first done by T. Erdogan et al. in 1994 [14]. The electrons are excited by UV to the conduction band and then trapped in a continuous distribution of energy state. The rate of de-trapping the electrons depends on the temperature and the depth of the trapping state. Figure 2.2 shows the simplified model of the thermal decay mechanism. The trapped electron would be thermally released back to the original energy level before the UV excitation. The demarcation energy  $E_d$  separates the distribution state into 2 groups. For the groups with  $E < E_d$ , the energy level is close to thermal equilibrium with the conduction band. Over time these electrons will depopulate and looks like Figure

2.2b. For the group with  $E > E_d$ , it would be too deep to be thermally excited by only time.

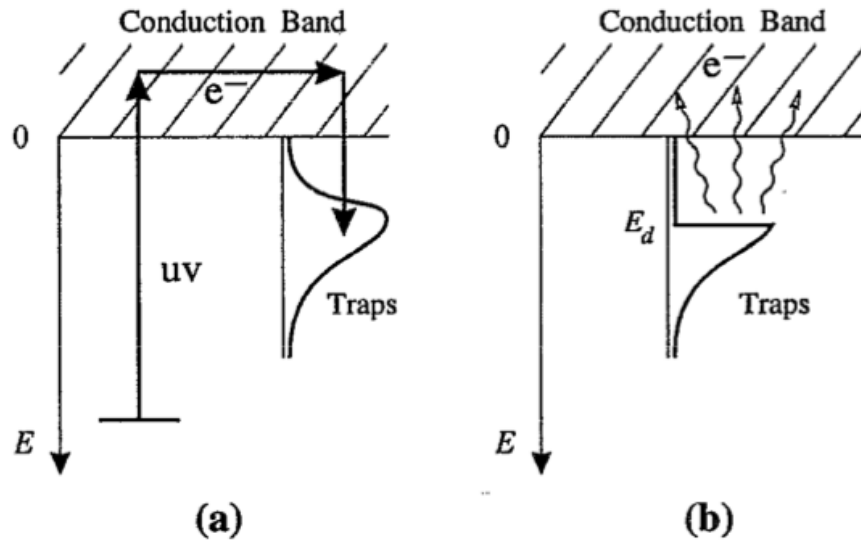


Figure 2.2. Physical model of a) electrons excited by UV are trapped in continuous distribution of traps; b) shallow traps ( $E < E_d$ ) is emptied and deeper traps remain full by thermal depopulation at a given temperature and time.

The decay of the FBG was shown to obey power law [14]. The reflectivity of the grating first decay tremendously then become much slower as time advance. It was also found to be strongly related to temperature. The integrated coupling constant (ICC) was used as a measure of gating strength due to its proportionality to the UV-induced refractive index change. ICC is given by

$$ICC = \tanh^{-1} \left( \sqrt{1 - T_{min}} \right). \quad (2.7)$$

$T_{min}$  is the transmission minimum. Figure 2.3 shows the relationship between the normalized integrated coupling constant  $\eta$  and time.  $\eta$  is normalized to ICC at  $t = 0$ . The figure shows a rapid decay at the beginning. After that, the rate of decay drops significantly.  $\eta$  can be fitted into

$$\eta = \frac{1}{1 + A(t/t_1)^\alpha}. \quad (2.8)$$

The dimensionless factor  $A$  and  $\alpha$  were found to be temperature dependent.  $t$  is time.

The constant  $t_1$  is the unit time and was set to 1 min to keep  $\eta$  constant in ref. [14].

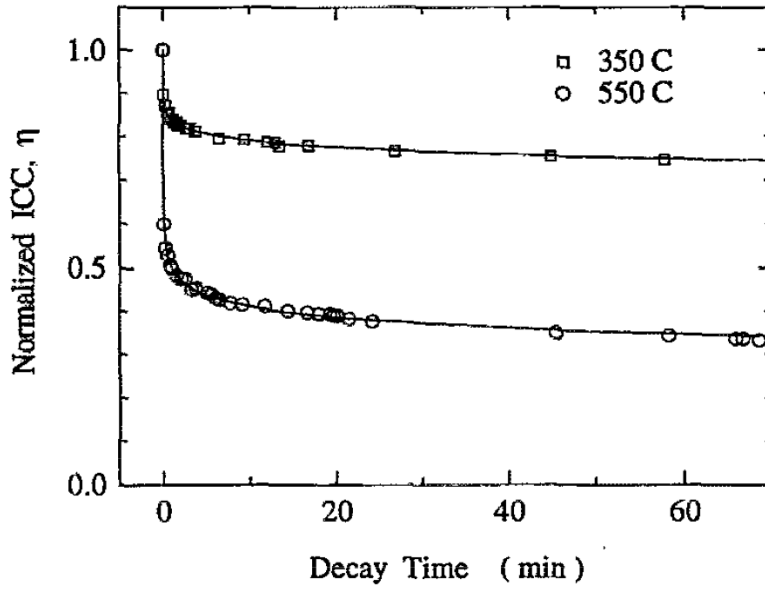


Figure 2.3. Measured normalized integrated coupling constant of 2 gratings heated to 350°C and 550°C. [14]

Figure 2.4a shows the variation of factor  $A$  against temperature and Figure 2.4b shows the relationship between factor  $\alpha$  and temperature.  $\alpha$  was fit to the equation

$$\alpha = T/T_0. \quad (2.9)$$

where  $T_0$  is a constant.  $A$  has the form

$$A = A_0 \exp(aT), \quad (2.10)$$

where  $A_0$  is a constant.

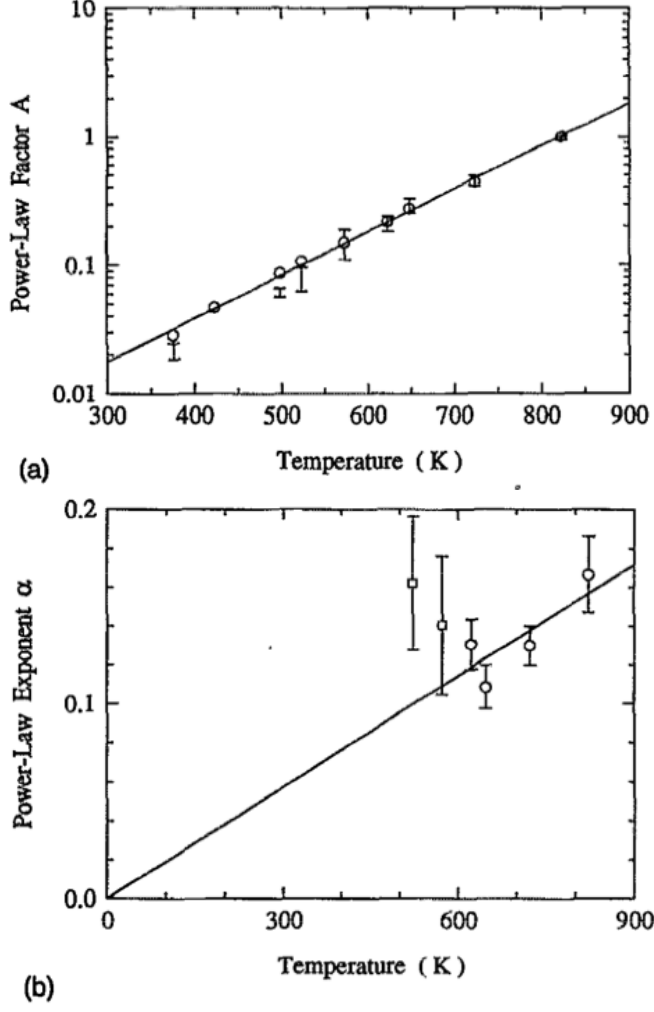


Figure 2.4. (a) Power law factor A obtains by curve fitting. (b) Power law factor  $\alpha$  obtained by curve fitting [14].

The normalized integrated coupling constant  $\eta$  is expressed in terms of  $E_d$  as [14]

$$\eta = \frac{1}{1 + \exp\left[\frac{(E_d - \Delta E)}{k_B T_0}\right]}, \quad (2.11)$$

where  $k_B$  is the Boltzmann constant and  $\Delta E = -k_B T_0 \ln(A_0)$ ,  $E_d = k_B T \ln(\nu_0 t)$ .  $\nu_0$  is a frequency term given by  $\nu_0 = \exp(aT_0)$ . Figure 2.5 shows the combined plot of different temperature's decay curve of the normalized ICC as a function of the demarcation energy  $E_d$ . By selecting the right value of  $\nu_0$ , all the results can be fitted with a single curve by equation (2.11). Figure 2.6 shows the decay of a grating first heated to 350 °C and then to 550 °C. At 350 °C and 70 min, the normalized ICC of

the grating drops to about 75%. The grating was then heated to 550 °C. The normalized ICC of the grating drops to about 33% of the original value, which is similar to Figure 2.3. This suggests that the history of the grating influence the decay process. This also proves that the trap is not a single state. So, most of the electrons above certain depth of trap are depopulated but not some of the electrons at a single state are depopulated. In the case of a single trap state, the decay will not be related to the previous decay history and the grating shown in figure 2.6 would drop to 33% of the 75% (i.e. 25%) instead of 33%.

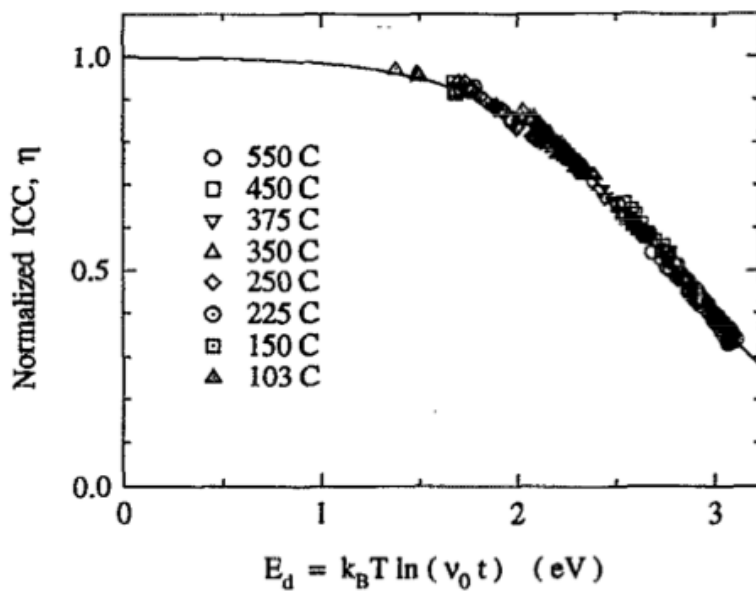


Figure 2.5. Normalized integrated coupling coefficient  $\eta$  as a function of the demarcation energy  $E_d$ . [14]

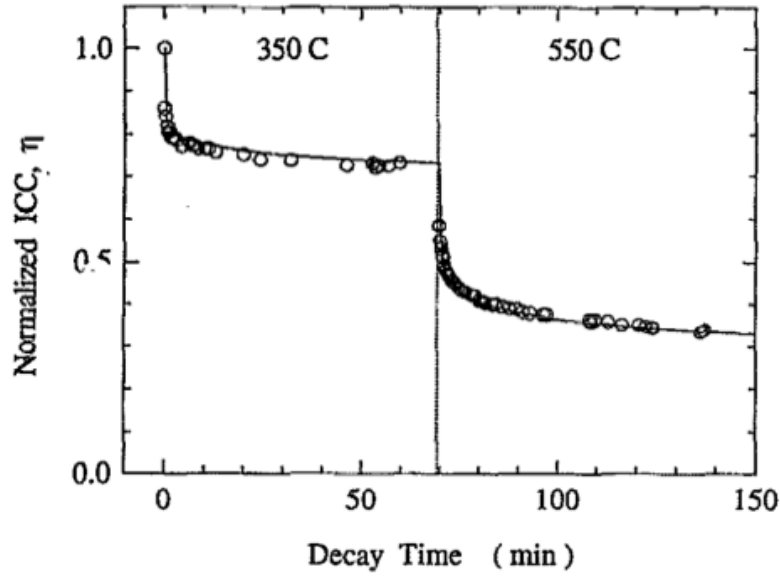


Figure 2.6. Decay of grating first at 350 °C then 550 °C [14]

As illustrated above, the dependency on the decay history of the gratings suggests that the decay process can be accelerated. Two approaches can be used, the power law approach and the aging curve approach [14][15]. According to [15], the aging curve method is more general. For the aging curve approach, different datasets of different temperatures are combined into a single curve as shown in Figure 2.5. The curve is fitted by equation (2.11). The parameter  $\nu_0$  is found by curve fitting of different results at different temperature [15]. For the power law approach,  $A \propto \exp(T)$  and  $\alpha \propto T$  [14][15]. According to Figure 2.7, the parameter  $\alpha$  is not in a clear linear relationship with temperature  $T$ . Figure 2.8 shows the comparison between the two approaches for accelerated aging. The power law approach shows to deviate more from the experimental results when compared to the aging curve approach, which suggest the aging curve is more general [15].

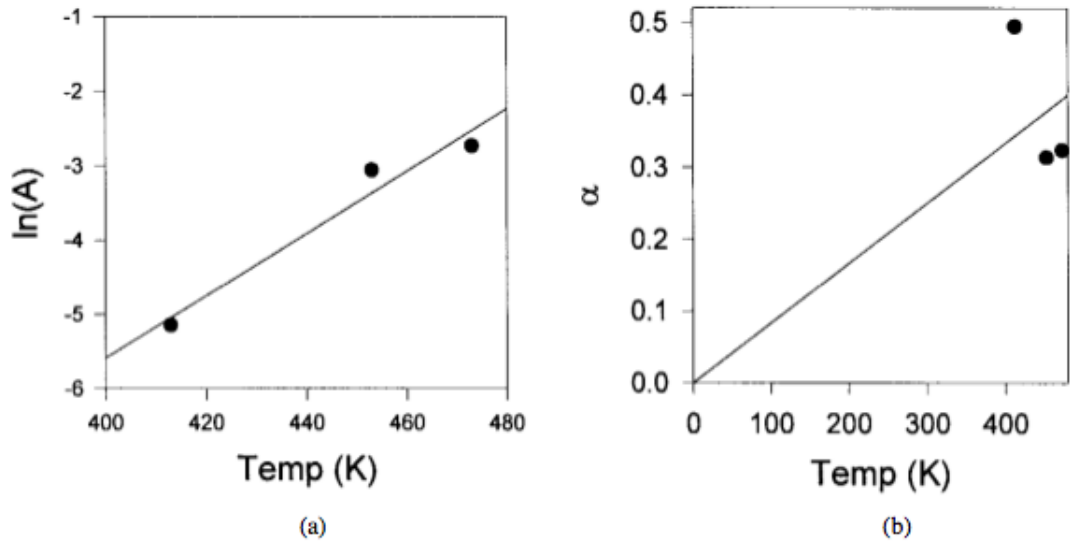


Figure 2.7. (a)  $A$  against  $T$  and (b)  $\alpha$  against of a weak grating [15].

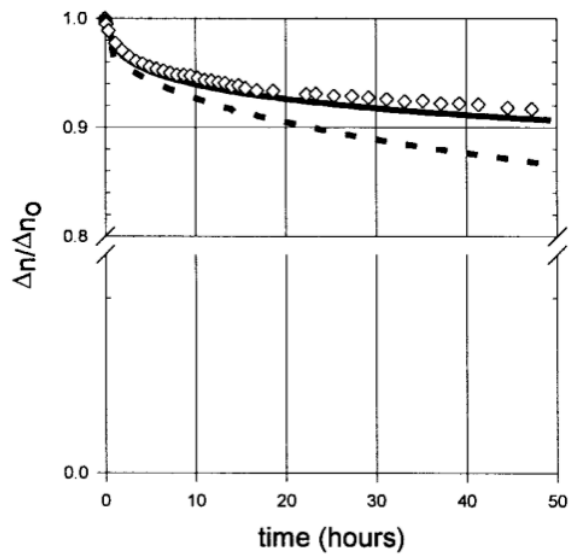


Figure 2.8. Comparison between aging curve approach and power law approach for accelerated aging. Continuous line: Aging curve approach. Dotted line: Power law approach. Square: Experimental results. [15]

## **2.2 Flow Measurement**

### **2.2.1 Introduction**

Flow measurement has a history of over a thousand years. Flow is a very important parameter to be monitored. The quantity of fluid supplied gives information on demand, which is important for production planning. Manufacturing of many different materials or solution involves the mixture of required portion of different fluids. Flow monitoring provides information on the amount of certain fluid mixed in the product. Flow monitoring is essential for flow control. Flow control is required to maintain certain operation conditions like the air fuel mixture in an internal combustion engine or the cooling of engines. Fluid flow measurement and control is thus crucial in every aspect of our life, from extraction and refinery of oil and gas in heavy industry to proper operation of automobiles.

To measure flow, a flowmeter is required. Flowmeters can broadly be classified based on the method used to measure the flow. They include inferential flowmeters, direct measurement flowmeters and energy additive flowmeters [16].

Inferential flowmeters measure flows by detecting the variation in physical parameters induced by the varying flow instead of directly measure the flow rate. There are many types of inferential flowmeters. The pitot tube is widely used in aviation industry to measure the air speed of an aircraft. Vortex flowmeter is another kind of inferential flowmeter. A bluff body is placed in the middle of the pipe which generate Kármán vortex street. Sensors are used for detecting the frequency of the vortex and converts it into flow rate.

Direct measurement flowmeters measure the flow rate directly. One kind of such flowmeters is turbine flowmeter. When the fluid flows through the turbine, the turbine rotates. Variation in rotation is related to flow rate.

Energy additive flowmeters input energy into the system and monitor the variation of the injected energy to calculate the flow rate. Ultrasonic flowmeter inject ultrasound wave into the fluid and measure the Doppler shift or the time the signal takes to reach the sensing component to determine the flow speed. Another very common type of energy additive flowmeters is hot-wire flowmeter/anemometer. Hot-wire flowmeter uses the principle of convective heat transfer to measure flow rate.

### **2.2.2 Non Fibre optics flowmeter**

Mechanical, electromechanical and electronic flowmeters have been used for many years and are well developed. Some of them are still quite commonly used. Below are descriptions of several kinds of non fibre optic based flowmeters.

#### ***A. Inferential flormeter – Drag body flowmeter***

The drag body flowmeter operates by the means of differential pressure caused by the obstructed flowing fluid. It is constructed with a mechanically constrained target placed into and facing the flow. The force generated by the pressure difference together with the force by viscosity try to push the target along the flow direction. Strain sensors or displacement sensors can be used to measure the flow rate [16]. Figure 2.9 shows the basic design of a drag body flowmeter. Such design is especially suitable for applications which the liquid contains suspended solid. One of the major disadvantages is the water pressure loss caused by the drag plate [17].

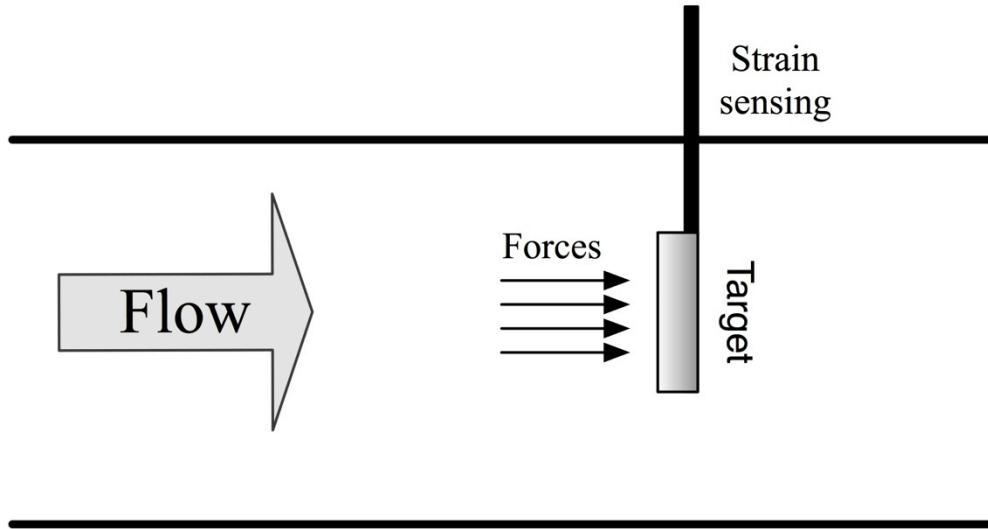


Figure 2.9. Graphical illustration of a drag body flowmeter

### ***B. Inferential flowmeter – Vortex shedding flowmeter***

Vortex shedding flowmeter measure flow rates by generating Kármán vortex street and measure the fluctuating frequency of the vortices [18] [19]. A vortex flowmeter needs a bluff body (vortex shedder), which is a shedder bar as illustrated in figure 2.10, with typical shape like T, rectangle, square or trapezoid [18]. When fluid flows through the bluff body, vortex street is formed downstream behind the bluff body. Such phenomenon is formed by the fluctuation of pressure and velocities on both sides of the vortex shedder. Figure 2.10 graphically illustrates a typical vortex flowmeter. The vortex frequency is given by

$$f = St \frac{v}{d}. \quad (2.12)$$

$St$  is Strouhal number,  $v$  is velocity and  $d$  is the width of the bluff body. The Strouhal number is a dimensionless parameter which shows the frequency and velocity relationship of the vortex shedder [19]. The Strouhal number is constant over a wide range of Reynolds number. The range is usually  $20,000 \leq Re \leq 70,000,000$  [18].

There are several methods to measure the vortex frequency. One way is to measure the pressure fluctuation. This can be measured by placing a movable tail behind the vortex shedder and measure the variation in strain of the tail. Pressure sensors placed on the pipe wall can be used to measure the pressure fluctuation. Another way to measure the pressure fluctuation is by ultrasound. Vortices interact with ultrasound and modulate the signal phase and amplitude [20]. The vortex flowmeter gives a linear response and works on both gas and liquid. But it cannot work in multiphase fluid and is unstable in low flow rate [19].

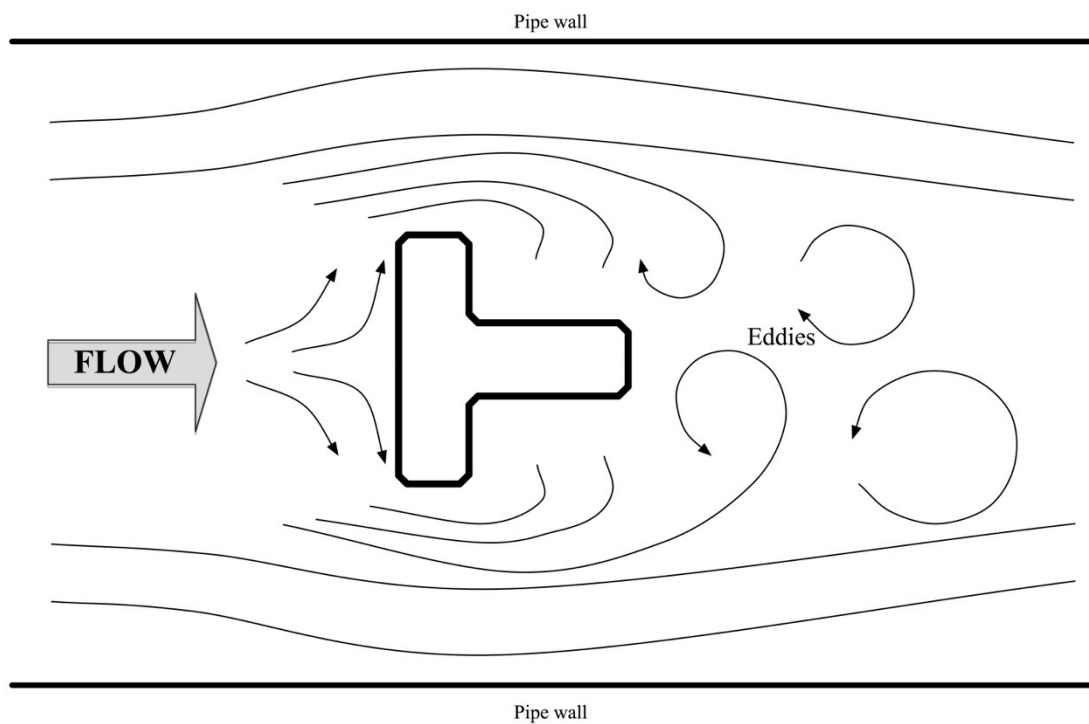


Figure 2.10. Graphical illustration of a vortex flowmeter

### ***C. Direction measurement flowmeter – Turbine flowmeter***

Turbine flowmeter is a kind of rotating flowmeter. It consists of a short section of pipe and a rotor blade with bearing support placed at the centre of the pipe. The rotor blade is sized very close to the inner dimension of the pipe. The blades are made to

be magnetic or with small magnet inserted. Pick-ups are placed outside to pick up signal when the blades pass through it. The output of the flowmeter is digital pulses with frequency linearly related to the flow rate over a wide range. Typical problem of turbine flowmeter arises from the bearing. Friction of bearing in large rotor gives insignificant errors [21]. It becomes significant when the rotor size is similar to the bearing. Another source of inaccuracy is the changes in fluid viscosity. Viscosity variation would disturb the rotor speed to flow speed relationship [16].

#### ***D. Energy additive flowmeter – Ultrasound flowmeter***

There are two common types of ultrasound flowmeter of which they use different topologies to measure the flow rate. One is ultrasonic time-of-flight flowmeter and the other one is ultrasonic Doppler flowmeter.

##### *Time-of-flight*

In ultrasonic time-of-flight flowmeter, the transit time between the downstream and upstream ultrasonic signal is used for the flow calculation. The time required for a sound signal to propagate downstream/upstream is dependent on the flow rate of the fluid and the speed of sound in that particular fluid.

$$t_u = \frac{D/\sin\theta}{c - V \cos\theta} \quad (2.13)$$

$$t_d = \frac{D/\sin\theta}{c + V \cos\theta} \quad (2.14)$$

Equations (2.13) and (2.14) show the transit time of the upstream and downstream ultrasound signals that refer to Figure 2.11 [19].  $t_d$  is the downstream transit time,  $t_u$  is the upstream transit time,  $D$  is the diameter of the inner wall of the pipe,  $L$  is the

distance between the two ultrasound transducer and  $\theta$  is the angle between the transducer and the wall. Figure 2.11 shows a simple ultrasound time-of-flight flowmeter with a single pair of transducers.

One way to make the system independent of sound speed in fluid is the sing-around system. The sing-around system uses the difference between downstream and upstream frequency, which are defined as  $f_d=1/t_d$  and  $f_u=1/t_u$  respectively, to eliminate the dependence on the speed of sound in the fluid  $c$  [19].

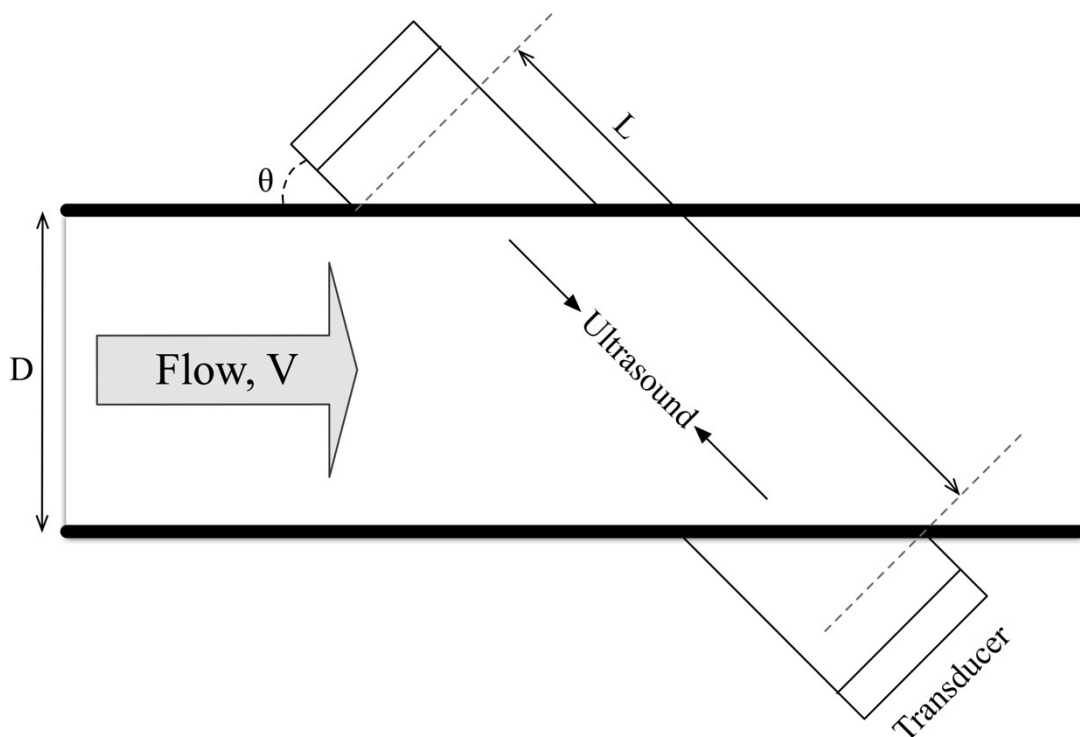


Figure 2.11. Ultrasound time-of-flight flowmeter

### Doppler

When a sound wave is reflected by a moving object, the frequency shifts according to the direction and velocity of that moving object. The ultrasound Doppler flowmeter makes use of this effect to measure the flow of fluid in the pipe. The ultrasound Doppler flowmeter requires the existence of disturbance like air bubble

and dirt particles to reflect the ultrasound wave [19][22]. The readings of the flowmeter depends on the speed of sound in the fluid. The readings can also be influenced by the number of existing disturbance. Those disturbances might also not be flowing at the same speed as the fluid, which cause another source of error [19][22].

#### ***E. Energy additive flowmeter – Hot-wire anemometer/flowmeter***

The hot-wire anemometer uses the principle of convective heat transfer to measure the flow rate of the targeted fluid. A short section of an electrical conductive wire is used as the heating element or even at the same time as the sensing element. The development of hot-wire anemometer can be dated back to the beginning of the 19<sup>th</sup> century [23]. Researches were first focused on the convection heat transfer of small copper wire in still and then moving air [24]. Most of the early development of hot-wire anemometer were constant-current hot-wire anemometer [23][25]. Later, researches were carried out on maintaining the temperature of the thin wire constant [26], which lead to the constant-temperature operation. Early hot-wire anemometers were mainly controlled manually without the aid of electronics and feedback. In late 20's, electronics were first incorporated into hot-wire anemometry [23] and feedback system was introduced in late 40's [26]. Weske [27] formed the system with the hot-wire in one arm of a Wheatstone bridge. The bridge operates in equilibrium stage. Disturbances like change in flow rate drive the system out of equilibrium. The potential difference caused by the disturbance is amplified and causes the system to vary the driving current of the hot-wire and maintain a constant temperature of the hot-wire. Constant temperature operation has a quicker response than constant current operation. The constant temperature hot-wire anemometer is now the dominant type of hot-wire anemometer and it gives higher frequency response than

the constant current type [28]. The frequency response of constant temperature hot-wire anemometer can reach over 100 KHz [25]. The signal to noise ratio of both types are found to be similar. Noise like radio, stray magnetic field affects the system. Also, the resistance of the hot-wire, resistors in the bridge, amplifier, etc, also play a significant part in the noise levels [25]. Figure 2.12 shows the construction of a basic hot-wire anemometer in constant current mode (without the dotted line feedback path) and constant temperature mode (with the dotted line feedback path).

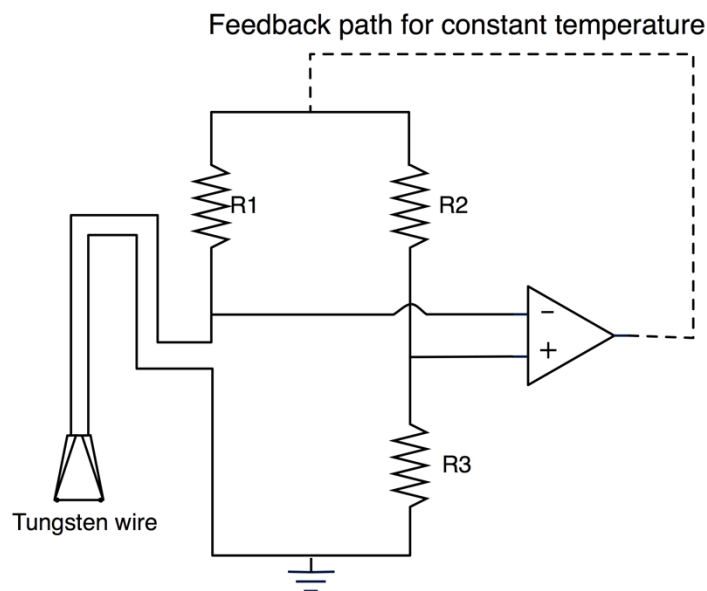


Figure 2.12. Basic hot-wire anemometer [25]

The equation of a finite length hot-wire probe can be given by

$$\frac{I^2 R_w}{R_w - R_a} = A + Bv^n \quad (2.15)$$

where  $I$  is the electric current,  $R_w$  and  $R_a$  is the resistance of the hot-wire element at the elevated and ambient temperature respectively,  $v$  is the velocity of the flowing fluid.  $A$ ,  $B$  and  $n$  are empirical constant to be determined by calibration procedures [29]. The resistance of the hot-wire is related to the mean wire temperature  $T_w$  by

$$T_w - T_a = \frac{R_w - R_a}{\alpha_0 R_0} \quad (2.16)$$

where  $\alpha_0$  is the temperature coefficient at 0°C and  $R_0$  is the hot-wire's resistance at 0°C and  $T_a$  is the ambient temperature. Combining equation (2.15) and (2.16),

$$\frac{E_w^2}{R_w} = (A + Bv^n)(T_w - T_a) \quad (2.17)$$

$E_w^2$  is the potential of the hot-wire at the elevated temperature. The term  $\alpha_0 R_0$  is absorbed into the parameters  $A$  and  $B$ .

For constant current mode, the velocity and temperature sensitivity are [29]

$$S_{v,cc} = \frac{nB\bar{v}^{n-1}I^3\bar{R}_w^2}{\bar{R}_a(A + B\bar{v}^n)^2} \quad (2.18)$$

$$S_{\theta,cc} = \frac{\alpha I \bar{R}_w R_0}{\bar{R}_a} \quad (2.19)$$

$S_{v,cc}$  is the constant current mode velocity sensitivity,  $S_{\theta,cc}$  is the constant current mode temperature sensitivity,  $\theta$  is the fluctuation of fluid temperature  $T_a$ ,  $\bar{v}$  and  $\bar{R}$  are their time mean value.

For constant temperature mode, the velocity and temperature sensitivity are [29]

$$S_{v,ct} = \frac{nBv^{n-1}}{2} \left[ \frac{R_w(T_w - T_a)}{A + Bv^n} \right]^{0.5} \quad (2.20)$$

$$S_{\theta,ct} = -\frac{1}{2} \left[ \frac{R_w(A + Bv^n)}{T_w - T_a} \right]^{0.5} \quad (2.21)$$

$S_{v,ct}$  and  $S_{\theta,ct}$  are the velocity and temperature sensitivity in constant temperature mode respectively. According to equation (2.20) and (2.21), the velocity sensitivity increases with increasing temperature difference  $T_w-T_a$  while the temperature sensitivity decreases with increasing temperature difference. This means higher overheat ratio  $R_w/R_a$  gives higher flow sensitivity while suppressing the effect of temperature fluctuation of the fluid.

### 2.2.3 Fibre optic flowmeter

The history of optical fibre based flowmeter is not long. The move from non fibre optic to fibre optic sensor is mainly due to the ability of withstanding harsh environment and compactness of the optical fibre sensor. Below are the reviews of several kinds of fibre optic flowmeter.

#### *A. Laser Doppler anemometer*

The laser Doppler anemometer (LDA) was first illustrated by E. Yeh et al. [30] in 1964. It measures flow by measuring the laser radiation scattered by tiny particles in the flowing fluid. Figure 2.13 shows the optical setup of a LDA used by R. J. Adrian et al.. The single laser beam is split into two. The two beams are reflected and focused in the fluid. The frequency of the light scattered by the moving particles toward the photomultiplier is [31]

$$f = \frac{2v \sin \theta}{\lambda} . \quad (2.22)$$

Later in the 80's, laser Doppler anemometry was reported based in optical fibre. Those LDA were first based on conventional single mode fibre. Later, LDA based on polarization maintaining fibre (PMF) was proposed [32]. The benefits of using

PMF includes the maintained polarization states. For single mode fibre, the polarization states of the light cannot be maintained. This affects the efficiency of the LDA [32]. Figure 2.14 shows the configuration of the PMF based LDA.

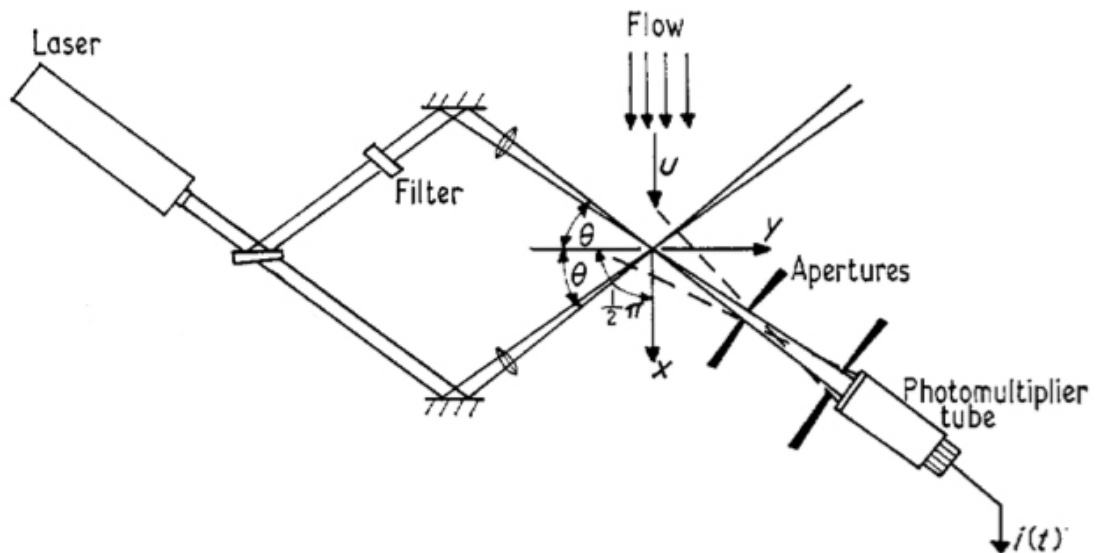


Figure 2.13. Typical optical configuration of laser Doppler anemometer [31]

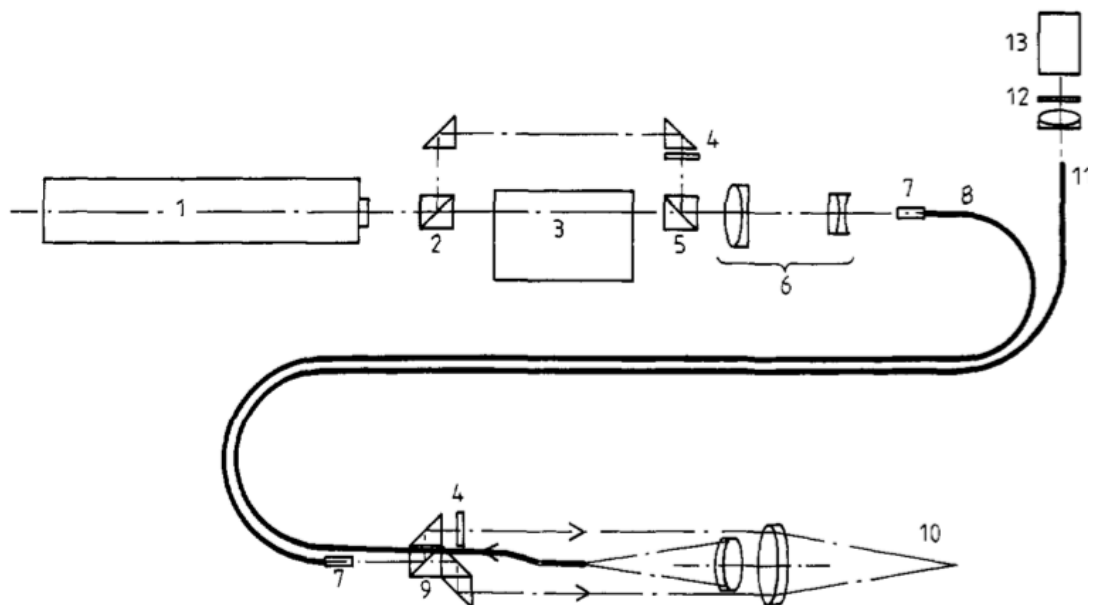


Figure 2.14. Optical setup of PM-PCF based LDA. (1) laser with polarized output; (2) 50/50 beam splitter; (3) Bragg cell; (4) 90° polarisation rotator; (5) polarization beam splitter; (6) beam compressor; (7) micro lens; (8) single mode polarization maintaining fibre; (9) polarization beam splitter; (10) measuring volume; (11) receiving multimode fibre; (12) filter; (13) photomultiplier. [32]

### ***B. Drag body flowmeter***

Several fibre optic flowmeter designs with principle similar to drag body flowmeter were reported [33] [34]. Those designs were based on using a cantilever beam which penetrate into the flowing fluid. The beam is bent by the force of the flowing fluid. Strain sensors were placed on the cantilever beam to measure the strain and direction of bending of the cantilever. W. Peng et al. [33] designed a flowmeter for downhole application. They used interferometer to measure the strain and direction of the cantilever beam. Two interferometers were placed on both side of the cantilever beam. Temperature fluctuation was compensated by calculation. The change in bending of the cantilever changes the length of the air gap of the interferometer, which indicates the flow rate. P. Lu et al. [34] used FBG to measure strain on the cantilever beam. A second FBG was placed in the fluid to measure the temperature.

### ***C. Vortex shedding flowmeter***

In vortex shedding flowmeter, a bluff body generates Kármán vortex street, which is a series of vortices. The optical fibre itself can act as the bluff body [35][36]. A multimode optical fibre ran from the top of the water pipe to the bottom. The optical fibre was slightly stretched to allow vibration. The vibration of the optical fibre was recorded by measuring the modulation of light intensity change caused by the microbending [36] or by measuring the change in interference pattern caused by variation in different mode in the optical fibre [35]. Both of the above mentioned design were not based on readily available standard single mode fibre. There were also publication on using single mode fibres. The fluid tested was air. The results showed linear response at high flow rate but deviate from the curve at lower rate. In ref. [37], the response deviates from the linear curve when the Reynolds number goes below around 50. Linear range is between 2.5 m/s and 8 m/s.

L. K. Cheng et. al [38] reported a FBG based vortex shedding flowmeter for downhole measurement. It consisted of a bluff body with an FBG sensor placed in a follower plate to measure the fluctuation of mechanical strain caused by the vortices. The FBG was inscribed in a standard single mode fibre. The vortex shedder was a T-shaped design with triangular body and a thin tail plate that the sensor was located. The vortices generate alternate high and low pressure that bends the plate and the FBG picks up the varying strain value. Their results shows a linear response from 1.1 m/s to 25m/s.

#### ***D. Hot-wire anemometer***

The usage of traditional hot-wire anemometer is quite popular, but not many papers on fibre optics hot-wire anemometer were published. One of the reasons why optical fibre hot-wire anemometer is not widely studied is due to the difficulty in heating up the optical fibre without any extra components on the sensor head. However, it is believed fibre optic hot-wire would be a good choice for measuring flow in harsh environments with its compact size (without the need of bulky vortex shedder as in vortex shedding flowmeter) and thus less head lost in the pipe.

Fibre optics thermal anemometry was reported in the 80's [39]. The heating element was not directly on the optical fibre itself. Later, Bobb [40] reported the use of gold coating directly coated on a section of uncoated silica fibre. Electric wires were connected to the gold coating and pass electric current through it to heat it up. These methods required the use of electric wire to guide electric current to the heating elements placed near the optical fibre or coatings on the fibre. Such system cannot fully utilise the benefits of optical fibre sensors, especially when working in harsh environment.

Later, Lamb, et. al [41] published their work on a purely optical technique to measure electric wind. They used carbon dioxide (CO<sub>2</sub>) laser to heat up the optical fibre. Figure 2.15 shows the setup of their experiment. The CO<sub>2</sub> laser beam externally hit one arm of the Mach-Zehnder interferometer. The reference arm was insulated while the measuring arm was exposed to laser radiation. The heat up caused by the laser changed the optical path length of the measuring arm relative to the reference arm. The output fringe shifted with respect to the flow.

Although the demonstrated optical fibre sensor is purely based on optical fibre, it is impractical to use such large CO<sub>2</sub> laser setup in many applications, especially for flow in pipe.

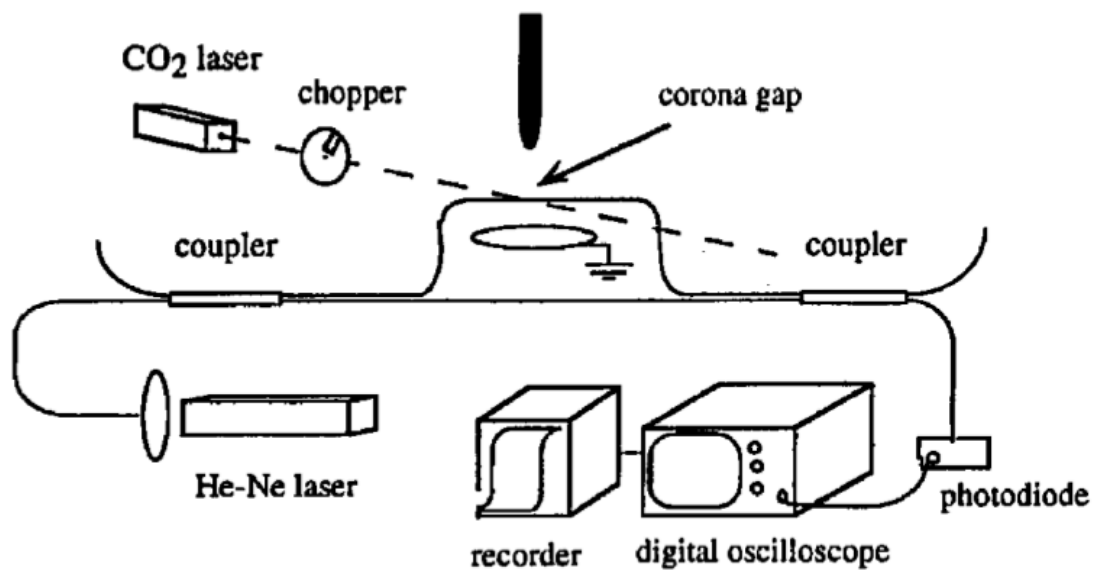


Figure 2.15. Electric wind measurement with CO<sub>2</sub> laser heating the fibre optic Mach-Zehnder interferometer [41]

In 2005, Chen et. al [42] reported a purely optical way to thermally tune FBGs. An FBG was written on a section of single mode fibre. The single mode fibre was then fusion spliced to a section of multimode fibre where the high power laser at 910 nm

was carried. Silver film was then coated onto the fibre section where the FBG was located. The silver film absorbs the 910 nm laser light and convert it to heat. The changes in temperature cause the wavelength shift of the FBG. Figure 2.16 shows the setup of their experiment. The sensors were designed to measure liquid level. The sensor's temperature in liquid is higher than that in air due to the much higher thermal conductivity of liquid.

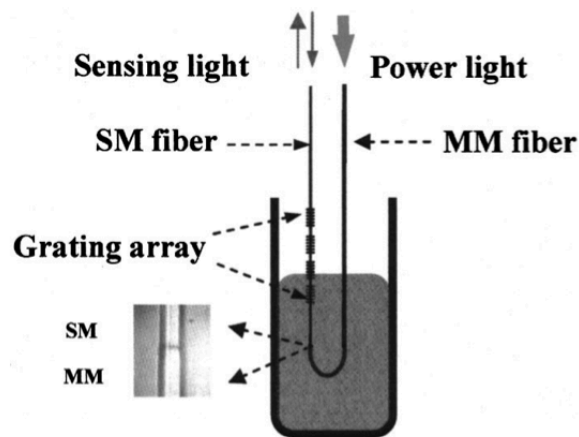


Figure 2.16. Experimental setup of silver coated self-heating FBG sensors for liquid level and temperature measurement [42]

The self-heating FBG sensor was later used as a flow sensor [43]. The same sensor design was employed. Two sensors were used to form a X-probe with 90° cross angle. The 2 sensors were positioned at the centre of the “X” which form the sensor probe. The use of X-probe allow the measurement of both flow rate and direction at the same time.

Similar concept of a fibre optic flow sensor was reported in 2011. Caldas et. al [44] reported the use of FBG written in single mode fibre with coated silver film. Instead of using multimode fibre, the whole experimental setup was solely single mode fibre. 400 mW of laser at 1480 nm was launched into the fibre. Long period grating (LPG)

was used to couple light from core mode to cladding mode which than hit the silver film. The use of LPG instead of fusion splicing single mode and multimode gives lower power loss and also gives better strength.

All the optical fibre based hot-wire anemometers reported require extra coating to generate heat. These coatings were made of metals. The problems with most metals are corrosion when the sensor is used in corrosive fluid, oxidation after prolonged operation and high temperature, directly exposed to the fluid, etc. These weaken the potential for fibre optic hot-wire anemometer in harsh environments.

Optical fibre doped with rare earth or transition elements experience optical absorption [45] [46]. The electronic relaxation of the dopant can be radiative or nonradiative. For cobalt doped optical fibre, about 34% of optical energy turns into thermal energy [46]. The experiment was conducted with a Ti:sapphire laser operating in the range of 700-720 nm. These results suggest that doped fibre can be used as a hot-wire anemometer without the need of electricity or any coatings. Such characteristic would be able to expand the usage of optical fibre hot-wire anemometer in harsh environments and lead to the investigation on the use of such fibre as hot-wire anemometer.

### **2.3 Sagnac Interferometer**

Sagnac interferometer was introduced by Sagnac in 1913 [47]. A light beam hit a beam splitter and split into two beams. One beam travels in the clockwise direction in the loop while the other one travels in the counterclockwise direction. The two beams meet again at the beam splitter and interfere. When the loop rotates, the beam travelling with the rotation direction lagging away from the beam splitter while the

beam travelling in the opposite direction advance towards the beam splitter. This cause the propagation time of the two beams to deviate and the optical path of the two beams are slightly different. The basic setup of a Sagnac interferometer is shown in Figure 2.17.

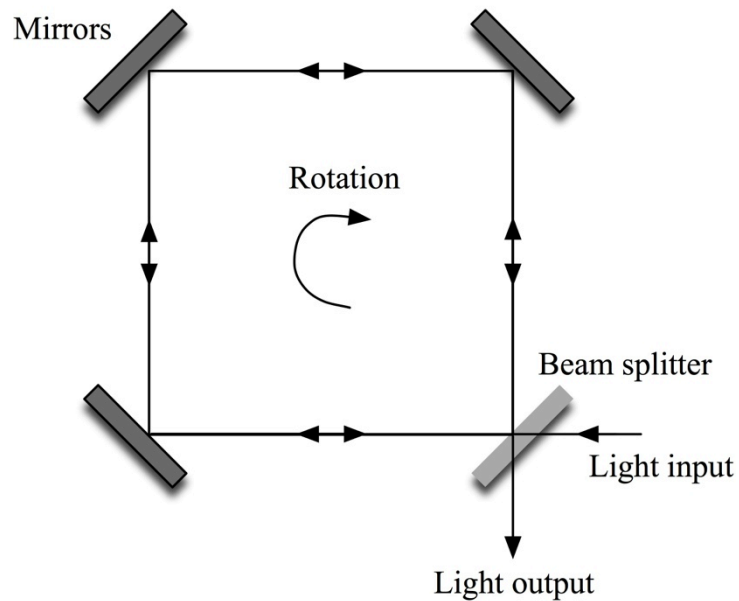


Figure 2.17. Basic sagnac interferometer in free space.

For a Sagnac interferometer, the observed spectral fringe shift in free space is

$$\Delta Z = \frac{4\omega NA}{\lambda c} \quad (2.23)$$

where  $\omega$  is the angular frequency of rotation,  $N$  is the number of round trips that the beams travel in the loop of area  $A$ ,  $\lambda$  is the wavelength in free space and  $c$  is the speed of light in free space. The size of the gyroscope would be very large if the area  $A$  is large or  $N$  is made over 100 [48].

Fibre optic sagnac interferometer was introduced in 1976 by Vali et. al [47][48]. Instead of free space mirrors to form the loop, optical fibre was used. The benefit of

using optical fibre is the size of the gyroscope is small even with large  $N$ . The enclosed area is circular and the spectral fringe shift equation is [48]

$$\Delta Z = \frac{4\omega N\pi R^2}{\lambda c} = \frac{2\omega LR}{\lambda c} \quad (2.24)$$

where  $L$  is the length of the optical fibre and  $R$  is the radius. In the experiment by Vali et. al [48], a beam splitter split a laser beam into two and then focused on the fibre ends. Later developments based solely on fibre optic components. Optical fibre couplers were used to replace free space beam splitter.

Other than gyroscopes, the Sagnac interferometer can also be used as different kinds of sensor. One application is current sensor. Phase difference between the counter propagating beams varies by the current in the cable wrapped around by the polarization maintaining fibre loop [49]. Another application is a hydrophone. If dynamic perturbations happen near the end of the loop, the propagation time difference between the counter propagating beams varies. This phenomenon can be used to measure perturbation like ultrasound [47].

In 2005, Liu et. al [50] published their work on using high birefringence fibre loop mirrors.  $n$  sections of high birefringence fibre sagnac loop were investigated. The coupler used was a fused taper coupler made of single mode fibre.  $n$  sections of high birefringence fibre and  $n+1$  sections of single mode fibre were connected alternatively. For a single section high birefringence fibre loop, the reflectivity and transitivity are given by [50]

$$R = \frac{I_{out}}{I_{in}} = 1 - \left[ \sin(\theta) - \cos\left(\frac{\beta}{2}\right) \right]^2 \quad (2.25)$$

$$T = \frac{I_{2out}}{I_{in}} = \left[ \sin(\theta) \cos\left(\frac{\beta}{2}\right) \right]^2. \quad (2.26)$$

Where  $\beta = -2\pi B l / \lambda$ ,  $\theta = \theta_1 - \theta_2$  and  $B$  is the birefringence.  $\theta_1$  is the rotation angle of the light enters the high birefringence fibre after passing through the single mode fibre.  $\theta_2$  is the rotation angle when it re-enters the coupler after passing through the high birefringence fibre.  $I_{1out}$  and  $I_{2out}$  is the output intensity at port 1 and 2 respectively and  $B$  is birefringence.

## 2.4 Fibre Optic Pressure Sensor

Optical fibre based pressure sensor has been developed over decades. An example of the early works is the work of Hocker et. al [51] published in 1979. In his work, the sensor was designed based on a Mach-Zehnder interferometer. Single mode fibre is used to form the two arms of the Mach-Zehnder interferometer. Pressure is applied on a portion of one of the arms. The pressure applied on the optical fibre changes the refractive index and diameter of the fibre. This induces phase change by the applied pressure. However, not only pressure induces phase variation, temperature can also induces phase variation. As a result, the uncertainty of the experiment was large.

Temperature dependency of the sensor is one key issue that affects pressure sensors. Zhao et. al [52] used FBG as pressure sensor. The transducer caused an isosceles triangle to bend. This is measured by a pair of FBGs to read the pressure induced strain as well as temperature. FBGs are placed on top and also at the bottom of the isosceles triangle. Temperature variation causes the two FBGs' wavelength shift in the same direction while strain variation causes their wavelength to shift in opposite direction. So temperature fluctuation can be compensated.

A Fabry-Pérot cavity based pressure sensor was reported by Zhu et. al [53]. The sensor was composed of single mode fibre, 62.5/125  $\mu\text{m}$  germanium doped core multimode fibre and 105/125  $\mu\text{m}$  pure silica core fluorine doped cladding multimode fibre. A 10-15  $\mu\text{m}$  short section of the 105/125  $\mu\text{m}$  multimode fibre was spliced to the end of the single mode fibre. 20-30  $\mu\text{m}$  section of the 62.5/125  $\mu\text{m}$  multimode was spliced to the end of the 105/125  $\mu\text{m}$  multimode fibre. The core of the 62.5/125  $\mu\text{m}$  multimode fibre was etched by hydrofluoric acid to form a cavity. A thin layer of the 105/125  $\mu\text{m}$  multimode was spliced to the end. This formed the diaphragm that is used for pressure sensing. Change in ambient pressure deflects the diaphragm and thus reduce the cavity length. The spectrum was read and the position of the fringe's maxima and minima is used to find the pressure value. The pressure was tested up to 190 psi (1.31 MPa), the cavity length change was 52.6 nm. The cavity length change due to temperature was 7 nm for 500°C of temperature change. 50°C temperature change gives 1.3% of length change of the 190 psi pressure change. The temperature sensitivity is about  $1.4 \times 10^{-5}$   $\mu\text{m}/^\circ\text{C}$  and the pressure sensitivity is about  $2.7 \times 10^{-4}$   $\mu\text{m}/\text{psi}$  ( $39.1 \times 10^{-3}$   $\mu\text{m}/\text{MPa}$ ).

Aref et. al [54] also reported the use of Fabry-Pérot cavity to sense pressure change. They used a metal tube to hold the single mode fibre at one side and a metal micro wire at the other side. An air gap was formed between the fibre and the metal micro fibre in the metal tube. The thermal expansion of the metal tube was compensated by the metal micro wire.

Another Fabry-Pérot cavity based sensor was demonstrated by Ran et. al [55]. 157nm was used to produce a circular hole on a fibre tip. The fibre with the hole was than spliced to another fibre to enclose the hole. The fibre was than cleaved close to the cavity to form a membrane that was used for pressure sensing. The sensor's

pressure sensitivity (measured by phase change) was 0.01 rad/MPa. The temperature sensitivity was 0.00005 rad/K, which means 1 K of temperature change is equivalent to 0.005 MPa.

The pressure sensors reported above were mainly based on single mode fibre. Polarization maintaining (PM) or high birefringence fibre based pressure sensors have also been proposed and demonstrated. Birefringence is given by

$$B = \frac{\lambda}{2\pi} (\beta_x - \beta_y), \quad (2.27)$$

where  $\beta_x$  and  $\beta_y$  are the propagation constant in the x and y axis respectively. Bock et. al [56] have studied experimentally the relationship between hydrostatic pressure and the birefringence in high birefringence fibre. The fibre used was York HB 800. The light source was a helium-neon laser operating at 632.8 nm. The laser beam is linearly polarized and coupled to the fibre at 45° to the principle axes of the high birefringence fibre. The output light was controlled by appropriate polarization elements before being monitored. The output signal strength against pressure was a sinusoid with the period depends on the fibre length. Experimental results showed the beat length increase (i.e. decrease in birefringence) as the pressure increase. This experiment showed high birefringence fibre itself can be used as pressure sensor without the help of any transducer.

Chiang et. al [57] stated that the elasticity of the stress applying part in the high birefringence fibre was not the same as the silica in the fibre. Due to the differences in Poisson's ratio, the stress applying part and the silica were experiencing different strain along the lateral direction. In their experiment, York HB800 high

birefringence fibre was used. The results also showed that the beat length increased (birefringence decreased) with the increase of pressure.

Those studies demonstrated that PM fibre could be a great candidate for pressure sensor. But at the same time, PM fibre could also be a good candidate for temperature measurement. Starodumov et. al [58] proposed the use of PM fibre based sagnac interferometer as temperature sensor. For internal stress fibre, the incorporated rods or elliptical cladding have different thermal expansion to silica. Thus, the birefringence of the fibre changes when temperature changes. This shows PM fibre can also be sensitive to temperature.

Szpulak et. al [59] published a paper on the pressure induced birefringence change in polarization maintaining photonic crystal fibre (PM-PCF). The pressure applied on the holey fibre induced stress across the fibre's cross section and also deformation in fibre structure. Two types of holey fibres were tested. Their structures are illustrated in figure 2.18. The structure B PM-PCF was manufactured by Blaze Photonics Inc. Figure 2.19 gives the wavelength dependency of phase and group modal birefringence of the 2 different structures of PM-PCF. Figure 2.20 gives the pressure sensitivity of phase and group modal birefringence of the 2 types of fibre. Group birefringence is related to phase modal birefringence by

$$G = B - \lambda \frac{dB}{d\lambda}. \quad (2.28)$$

The same group of people published another paper on the experimental results on the phase and group modal birefringence of the structure B fibre [60]. The results are shown in figure 2.21 and 2.22. These results demonstrated the potential of using the PM-PCF for pressure sensing.

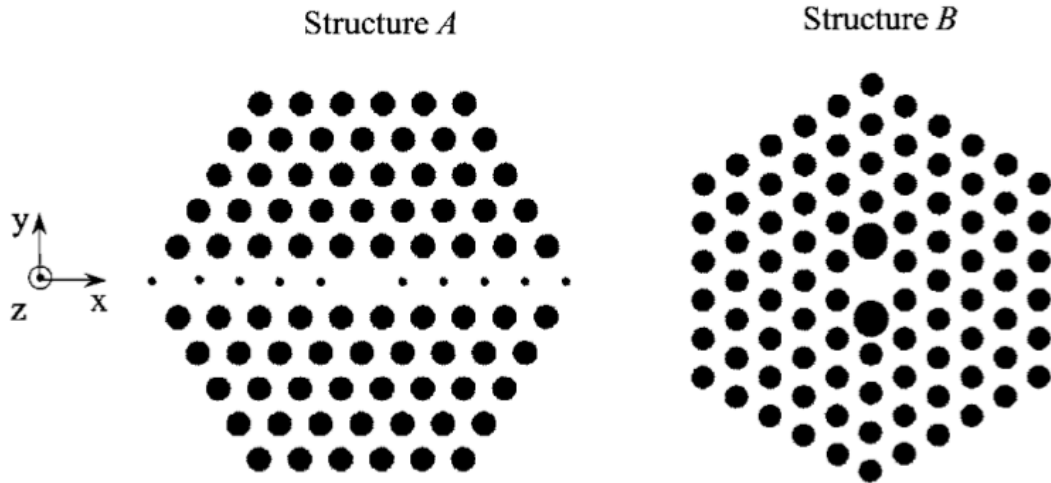


Figure 2.18. Cross section of the PM-PCF analyzed in [58]. Structure B was produced by Blaze Photonics Inc [59].

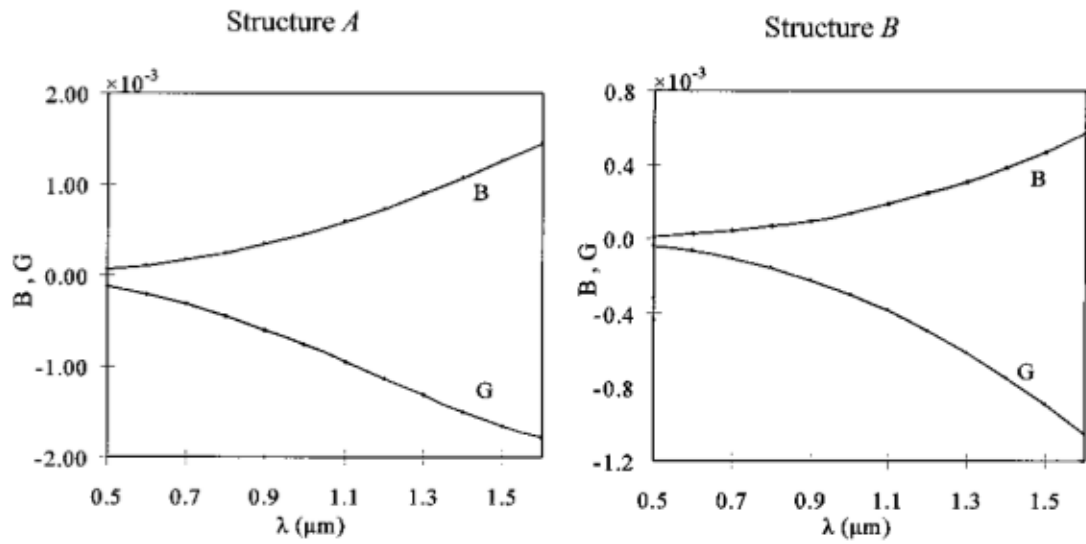


Figure 2.19. Calculated group and phase modal birefringence at different wavelength [59].

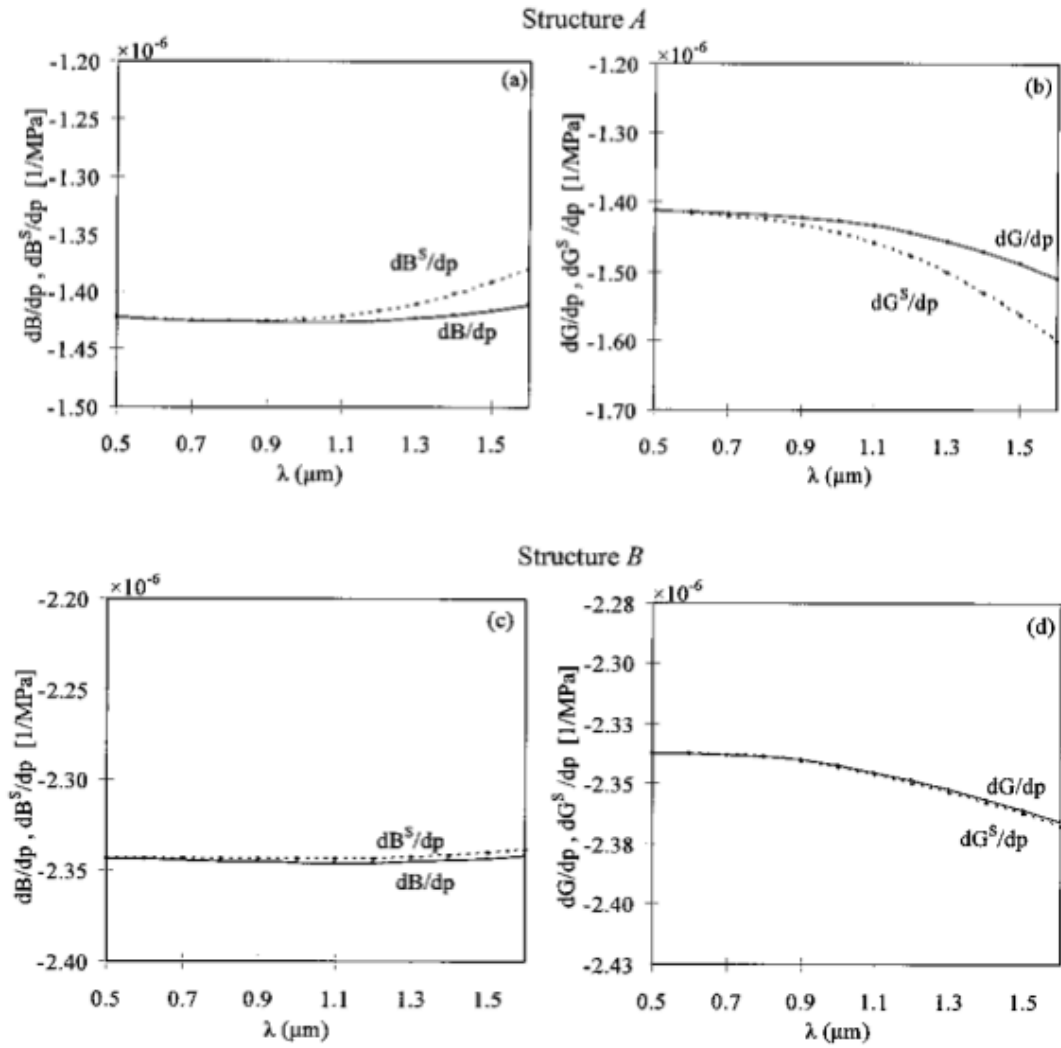


Figure 2.20. (a) (b) Pressure sensitivity of phase and group modal birefringence of structure A; (c)(d) Pressure sensitivity of phase and group modal birefringence of structure B [59].

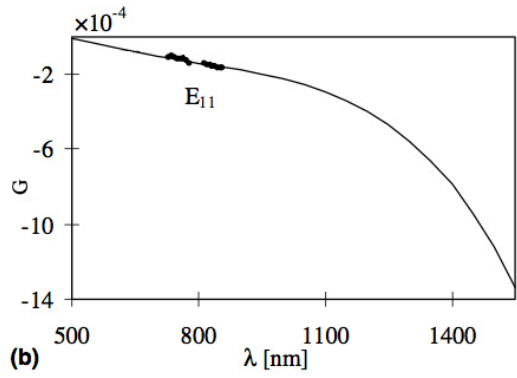
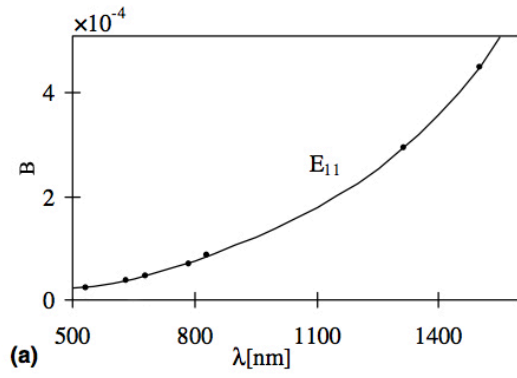


Figure 2.21. Experimental results of the PCF's phase and modal birefringence at different wavelength [60].

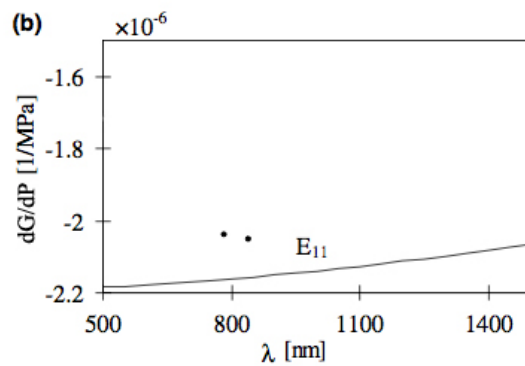
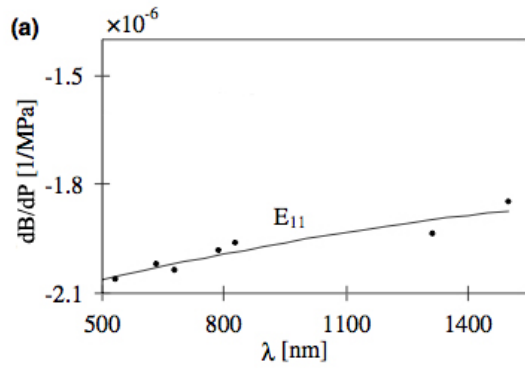


Figure 2.22. Experimental results on pressure sensitivity of (a) phase (b) group modal birefringence at different wavelength [60].

Pressure sensor based on PM-PCF was reported by T. Martunkien et. al [61]. Instead of using commercially available PM-PCF from Blaze Photonic, Inc., two PM-PCFs of different designs were proposed. About 0.5 m section of the fibre was put in the pressure or temperature chamber. Linealy polarized light beam was adjusted at 45° to the fibre's axis to excite both polarization modes. Such method is similar to the one used in [56]. Phase shift against pressure change was measured. For the pressure sensitivity, both types of the presented fibre were about -43 rad/MPa·m at 1550 nm. The temperature sensitivities of the 2 presented fibre were -0.044 rad/K·m and -0.08 rad/K·m. So 1 K of temperature change would be equivalent to 0.001 MPa and 0.0019 MPa. This shows about 5 times improvement than the sensor reported in [55].

Fu et. al [62] proposed and demonstrated a pressure sensor design which used the PM-PCF to form a Sagnac loop. The fibre used was the same design as in [59][60], from Blaze Photonics Inc.. A 3 dB coupler was used and a section of the PM-PCF was spliced to the two output ports of the 3 dB single mode fibre coupler. Broadband light source was used and the transmission spectrum of the sensor was monitored by optical spectrum analyser (OSA). The sensor was put inside an air pressure chamber for pressure measurement up to 0.3 MPa. When pressure changes, the birefringence changes and the transmission spectrum of the sensor shifts. The sensor's spectral shift was measured. The transmission spectrum of the sensor is given by [62]

$$T = \frac{1}{2} \cdot \left[ 1 - \cos \left( \frac{2\pi BL}{\lambda} + \frac{2\pi K_p \Delta PL}{\lambda} \right) \right]. \quad (2.29)$$

The first term in the cosine function is the phase difference caused by the fibre's intrinsic birefringence and the second term is by the birefringence induced by

pressure.  $K_P$  is the birefringence-pressure coefficient of the PM-PCF. The spacing between the adjacent minima is

$$S = \frac{\lambda^2}{BL} . \quad (2.30)$$

The spectral shift can be given by

$$\Delta\lambda = \frac{K_P \lambda}{B} \Delta P \quad (2.31)$$

According to equation (2.31), the spectral shift is independent of the PM-PCF length. 58.4 cm of the PM-PCF was put to test. Operation wavelength was centred at 1550 nm. The spacing found was ~5.3 nm. The group birefringence was about  $7.8 \times 10^{-4}$ . The sensitivity was 3.42 nm/MPa. Two other sensors of 40 and 79.6 cm long of PM-PCF were tested. Their sensitivity were 3.46 and 3.43 nm/MPa respectively. All the three sensors showed similar sensitivity, which supports that the sensor's sensitivity is independent of the PM-PCF's length. The temperature sensitivity was also measured to be -2.2 pm/°C, which means 1 K temperature change corresponds to  $0.64 \times 10^{-3}$  MPa, which is even smaller than the sensor reported in [61].

Further experiment on larger pressure range was reported in [63]. The sensor was placed in a hydraulic pressure chamber. Pressure was applied up to 20 MPa. The sensitivity was 3.24 nm/MPa. Another test was done with wavelength centred at 1320 nm. The sensitivity was 4.21 nm/MPa.

## **2.5 Conclusions**

The development of FBG and its thermal decay property is reviewed. Traditional sensors for flow measurement are discussed. The optical fibre counterpart of those flow sensors and other optical flow sensors are further discussed.

The basic principle of Sagnac interferometer is described. Development of fibre optic based pressure sensor is reviewed. Different designs based on single mode fibre, PM fibre and PCF are discussed. The temperature sensitivity of those sensors showed clearly PM-PCF based sensor is much insensitivity to temperature, which is crucial for sensor solely for pressure measurement in downhole applications.

## Chapter 3

### Fibre optic thermal anemometer

#### 3.1 Introduction

Hot-wire anemometer is one of the most popular types of flowmeter. The underlying principle of hot-wire anemometer is convective heat transfer. The development history of hot-wire anemometry is more than a century, dating back to the beginning of the 19<sup>th</sup> century [23]. The first kind of hot-wire anemometer introduced was based on constant current operation [23][25]. Then, more researches were carried out on keeping the temperature of the hot-wire constant [26]. The Wheatstone bridge to hot-wire anemometer proposed by Weske [27] has formed the basis of today's electronic based hot-wire anemometer.

No significant amount of research work has been carried out on fibre optic based thermal anemometry. The benefits of pure fibre optic sensors include electrically passive, EMI immunity, low attenuation over long distance, easy to multiplex, etc [13]. These are the most important incentives for research on fibre optic thermal anemometer. However, the main challenge is believed to be the difficulty in heating up the optical fibre.

Different efforts were reported to heat up the optical fibre. Early research works used electricity to generate heat. Either external heating element [39] or metal coating on the optical fibre [40] was used. Bobb [40] coated a gold metal film on the surface of the optical fibre. Conducting wires were connected to the metal film to pass electric current through the metal film and the electric current heated the gold metal film up.

These systems cannot fully utilize the benefits of fibre optic sensors as they still rely on electricity.

Later, purely optic solutions were proposed. As mentioned in chapter 2, Lamb et al. [41] published their work using a CO<sub>2</sub> laser to heat up the optical fibre. The high power CO<sub>2</sub> laser beam externally hit the optical fibre to generate heat. This design was intended to measure electric wind of corona discharge. Such setup has a major issue in most applications. The sensor is too bulky and requires free space optic to heat up the sensor. Work by Chen et al. [42] suggested coating a silver film on single mode fibre with FBG inscribed. 910 nm laser light was carried by multimode fibre and spliced to the single mode fibre with FBG and coating. The light of the 910 nm laser leaked into the cladding of the single mode fibre and absorbed by the silver coating and heat was generated. Jawart et al. [43] of the same group proposed the use of sensor design reported in [42] for thermal anemometry. Similar design was also reported by Caldas et al. [44] as flow sensor, except long period grating was used instead of multimode fibre to couple the 910 nm laser light to the cladding of the sensor's single mode fibre.

Except the design in [41] with large physical size, one common property of all the other designs was the use of metal. The potential problem of metal is oxidation, under high temperature the rate of oxidation is high. This will be a significant problem in practical system.

Silica doped with different transition metal elements have strong absorption at different wavelengths. According to Schultz et al. [64] and Davis et al. [46], the absorption and optical to thermal efficiency of cobalt and vanadium doped fibre can be summarized as

Cobalt:

- High absorption around 500 nm to 750 nm and beyond 1200 nm.
- Optical to thermal efficiency with 700 nm – 720 nm was 38%.

Vanadium

- High absorption around 500 nm to 1300 nm.
- Optical to thermal efficiency around 700 nm – 720 nm was 56%.

These suggest that both types of the doped fibre can be used as a self-heating optical fibre sensor for thermal anemometry.

In this chapter, a self-heating pure fibre optic FBG based anemometer is proposed. The benefit of this pure fibre optic design is that it is totally electrically passive and totally metal coating free at the sensor head. Thus, this design is free from metal oxidation and resistance in conducting metal wire as in the electric heating method.

### **3.2 Fabrication and structure of the sensor**

The self-heating fibre used is high absorption cobalt doped optical fibre with core diameter around 8  $\mu\text{m}$  from CorActive High-Tech Inc.. 4 types of high attenuation fibre were used. The attenuation of the fibres are 3 dB/cm, 5 dB/cm, 7 dB/cm and 9.7 dB/cm respectively. Attenuation values were measured at 1310 nm and 1550 nm. To measure the temperature change, FBGs were inscribed into the high absorption fibre. Around 7 - 9 mm section of the high absorption fibre were prepared and with two ends spliced to SMF28 single mode fibre. FBGs are fabricated by 193 nm ArF excimer laser by the phase mask technique. FBGs were inscribed to be sufficiently long to cover the whole section of the high absorption fibre. After the FBG

fabrication process, the high absorption fibre was cleaved at the two ends to trim it to 5 mm long. Its two ends were spliced to another two SMF28 single mode fibres. This process ensures that the FBG is covering the whole 5 mm section of the high absorption fibre and nothing is inscribed in the single mode fibres. The sensor configuration is shown in figure 3.1.

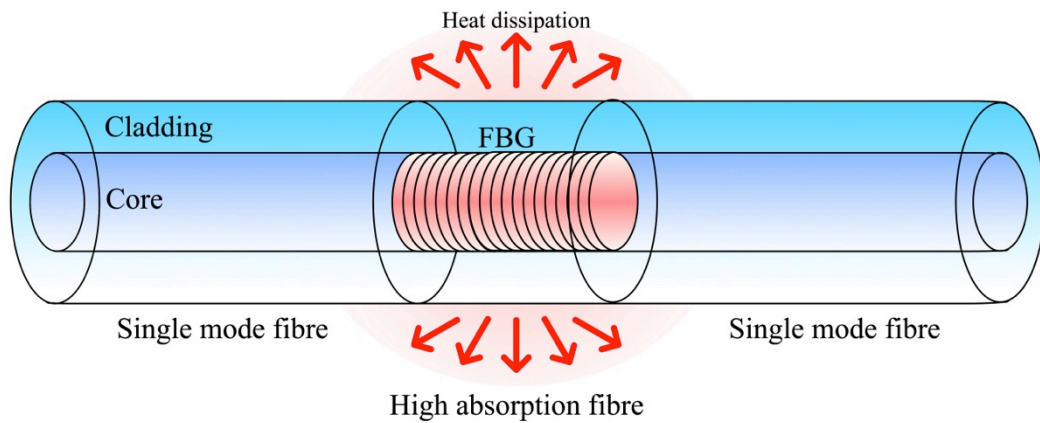


Figure 3.1. Fibre optic heat generating thermal anemometry flow sensor configuration

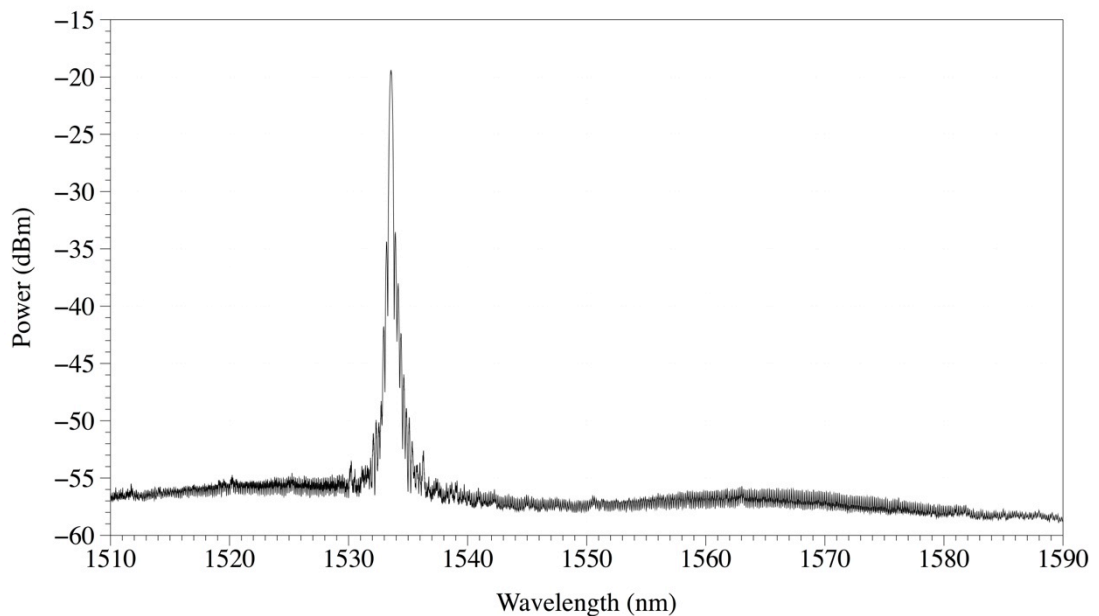


Figure 3.2. Reflection spectrum of the FBG inscribed in the 9.7 dB/cm high absorption fibre

The high power pumping laser light and the probe light from the optical fibre interrogator are carried by the core. The high absorption fibre absorbs laser light and convert the optical energy to thermal energy. The centre reflection wavelength of the

FBG inscribed in the high absorption fibre reflects the temperature of the high absorption fibre. The reflection spectrum measured by an optical fibre interrogator was shown in Figure 3.2. Figure 3.3 shows the temperature response of the high absorption fibre in air at different absorbed power. The temperature was measured using the FBG inscribed in the high absorption fibre. The temperature can reach nearly 600°C above ambient temperature with ~ 330 mW absorbed optical power.

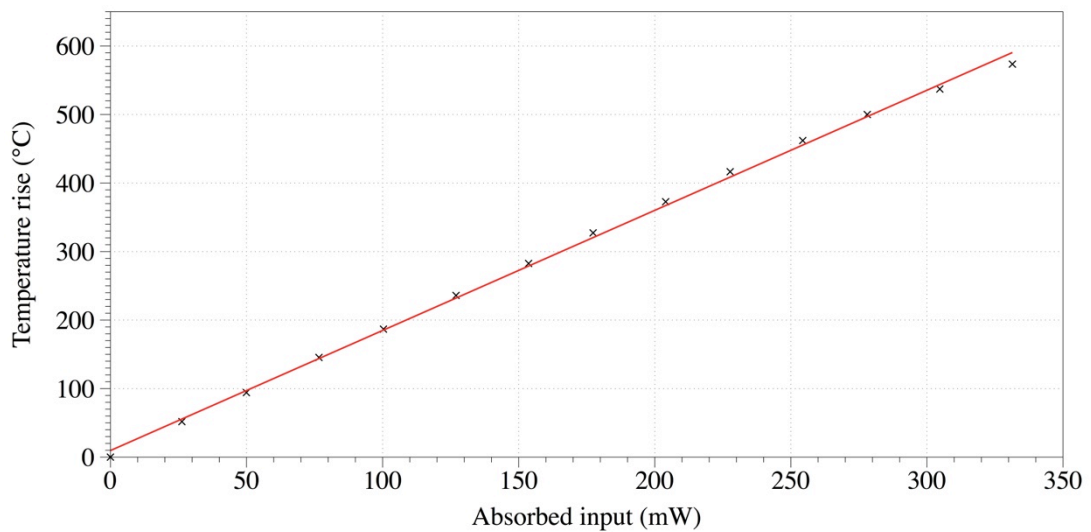


Figure 3.3. Temperature rise of the high absorption fibre at different absorbed pump power

### 3.3 Experiment design and results

Experiment was carried out to measure the response of this self heating fibre. Figure 3.4 shows the optical setup of the high absorption fibre based thermal anemometer. The pump laser is IPG Laser GmbH PYL-2-1455-R, operating at 1455 nm with maximum power output measured to be around 1.2 W. The output of the pump laser first passed through a 99:1 single mode coupler. 1% of the output power was directed to another 99:1 coupler. In total, 0.01% of the pump laser power was directed to an ILX FPM-8200 fibre optic power meter for laser output power monitoring. The other 99% of the pump laser optical power was directed to a

wavelength division multiplexer (WDM) where the pump laser was multiplexed with the output of the Micron Optics, Inc. SM130 optical fibre interrogator in the range of 1510 - 1590 nm. The multiplexed pump light then reached the high absorption fibre. A portion of the 1455 nm pump laser was absorbed by the high absorption fibre and converted into heat. The FBG in the high absorption fibre was fabricated with centre wavelength within the optical fibre interrogator measurement range. The FBG reflect the light with centre wavelength changes related to the temperature of the high absorption fibre. The reflected light then passes through the WDM and then enters the interrogator. The remaining power after passing through the high absorption fibre was measured by an ILX FPM-8210H optical power meter. The heating of the high absorption fibre was mainly due to the high power 1455 nm pump laser as the output of the interrogator was less than 0.25 mW, which was much weaker.

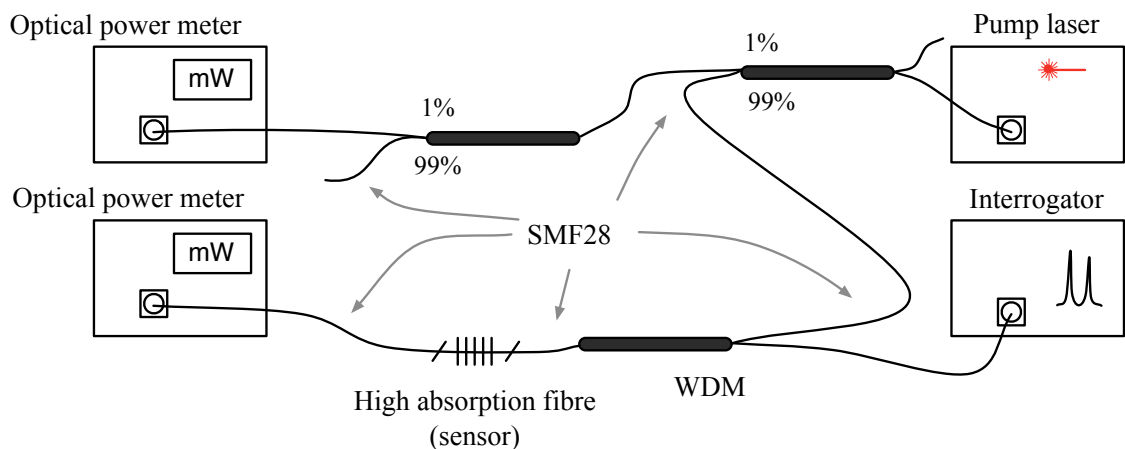


Figure 3.4. Optical setup of the high absorption fibre for flow measurement

Figure 3.5 illustrates the setup to measure the response of the high absorption fibre to air flow speed. A wind tunnel was build to reduce the turbulence of the flowing air. A Testo 405-V1 electronic hot-wire anemometer was used as the reference. The optical fibre flow sensor was placed at the centre of the wind tunnel in front of the reference hot-wire anemometer, with the two ends penetrating through the walls of

the wind tunnel. The optical fibre was slightly stretched to avoid fluctuation with the slight turbulence of the air flow.

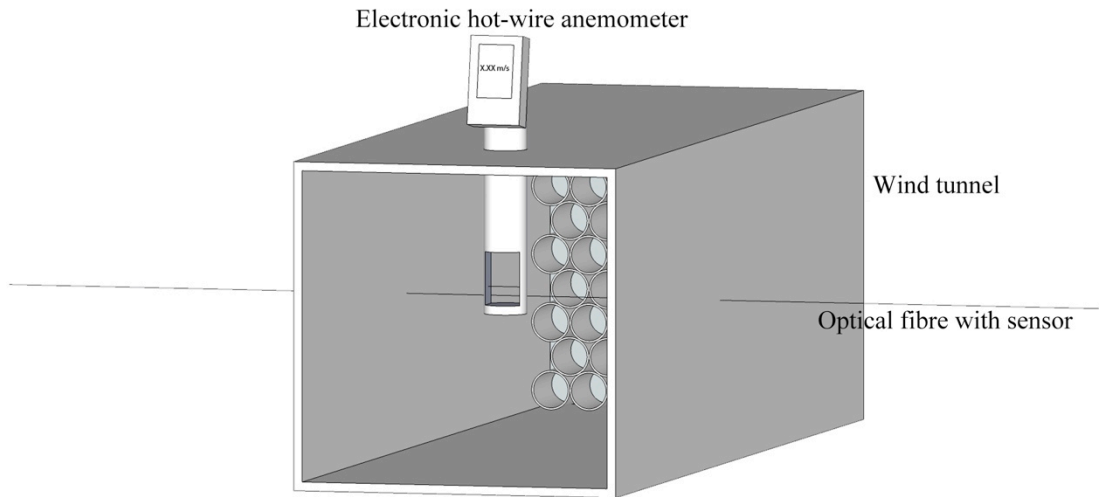


Figure 3.5. Flow measurement setup

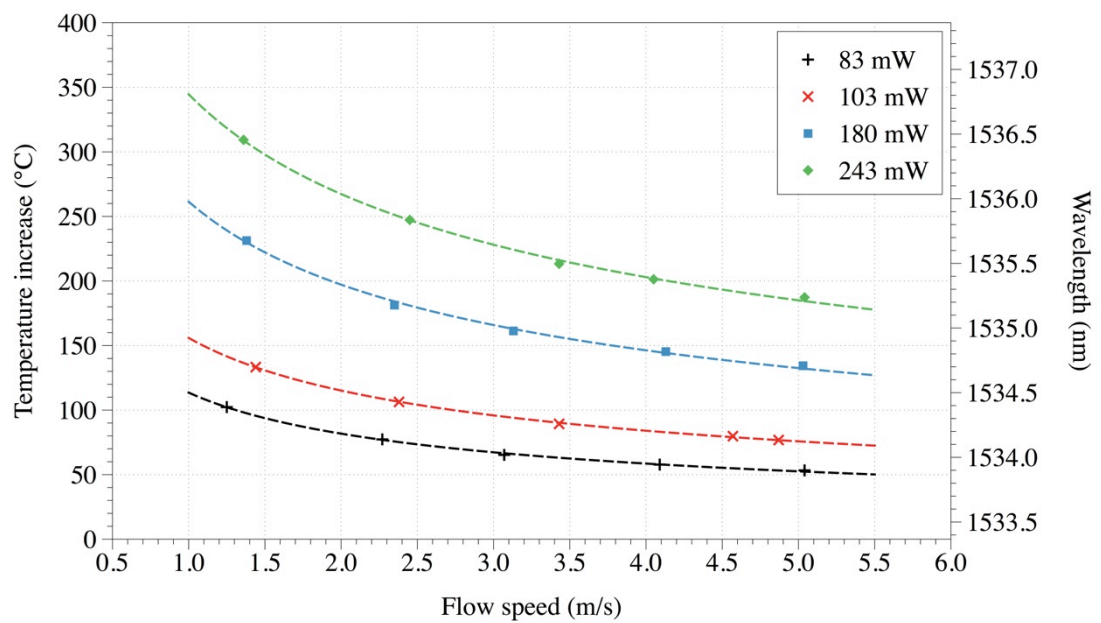


Figure 3.6. Response of the sensor at different flow speed

Figure 3.6 shows the response of the high absorption fibre. Experiments were conducted at different absorption power level. The response of hot-wire anemometer can be represented by [29]

$$P = (A + Bv^n)(T_{fibre} - T_a). \quad (3.1)$$

$P$  is the optical power being absorbed,  $T_{fibre}$  is the temperature of the high absorption fibre,  $T_a$  is the ambient temperature.  $A$ ,  $B$  and  $n$  are empirical constants to be determined by experiment. The dotted curves in Figure 3.6 are curve fitted to the experimental results with the constant  $n$  set to 0.45. The fitted curves match with the experimental data well. The values of  $A$  and  $B$  at different absorbed power level are plotted in figure 3.7.

The figure shows the parameter  $A$  increases with the absorbed power while parameter  $B$  decreases when the absorbed power increases. The sensitivity of the anemometer against flow speed can be calculated by differentiating equation (3.1). It is given by

$$\frac{dT_{fibre}}{dv} = -P \frac{Bv^{-0.55}}{(A + Bv^{0.45})^2}. \quad (3.2)$$

Figure 3.8 shows the sensitivity of the sensor at different absorbed power level. It is clear that increasing the power level increases the sensitivity of the sensor.

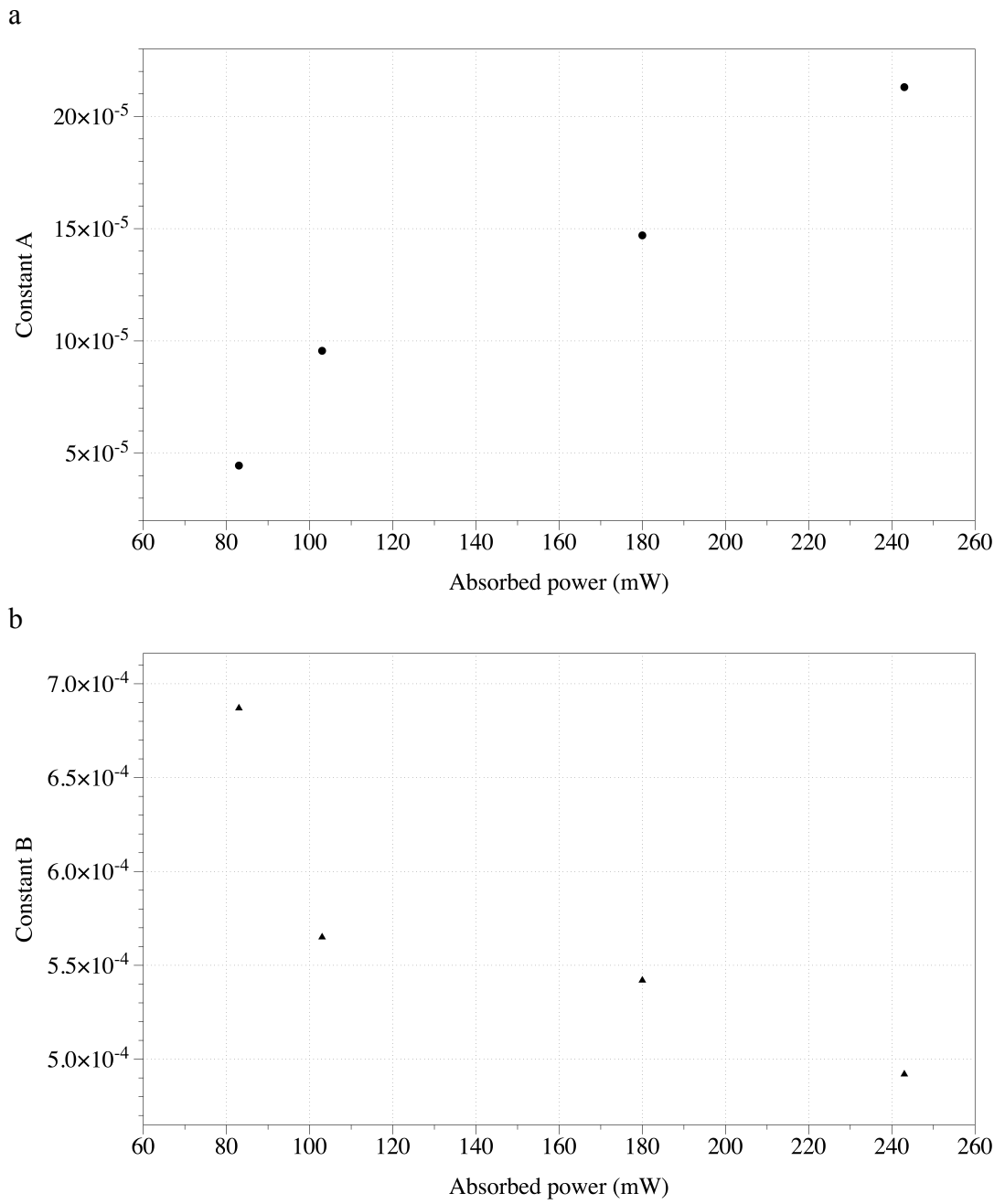


Figure 3.7(a). Empirical constant A and (b) constant B of the high absorption fibre at different absorbed power level

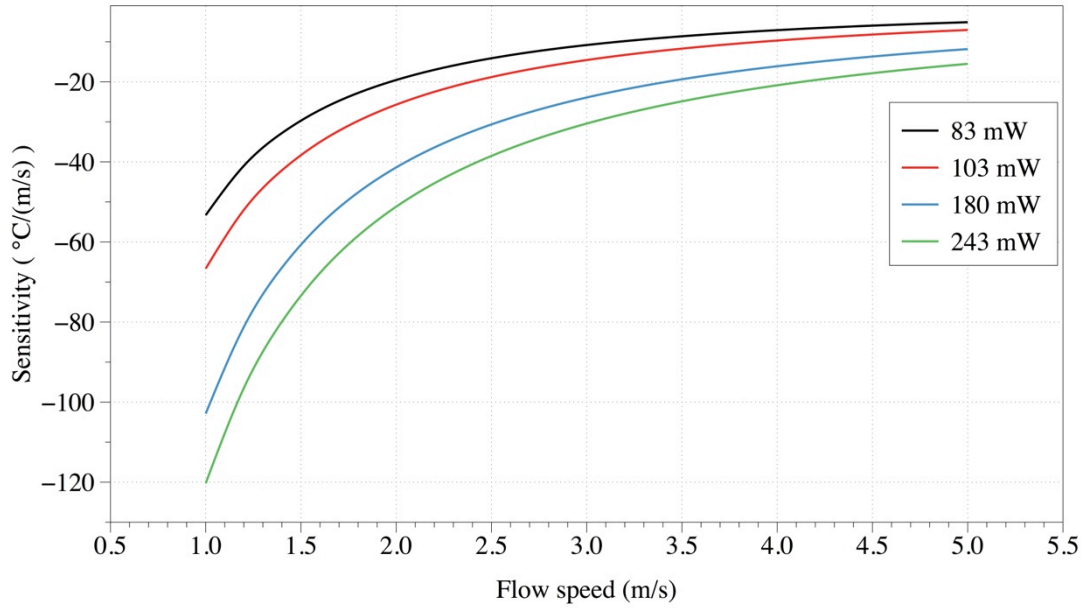


Figure 3.8. Sensitivity of the high absorption fibre versus flow speed.

### 3.4 Equation development

Experiments showed that the sensor's sensitivity drops with increasing flow speed or decreasing absorbed power. The results were curve fitted to equation 3.1 and the sensitivities against flow speed were calculated based on the values of empirical constant  $A$  and  $B$  obtained through curve fitting the experimental results. No estimation on the response of the sensor can be made without experimentally finding out the value of  $A$  and  $B$ .

The development of equations for estimating the response of the sensor with only the readily available physical and thermal properties parameters would be useful to trim the sensor's response in future developments.

An optical fibre can be treated as an cylinder. The general form of heat diffusion equation in cylindrical coordinate is given by [65]

$$\frac{1}{r} \frac{\partial}{\partial r} \left( kr \frac{\partial T}{\partial r} \right) + \frac{1}{r^2} \frac{\partial}{\partial \phi} \left( k \frac{\partial T}{\partial \phi} \right) + \frac{\partial}{\partial z} \left( k \frac{\partial T}{\partial z} \right) + \dot{q} = \rho c_p \frac{\partial T}{\partial t}. \quad (3.3)$$

$k$  is thermal conductivity,  $T$  is temperature,  $\dot{q}$  is the thermal power generation  $P_{gen}$  is per unit volume and is equal to  $P_{gen}/(\pi r^2 L)$ ,  $\rho$  is density,  $c_p$  is specific heat capacity and  $t$  is time. The first term on the left side of the equation gives the heat diffusion along the radius of the cylinder. The second term gives the heat diffusion in the azimuthal direction and the third term is heat diffusion along the cylinder  $z$  direction. The fourth term is the power generation. The right side of the equation is the stored energy change in the cylinder.

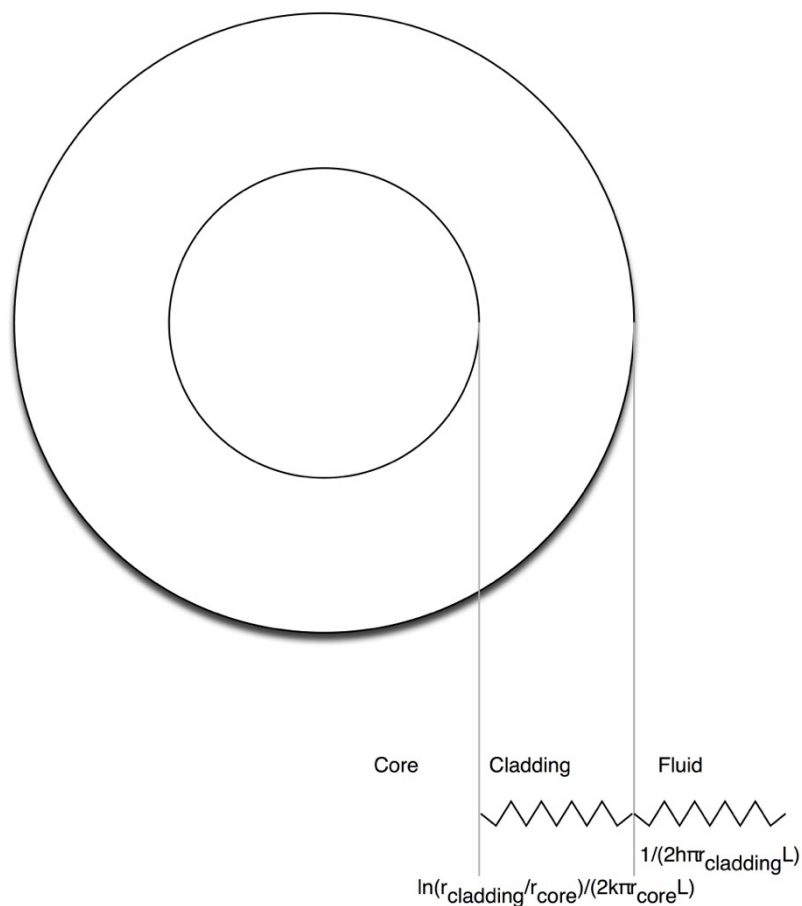


Figure 3.9. Graphical illustration of cross section of the high absorption fibre and the thermal resistance of the cladding and the fluid

Figure 3.9 gives the graphical illustration of the high absorption fibre and the corresponding thermal resistance. In the high absorption fibre, the diffusion of heat

is assumed to be mainly in the radial direction. Diffusion in the other two axes are neglected. In steady state operation of constant power operation, there is no net change in energy, so the right side of equation (3.3) is 0. In the core of the high absorption fibre where optical power is converted into thermal energy, equation (3.3) now becomes

$$\frac{1}{r} \frac{\partial}{\partial r} \left( r \frac{\partial T}{\partial r} \right) + \frac{\dot{q}}{k_{fibre}} = 0. \quad (3.4)$$

$k_{fibre}$  is the thermal conductivity of the optical fibre and  $0 \leq r \leq r_{core}$ ,  $r_{core}$  is the core radius. By integrating the above equation,

$$r \frac{\partial T}{\partial r} = -\frac{r^2 \dot{q}}{2k_{fibre}} + A, \quad (3.5)$$

where  $A$  is a constant. Integrating equation (3.5) gives

$$T(r) = -\frac{r^4 \dot{q}}{4k_{fibre}} + \ln(r)A + B, \quad (3.6)$$

where  $B$  is a constant. In the core of the high absorption fibre, when  $r$  is equal to the core radius  $r_{core}$ , the temperature is  $T_{s,core}$ , the surface temperature of core. At the centre of the core, there is no temperature gradient. So, at  $r=0$ ,  $\frac{\partial T}{\partial r} = 0$ .

With the above information, we can compute the value of constant  $A$  is 0,  $B$  is

$$B = T_{r,core} + \frac{r_{core}^2 \dot{q}}{4k_{fibre}}. \text{ Putting them in to equation (3.6) gives}$$

$$T(r) = \frac{\dot{q}}{4k_{fibre}} (r_{core}^2 - r^2) + T_{s,core}, \quad (3.7)$$

where  $0 \leq r \leq r_{core}$ .

Equation (3.7) shows that the temperature gradient inside the core is linear.

In the cladding of the high absorption fibre, there is no heat generation as no light is absorbed there. So, equation (3.3) is expressed as

$$\frac{k_{fibre}}{r} \frac{\partial}{\partial r} \left( r \frac{\partial T}{\partial r} \right) = 0. \quad (3.8)$$

where  $r_{core} \leq r \leq r_{cladd}$ ,  $r_{cladd}$  is the radius of the cladding. Integrating the above equation gives

$$\frac{\partial T}{\partial r} = \frac{C}{r}, \quad (3.9)$$

where  $C$  is a constant. Integrating equation (3.10) gives

$$T(r) = \ln(r)C + D, \quad (3.10)$$

where  $D$  is a constant. At  $r$  equals to the core radius  $r_{core}$ ,  $T(r) = T_{s,core}$ . At  $r$  equals to the cladding radius  $r_{cladd}$ ,  $T(r) = T_{s,cladd}$ , where  $T_{s,cladd}$  is the surface temperature of the cladding. Substituting these conditions into equation (3.10), we have

$$T_{s,core} = \ln(r_{core})C + D, \quad (3.11)$$

$$T_{s,cladd} = \ln(r_{cladd})C + D. \quad (3.12)$$

Equating the above two equations gives

$$T(r) = \frac{T_{s,core} - T_{s,cladd}}{\ln(r_{core}/r_{cladd})} \ln\left(\frac{r}{r_{cladd}}\right) + T_{s,cladd}. \quad (3.13)$$

The above equation is valid only for  $r_{core} \leq r \leq r_{cladd}$ .

The heat transfer rate is given by

$$q = -kA \frac{dT}{dr}. \quad (3.14)$$

$A$  is the area normal to the direction of heat transfer.  $A=2\pi rL$ .

Using equation (3.14), the heat transfer rate in the cladding is

$$q_{cladd} = -k_{fibre} 2\pi L \frac{T_{s,core} - T_{s,cladd}}{\ln(r_{core}/r_{cladd})}. \quad (3.15)$$

Thermal resistance is defined as the ratio of the temperature potential to the rate of heat transfer. The thermal resistance of the cladding is given by

$$R_{cladd} = \frac{\ln(r_{cladd}/r_{core})}{k_{fibre} 2\pi L}. \quad (3.16)$$

In the high absorption fibre, heat is generated in the core but not the cladding, the core can be treated as a heater and cladding as an insulating layer. The heat generated in the core diffuses through the cladding to the surface. When the fluid is flowing across the high absorption fibre, the heat is brought away mainly by forced convection. The power transfer by convection is represented by

$$P_{conv} = hA\Delta T, \quad (3.17)$$

where  $h$  is the convection coefficient,  $A$  is the surface area of the high absorption wire and  $\Delta T$  is the temperature difference between the ambient fluid temperature and

the surface temperature of the high absorption fibre. The thermal resistance of convection can be represented by

$$R_{conv} = \frac{1}{h2\pi r_{cladd} L}. \quad (3.18)$$

In steady state operation, there is no net change in stored energy. So the rate of energy generation is equal to the rate of energy dissipation. Which means that

$$P_{gen} = h2\pi r_{cladd} L (T_{s,cladd} - T_a), \quad (3.19)$$

where  $T_a$  is the ambient temperature. Rearranging equation (3.19) gives

$$T_{s,cladd} = \frac{P_{gen}}{h2\pi r_{cladd} L} + T_a. \quad (3.20)$$

As heat generated in the core of the high absorption fibre diffuses through the cladding to the flowing fluid, the rate of heat transfer is constant in these regions. So

$$P_{conv} = P_{gen} = q_{cladd}$$

$$P_{gen} = -k2\pi L \frac{T_{s,core} - T_{s,cladd}}{\ln(r_{core}/r_{cladd})}$$

$$T_{s,core} = \frac{P_{gen} \ln(r_{cladd}/r_{core})}{k_{fibre} 2\pi L} + T_{s,cladd}. \quad (3.21)$$

Substituting equation (3.21) to (3.7) we have

$$T(r) = \frac{P_{gen}}{2\pi L} \left[ \frac{1}{2k_{fibre}} \left( 1 - \frac{r^2}{r_{core}^2} \right) + \frac{\ln(r_{cladd}/r_{core})}{k_{fibre}} + \frac{1}{hr_{cladd}} \right] + T_a, \quad (3.22)$$

where  $0 \leq r \leq r_{core}$ .

To find the relationship between the convection coefficient  $h$  and the flow speed  $v$ , the Reynolds number and Nusselt number have to be found. Reynolds number  $Re$  is the ratio of inertial force to viscous force. This number tells which force is dominating in the system. Nusselt number  $Nu$  is a ratio of convective heat transfer to conductive heat transfer. The Reynolds and Nusselt number for a cylinder in cross flow are given by

$$Re = \frac{2r_{cladd}v}{\nu}, \quad (3.33)$$

$$Nu = \frac{2r_{cladd}h}{k_{fluid}}. \quad (3.34)$$

$\nu$ ,  $v$  and  $k_{fluid}$  are the kinematic viscosity, flow speed and thermal conductivity of the fluid respectively. For the boundary layer to be laminar,  $Re < 2 \times 10^5$ . In 1977, Churchill [66] gave the empirical correlation of Nusselt number as

$$Nu = 0.3 + \frac{0.62 Re^{0.5} Pr^{1/3}}{\left[1 + (0.4/Pr^{2/3})\right]^{0.25}} \left[1 + \left(\frac{Re}{282,000}\right)^{5/8}\right]^{0.8}. \quad (3.35)$$

$Pr$  is the Prandtl number of the fluid, which is the ratio of kinematic viscosity to thermal diffusivity. Putting equation (3.33) into (3.35), we have

$$Nu = 0.3 + \frac{0.62(2r_{cladd})^{0.5} Pr^{1/3} v^{0.5}}{v^{0.5} \left[1 + (0.4/Pr^{2/3})\right]^{0.25}} \left[1 + \left(\frac{r_{cladd}h}{141,000k_{fibre}}\right)^{5/8} v^{5/8}\right]^{0.8}. \quad (3.36)$$

For convenience, we let

$$\chi = \frac{0.62(2r_{cladd})^{0.5} Pr^{1/3}}{v^{0.5} \left[1 + (0.4/Pr^{2/3})\right]^{0.25}} \quad (3.37)$$

and

$$\beta = \left( \frac{r_{cladd}}{141,000\nu} \right)^{5/8}. \quad (3.38)$$

Substituting equation (3.36) to (3.34),  $h$  is given by

$$h = \frac{k_{fluid} \left[ 0.3 + \chi\nu^{0.5} (1 + \beta\nu^{5/8})^{0.8} \right]}{2r_{cladd}}. \quad (3.39)$$

Substituting equation (3.39) to (3.20), the surface temperature of the cladding can be equated to the flow speed  $\nu$ .

$$T_{s,cladd} = \frac{P_{gen}}{\pi L k_{fluid}} \left[ 0.3 + \chi\nu^{0.5} (1 + \beta\nu^{5/8})^{0.8} \right]^{-1} + T_a. \quad (3.40)$$

The temperature distribution in the core is found by substituting equation (3.39) to (3.22).

$$T(r) = \frac{P_{gen}}{2\pi L} \left\{ \frac{1}{2k_{fibre}} \left( 1 - \frac{r^2}{r_{core}^2} \right) + \frac{\ln(r_{cladd}/r_{core})}{k_{fibre}} + \frac{2}{k_{fluid} \left[ 0.3 + \chi\nu^{0.5} (1 + \beta\nu^{5/8})^{0.8} \right]} \right\} + T_a, \quad (3.41)$$

where  $0 < r < r_{core}$ . The average temperature of the core is

$$T_{core} = \frac{1}{r_{core}} \int_0^{r_{core}} T(r) dr$$

$$T_{core} = \frac{P_{gen}}{2\pi L} \left\{ \frac{1 + 3\ln(r_{cladd}/r_{core})}{3k_{fibre}} + \frac{2}{k_{fluid} \left[ 0.3 + \chi v^{0.5} (1 + \beta v^{5/8})^{0.8} \right]} \right\} + T_a \quad (3.42)$$

$$T_{core} = \frac{P_{gen}}{2\pi L} \left[ \frac{1 + 3\ln(r_{cladd}/r_{core})}{3k_{fibre}} \right] + T_{s,cladd}$$

Average temperature of the cladding is

$$T_{cladd} = \frac{1}{r_{cladd} - r_{core}} \int_{r_{core}}^{r_{cladd}} T(r) dr$$

$$= T_{s,core} - T_{s,cladd} \left[ \frac{1}{\ln(r_{cladd}/r_{core})} - \frac{r_{core}}{r_{cladd} - r_{core}} \right] + T_{s,cladd} \quad (3.43)$$

Figure 3.10 shows the temperature distribution inside the fibre at 3 m/s air flow speed and 243 mW of absorbed power. The thermal conductivity of the high absorption fibre is assumed constant. The temperature variation in the core is about 2.8 °C and the variation in the cladding is about 15.2 °C.

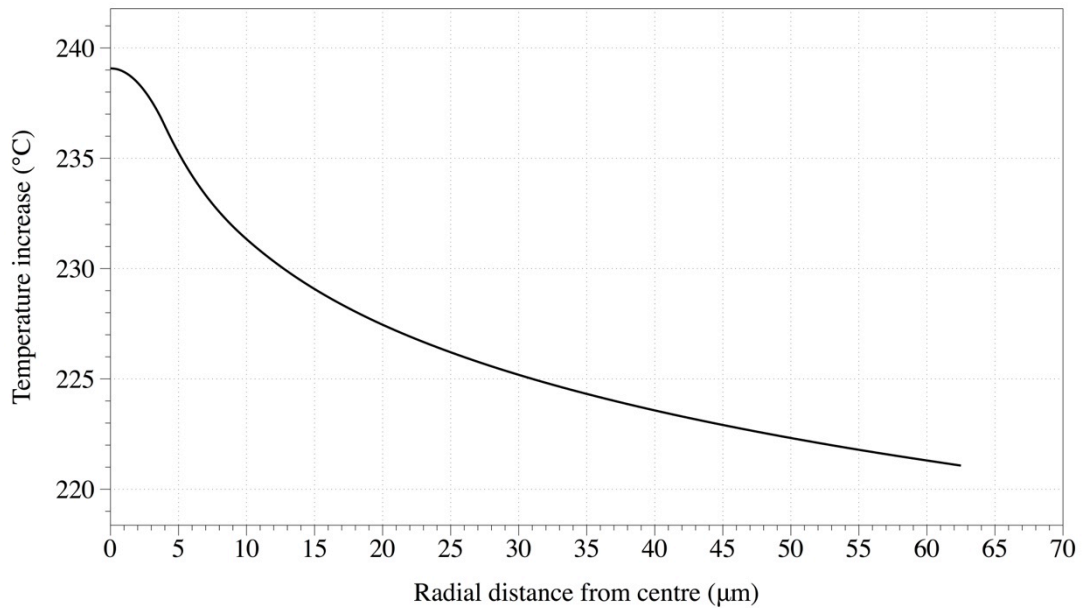


Figure 3.10. Temperature distribution in radial direction of the high absorption fibre with air flow speed at 3 m/s

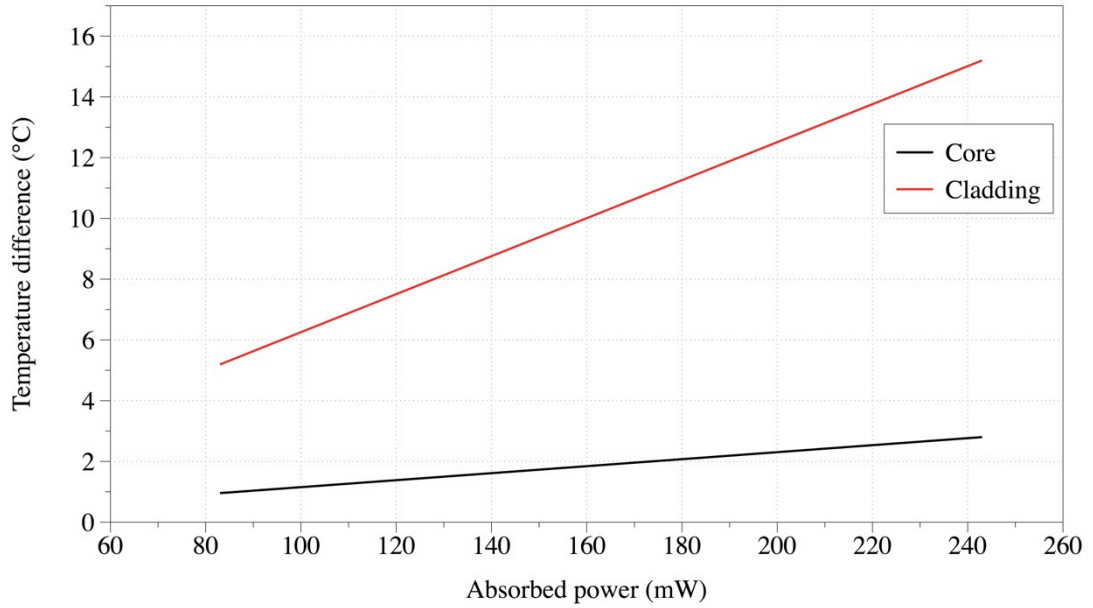


Figure 3.11. Temperature difference in the core and cladding at different absorbed power level. Figure 3.11 shows the temperature differences in the core (core centre temperature minus  $T_{s,core}$ ) and the cladding ( $T_{s,cladd} - T_{s,core}$ ) of the high absorption fibre. The temperature difference increase when the absorbed power increases.

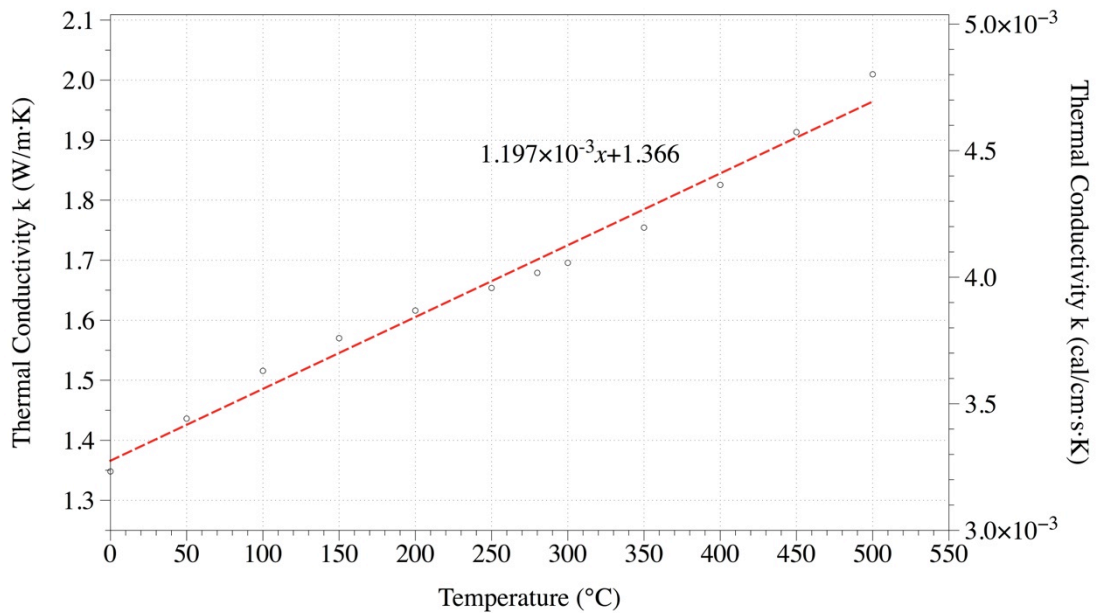


Figure 3.12. Thermal conductivity of fused silica

Figure 3.12 shows the thermal conductivity of fused silica against temperature. The figure is plotted with data from Sugawara's work [67]. A linear curve is fitted to the data points. The fitted equation is

$$k_{\text{fibre}} = 1.197 \times 10^{-3} T + 1.366. \quad (3.44)$$

The rate of change of thermal conductivity is  $2.858 \times 10^{-6}$  (W/m·K)/°C. Figure 3.13 shows the percentage difference of the thermal conductivity in the cladding at 6 m/s air flow speed. The difference from the average thermal conductivity in the cladding is less than 1%. This indicates the variation in thermal conductivity in the high absorption fibre can be neglected.

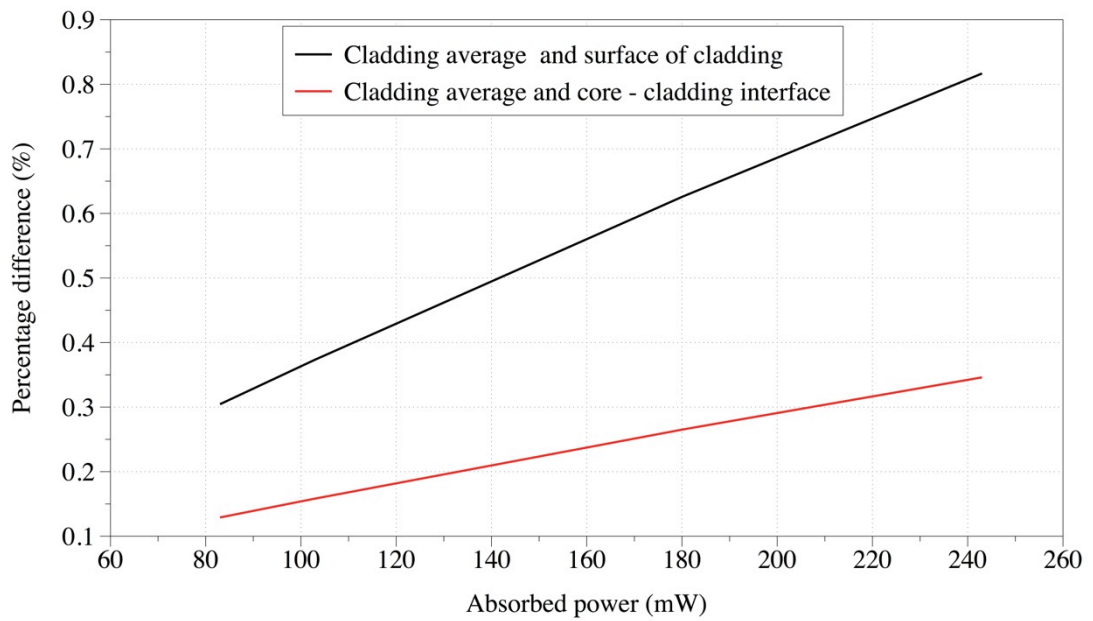


Figure 3.13. Percentage difference in thermal conductivity in the cladding. Black line shows the percentage difference between the average of the cladding and the outer surface of the cladding. The red line shows the difference between the cladding average and the core – cladding interface.

Despite the small variation in the cladding, the thermal conductivity of the sensor would change when the temperature of the sensor change significantly caused by different absorbed power level or ambient temperature. To improve the accuracy of the equations, equation (3.44) is substituted into equation (3.42).

$$T_{core} = \left\{ \left( 570.59 - 0.5T_{s,cladd} \right)^2 + 1141.19T_{s,cladd} + \frac{P_{gen}}{7.182 \times 10^{-3} \pi L} \left[ 1 + 3 \ln \left( \frac{r_{cladd}}{r_{core}} \right) \right] \right\}^{0.5} - 570.59 + 0.5T_{s,cladd} \quad (3.45)$$

The sensitivity of the sensor can be calculated by differentiating the above equation with respect to the velocity  $v$ .

$$\frac{dT_{core}}{dv} = T_{core}'(T_{s,cladd}) T_{s,cladd}'(v), \quad (3.46)$$

where

$$T_{core}'(T_{s,cladd}) = \frac{1}{2} + \frac{1}{2} \left\{ \left( 570.59 - 0.5T_{s,cladd} \right)^2 + 1141.19T_{s,cladd} + \frac{P_{gen}}{7.182 \times 10^{-3} \pi L} \left[ 1 + 3 \ln \left( \frac{r_{cladd}}{r_{core}} \right) \right] \right\}^{-0.5} \times \left( 570.59 + 0.5T_{s,cladd} \right), \quad (3.47)$$

$$T_{s,cladd}'(v) = \frac{-P_{gen} \left[ 0.5\chi v^{-0.5} (1 + \beta v^{5/8})^{0.8} + 0.5\chi v^{0.5} (1 + \beta v^{5/8})^{-0.2} \beta v^{-3/8} \right]}{\pi L k_{fluid} \left[ 0.3 + \chi v^{0.5} (1 + \beta v^{5/8})^{0.8} \right]^2}. \quad (3.48)$$

According to equation (3.48),  $T_{s,cladd}'(v)$  is independent of the core diameter  $r_{core}$ . In equation (3.47),  $r_{core}$  is included in the natural log function inside the large bracket. Despite the existence of  $r_{core}$ , its variation causes slight impact as the term is much smaller than the first two terms in the large bracket. So, the variation in the core diameter  $r_{core}$  is negligible. Table 3.1 gives some of the physical properties of air and optical fibre in room temperature. Figure 3.14 shows the simulated sensor's sensitivity against the variation in core size at 243 mW absorbed power and 1 m/s air flow speed. The results are obtained with the values listed in table 1. For the core

size changing from 8.3  $\mu\text{m}$  to 50  $\mu\text{m}$ , the sensitivity change from -143.92  $^{\circ}\text{C}/(\text{m/s})$  to -144.62  $^{\circ}\text{C}/(\text{m/s})$ . Increase in core diameter of 502.41 % only cause the sensitivity to increase by 0.49%. This suggests that changing the core diameter does not significantly change the sensitivity.

Table 3.1. Physical properties of air and the high absorption fibre

<b>Fluid – Air at Room Temperature</b>	
Density $\rho$ ( $\text{kg}/\text{m}^3$ )	1.184
Kinematic Viscosity $\nu$ ( $\text{m}^2/\text{s}$ )	$1.589 \times 10^{-5}$
Prandtl Number $Pr$	0.707
Thermal Conductivity $k$ ( $\text{W}/\text{m}/\text{K}$ )	0.0236
<b>High Absorption Optical Fibre</b>	
Thermal Conductivity of Fused Silica at Room Temperature $k$ ( $\text{W}/\text{m}/\text{K}$ )	1.38
Core Radius (Single Mode) $r_{core}$ (m)	$4.15 \times 10^{-6}$
Core Radius (Multimode) $r_{core}$ (m)	$25 \times 10^{-6}$
Cladding Radius $r_{cladd}$ (m)	$62.5 \times 10^{-6}$

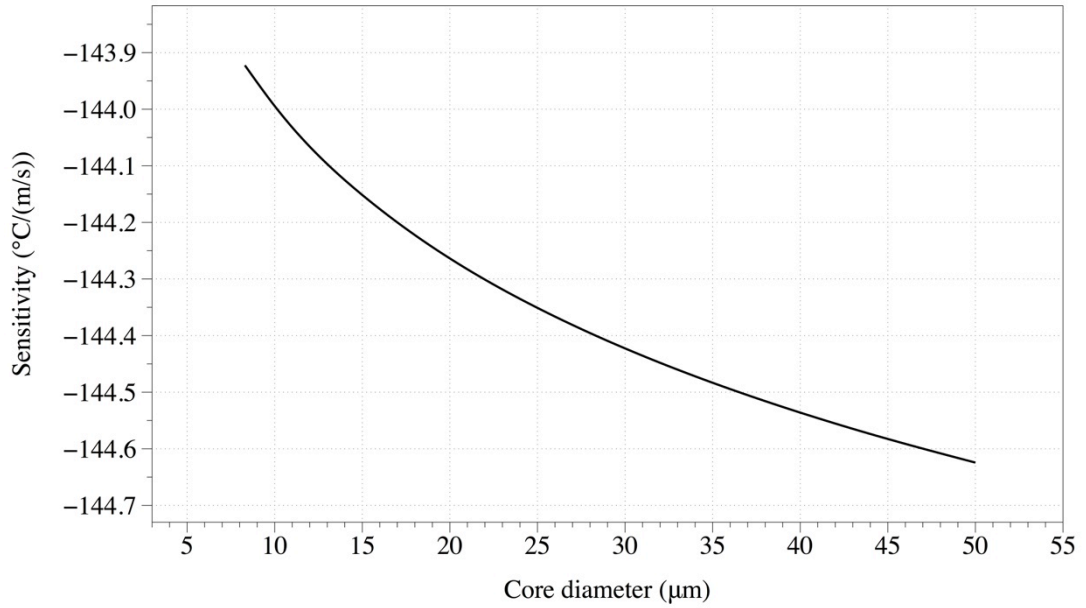


Figure 3.14. Sensitivity against core size at 1 m/s and 243 mW absorbed power.

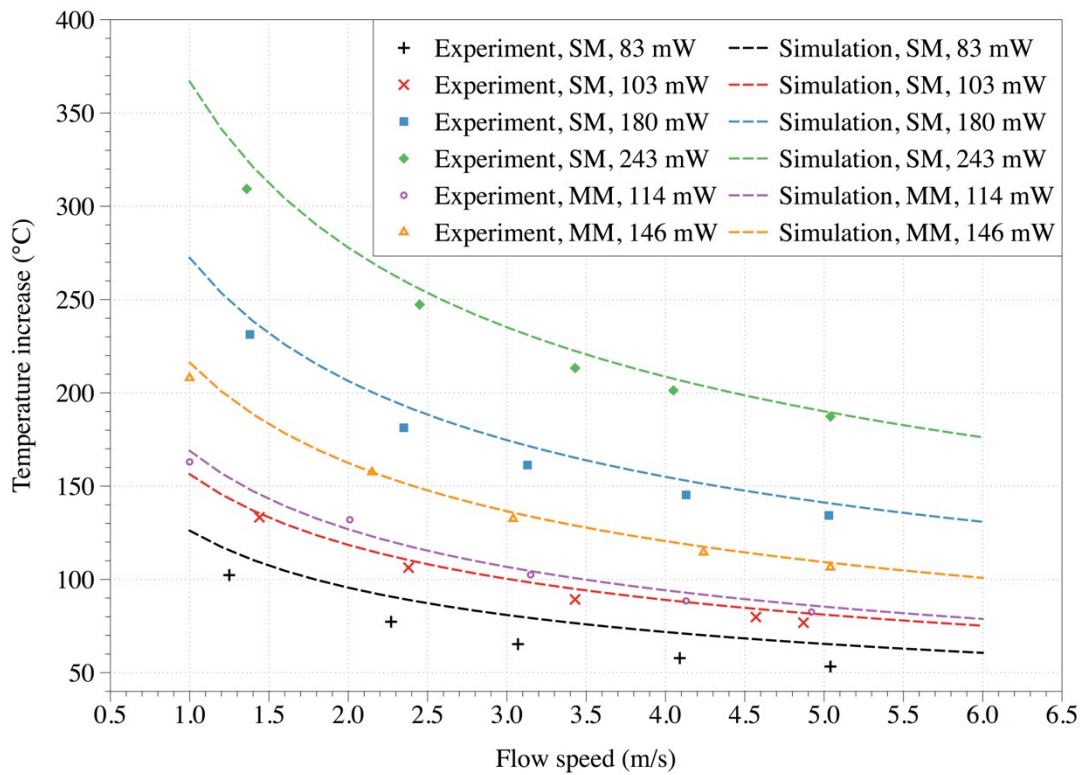


Figure 3.15. Flow response of the single mode (SM) high absorption fibre (core diameter: 8.3 μm) and the multimode (MM) high absorption fibre (core diameter: 50 μm) and the corresponding simulation results.

Figure 3.15 shows the response of the high absorption fibre of different core size to the air flow speed. The core diameter of the single mode high absorption fibre is  $8.3 \mu\text{m}$  and the multimode fibre is  $50 \mu\text{m}$ . Simulated results are also plotted. The simulated results match well with the experimental results of both the single and multimode high absorption fibre's flow response. The results suggest nearly 100% of the absorbed optical energy converts to thermal energy.

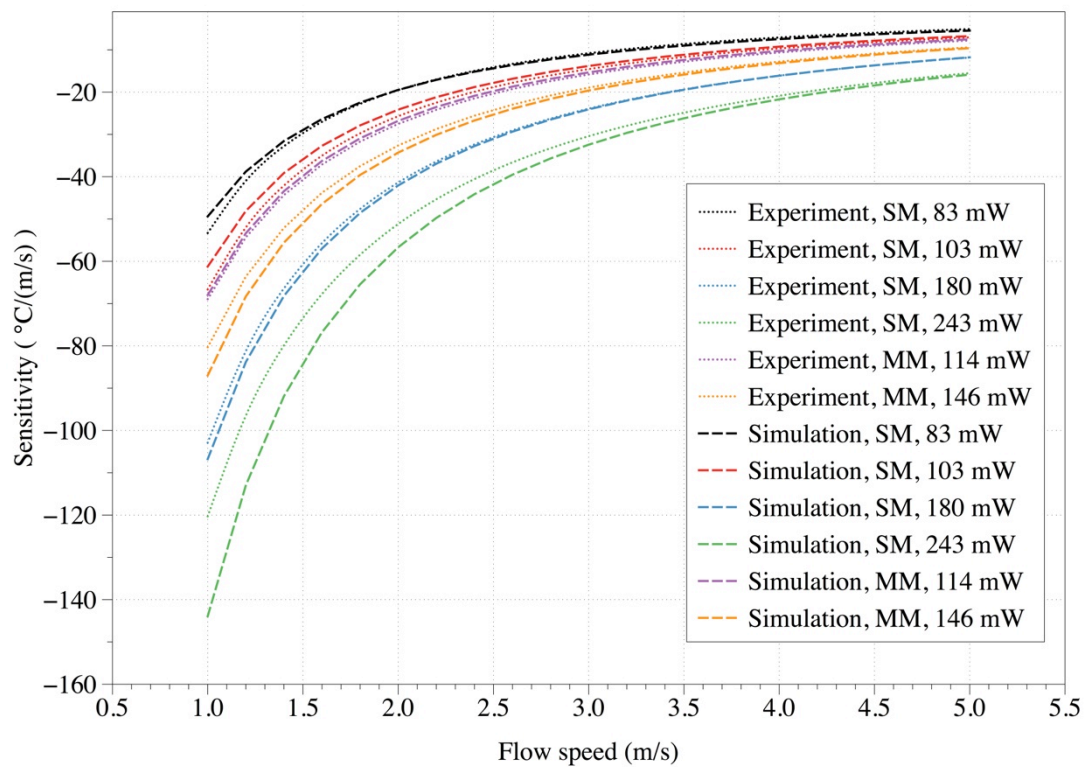


Figure 3.16. Experimental and simulated sensitivity of the single mode high absorption fibre and the multimode high absorption fibre at different flow speed.

Figure 3.16 shows both the simulated and the experimental results of both the single mode and multimode high absorption fibre. The simulated results and experimental results are generally similar. This shows previous prediction that variation in core diameter does not significantly alter the sensitivity of the sensor. One way to alter the sensor's sensitivity is to alter the outer diameter of the sensor. Equation (3.47)

and (3.48) depends on  $T_{s,cladd}$ ,  $\chi$ , and  $\beta$ . These parameters all depend on the cladding radius  $r_{cladd}$ . This suggest altering the cladding diameter (i.e. the outer diameter of the sensor) change the flow sensitivity of the high absorption fibre. Figure 3.17 illustrates the simulated results of the sensor's flow sensitivity when the outer diameter is altered. The absorbed power used for simulation is 243 mW and the graph gives the flow sensitivity at 6 m/s and 1 m/s flow speed. The figure shows increase in flow sensitivity when the outer radius decreases. The diameter used for simulation start from 125  $\mu\text{m}$ , which is the cladding diameter of the high absorption used, down to 60  $\mu\text{m}$ . Such a decrease in cladding diameter of 52% causes the flow sensitivity at 1 m/s air flow to increase by 24% and at 6 m/s air flow to increase by 34%.

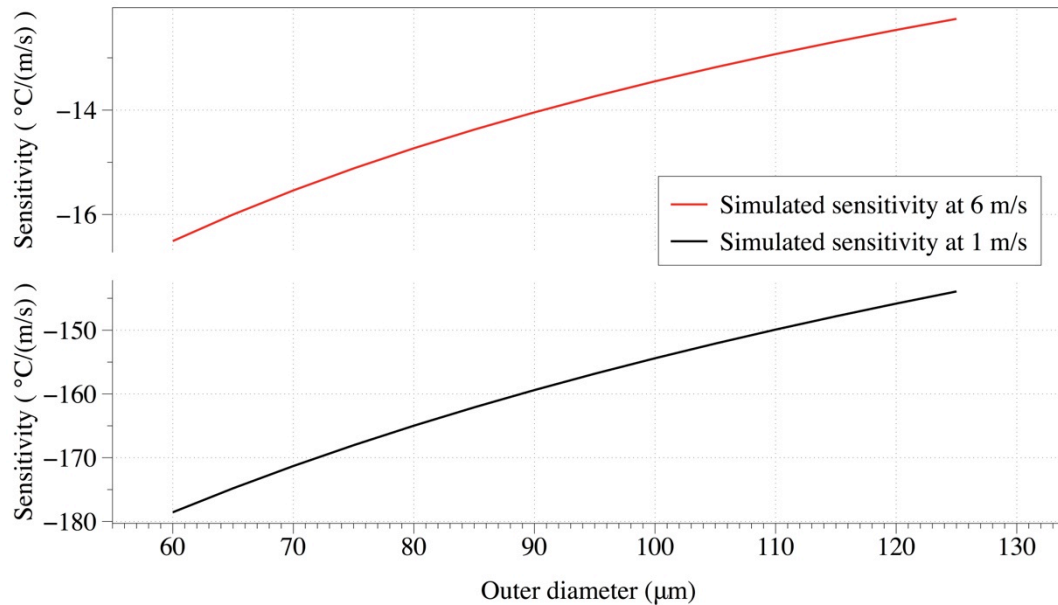


Figure 3.17. Simulated flow sensitivity of the high absorption fibre of different outer diameter at 6 m/s and 1 m/s. The absorbed power used for simulation is 243 mW.

This shows that instead of increasing the power of the pump laser, decreasing the radius of the cladding radius of the high absorption fibre should increase the sensitivity.

### **3.5 Thermal decay of the sensor**

The high absorption fibre used for thermal anemometry as stated above runs at elevated temperature. To enhance the flow sensitivity of the sensor, the output power of the pump laser has to be increased. This increases the optical power absorbed by the fibre and hence the temperature of the fibre goes higher. This elevated temperature working condition causes the reflectivity of the sensor to decrease faster. Thermal decay of this optical fibre thermal anemometer has to be evaluated. Experiments were carried out to find out the thermal decay of the grating on the high absorption fibre. The attenuation of the high absorption fibre used was 7 dB/cm. Four samples of high absorption fibre with each of them connected both sides to SMF-28 standard single mode fibre are studied. The temperature tested were about 140 °C, 310 °C, 370 °C and 500 °C. The reflectivity of the FBGs were about 35 % - 40 %. Figure 3.18 and 3.19 show the transmission spectrum and reflection spectrum of the FBG inscribed in the high absorption fibre in an oven with temperature around 310 °C. The reflectivity of the FBG decay rapidly at first, then slow down as time advances.

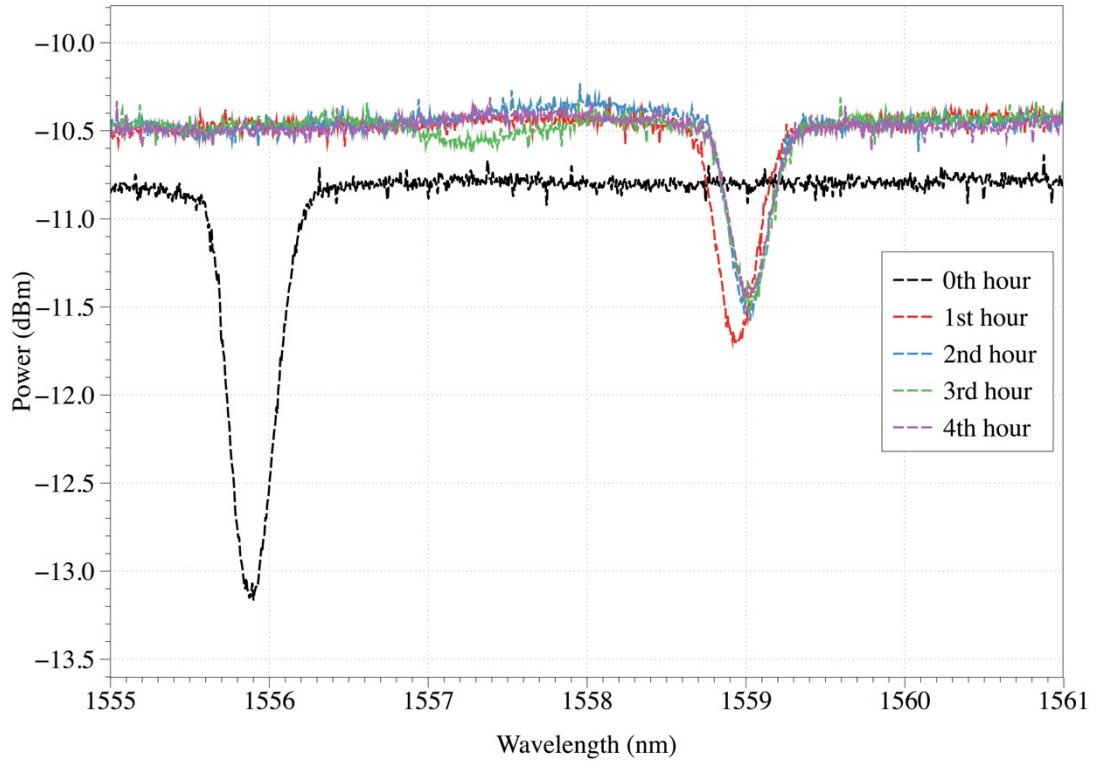


Figure 3.18. Transmission spectrum of the high absorption fibre at about 310 °C at different time

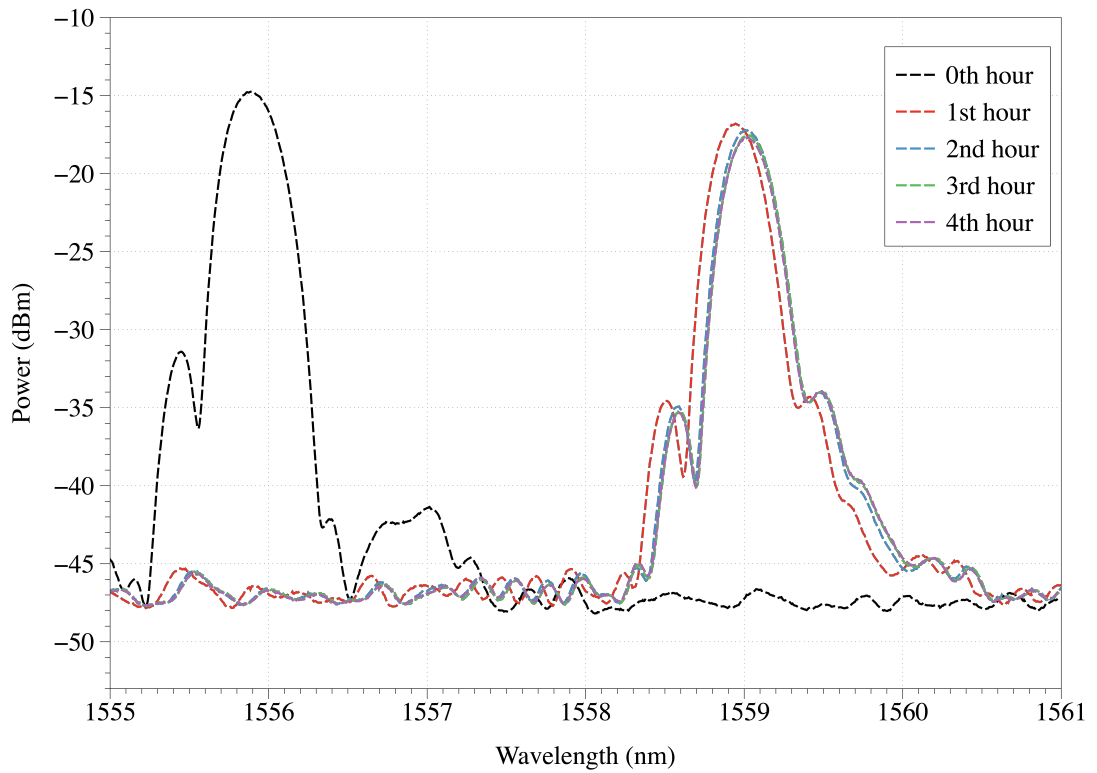


Figure 3.19. Reflection spectrum of the high absorption fibre at about 310 °C at different times

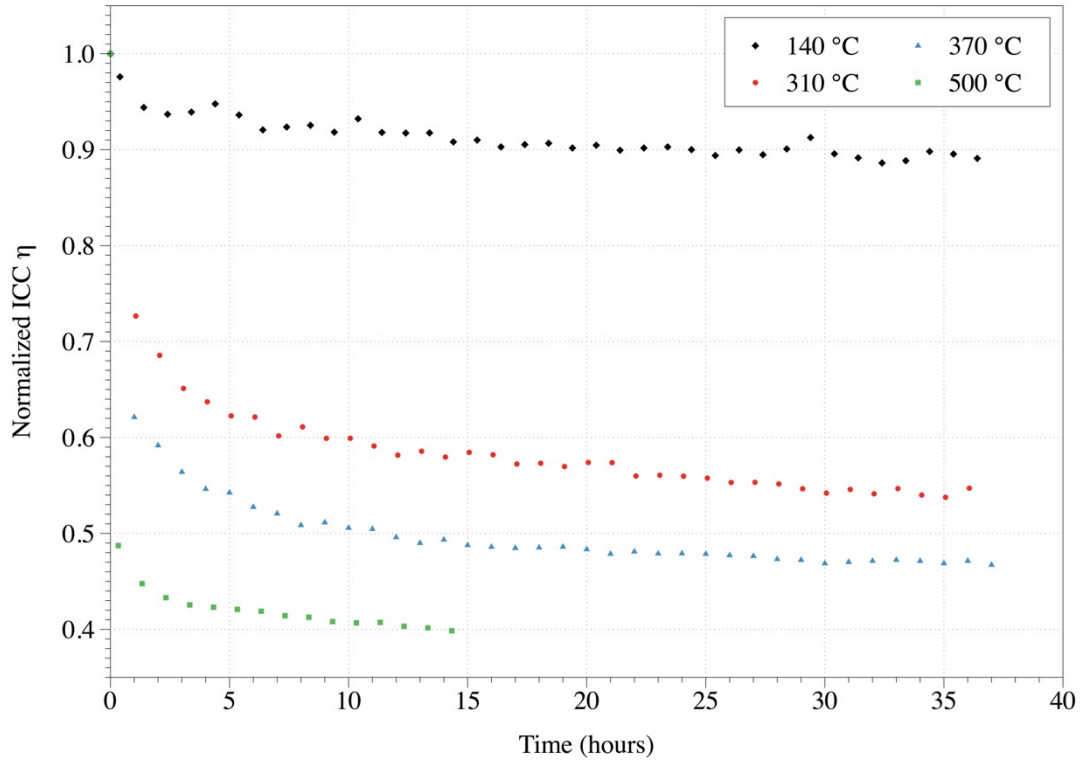


Figure 3.20. Decay of FBG inscribed in the high absorption fibre at different temperature and time

Figure 3.20 shows the change in the normalized integrated coupling constant (ICC)  $\eta$  against the change in time. The reflectivity drops more significantly at higher temperature. To relate these results together, the aging curve approach is used as suggested by Kannan et. al [15]. This method is more general than the power law approach.

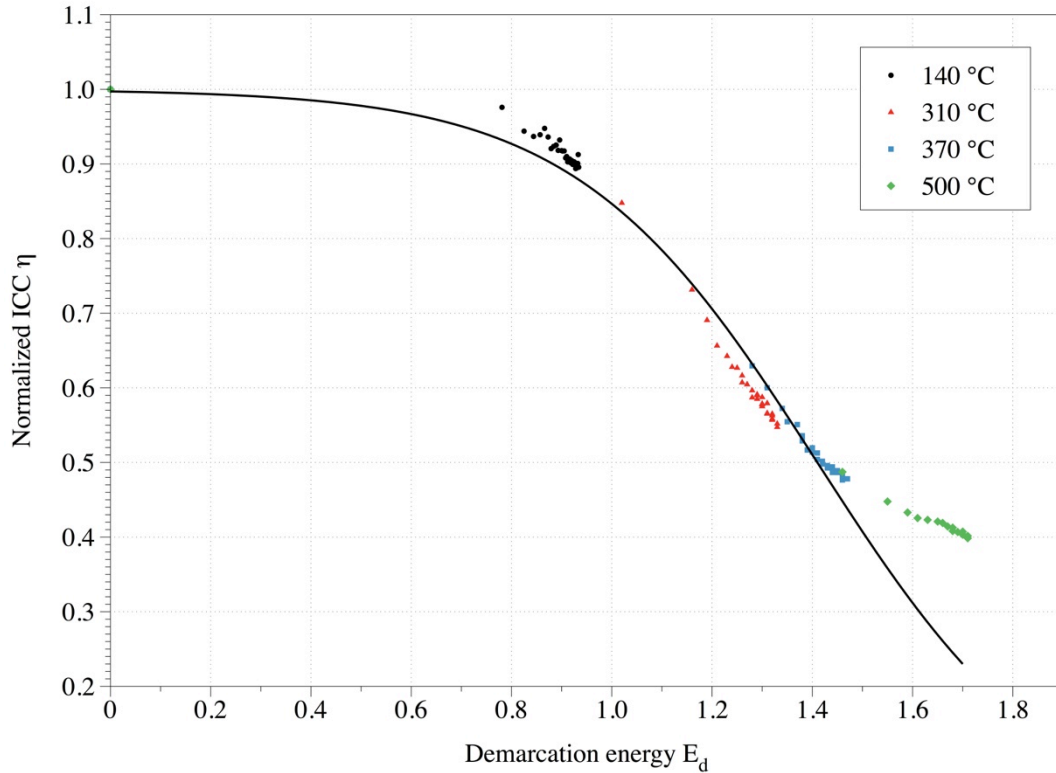


Figure 3.21. The normalized integrated coupling constant of the FBGs inscribed in the high absorption fibre against the demarcation energy

Figure 3.21 shows how the normalized integrated coupling constant  $\eta$  at different temperatures changes against the demarcation energy  $E_d$ . The demarcation energy is  $E_d = k_B T \ln(v_0 t)$ , where  $v_0$  is obtained by curve fitting the experimental data.  $v_0$  was found to be about  $1 \times 10^{-10}$  to yield good results. The  $\eta$  is related to  $E_d$  by  $\eta = 1 / [1 + \exp(E_d - 1.41) / 0.24]$ .

### 3.5 Water flow measurement

The possibility of using high absorption fibre to measure liquid flow was evaluated. Experiments were carried out to study the performance of the sensor in water flow measurement.

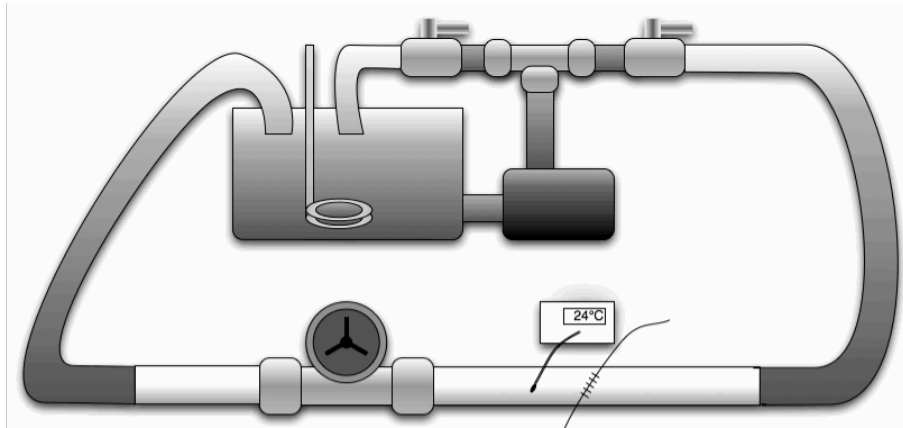


Figure 3.22. Experimental setup for measuring water flow

Figure 3.22 shows the experimental setup of the water flow measurement. A large water tank was used as a reservoir. An opening in the tank's wall was connected to the inlet of a water pump. The pump's output was connected to a T-shape joint. On one of the outputs of the T-joint was a direct path back to the water tank and is controlled by a ball valve. The other side of the output was connected to the test chamber water pipe where the sensor was inserted, through a ball valve that control the flow rate to the testing chamber. The water flowing in the test chamber water pipe first met the high absorption fibre based thermal flowmeter, then a thermocouple which is connected to a thermometer. Finally, the water met the rotary liquid flowmeter. The rotary liquid flowmeter was a Gems Sensors 15626BSPP-RS with low flow adaptor installed, which is capable to measure the volumetric flow rate from 1.5 to 12 GPM. The volumetric flow rate can be converted back to the flow speed in the test chamber water pipe by  $v=R/(\pi r^2)$ , where  $R$  is the volumetric flow rate and  $r$  is the internal radius of the test chamber water pipe. The internal diameter of the pipe was 12.5 mm. The measurable flow range was around 0.77 to 6.15 m/s. The output of the rotary flowmeter is square waves, and its frequency is related to the volumetric flow rate. The output was connected to an Agilent 54622D Mixed

Signal Oscilloscope and the frequency was measured. The connection of the high absorption fibre was the same as in Figure 3.4. The sensor was protected by a tiny silica tube with external diameter of around 0.4 mm. This silica tube help protect the FBG from measuring the strain applied on the fibre when the water flow across it.

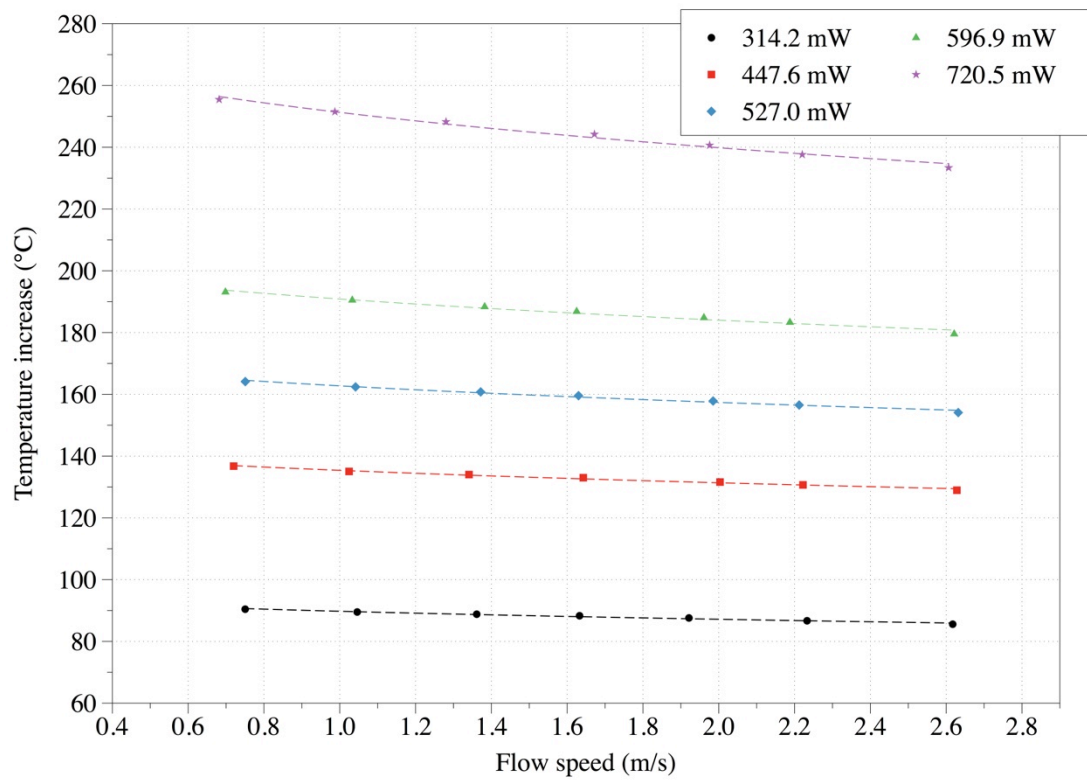


Figure 3.23. Sensor response at different absorbed power level

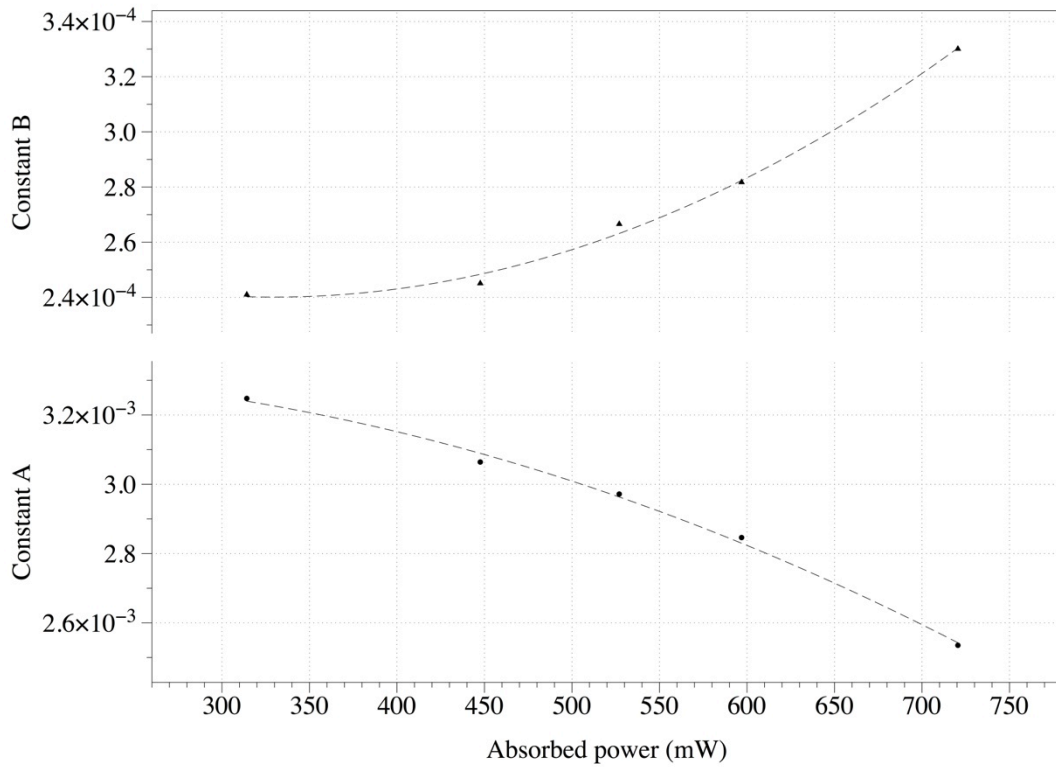


Figure 3.24. Constant A and B at different absorbed power level

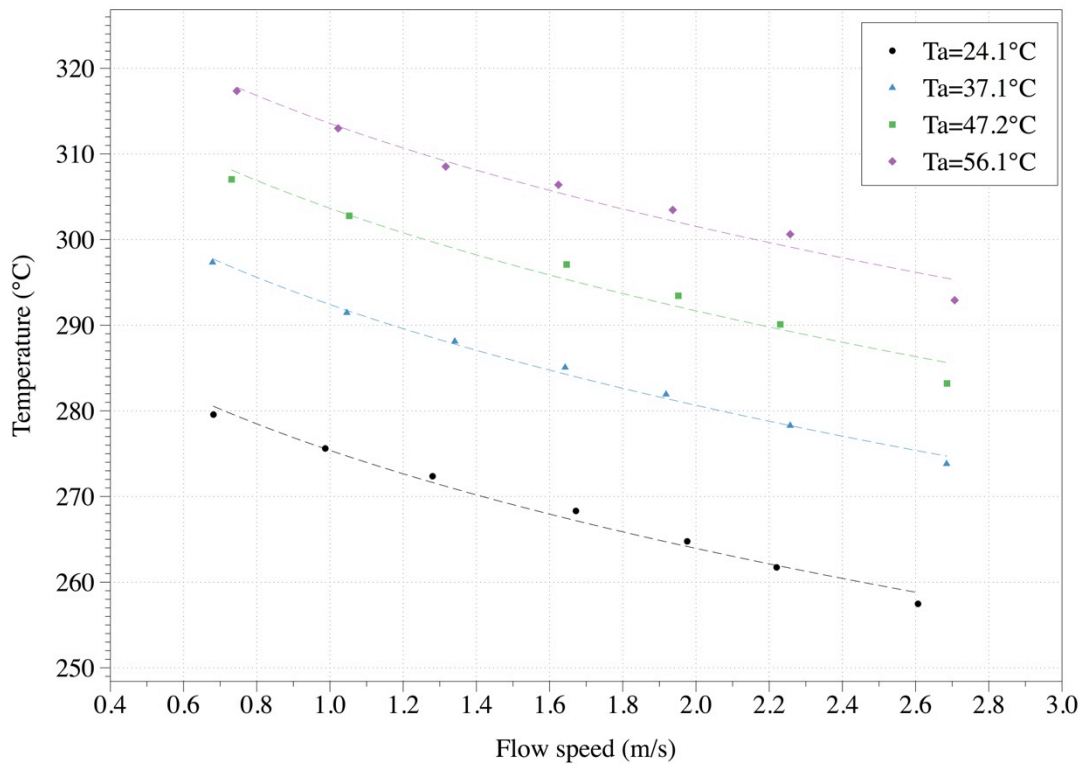


Figure 3.25. Response of sensors at different ambient temperature. The absorbed power was 720 mW

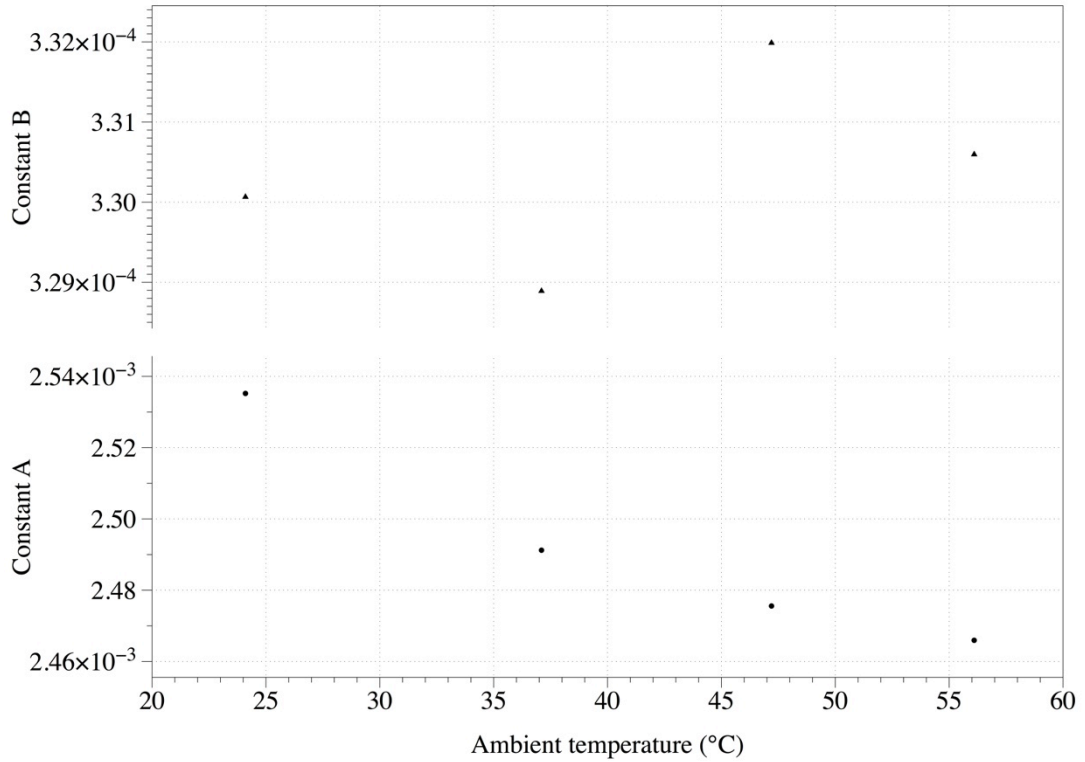


Figure 3.26. Change in constant A and B at different ambient temperature

Figure 3.23 shows the sensor's response to water flow at different flow speed and Figure 3.24 shows change in constant A and constant B when equation (3.1) is used to fit the results at different absorbed power level. In the figure, the temperature change induced by the speed of water flow change is much smaller than in air. Despite equation (3.47) and (3.48) give the flow sensitivity of the bare high absorption fibre in air, they can still give the idea that increase in thermal conductivity of the flowing fluid or increase in the outer diameter of the sensor setup will cause the flow sensitivity to decrease. In the case of the water flow experiment, the outer diameter is larger than that in the air flow experiments and the thermal conductivity of water is much higher than air. So, the sensitivity of the sensor in water flow is expected to be lower. Figure 3.25 shows the sensor's response at different ambient temperature  $T_a$  (i.e. water temperature). Figure 3.26 shows the

variation in constants A and B at different ambient temperature. The constant A decreases when the ambient temperature increases but the magnitude is very small. Changing the temperature by 20 °C causes the decrease in constant A by about 2.5%. Constant B shows no clear relationship with the changing ambient temperature. These experiments show the sensor response at different ambient temperatures are nearly the same, except a “DC offset” by the ambient temperature in the sensor’s measured temperature.

### **3.6 Conclusions**

The possibilities of using pure optical fibre for flow measurement was studied. High absorption fibre was used as the sensing fibre. Due to the high attenuation of this kind of fibre, high level of power was absorbed. The absorbed optical energy was converted into thermal energy. The flowing fluid brings the energy away by forced convection. This causes change in temperature of the high absorption fibre and this temperature change was measured by an FBG inscribed in the fibre.

The effectiveness of the high absorption fibre flow sensor was first evaluated against air flow. After that, equations were developed and it has been shown that they match well with the experimental results previously obtained. Using the equations developed, the efficiency of optical to thermal energy conversion was found to be close to 100%. These equations can help to estimate the sensor response and sensitivity in future design of new fibre optic thermal anemometer.

The possibility of using this fibre sensor for liquid flow measurement was studied. The high absorption fibre was protected by a tiny glass tube to avoid the FBG from measuring the stress caused by the water flow. The sensitivity of the sensor was found to be much lower when compared to air flow. This could be due to the larger

outer diameter caused by the addition of a glass protection tube and the higher thermal conductivity of water than air.

The response of sensor at different ambient temperature was evaluated. As we did not have equipment to adjust the flowing air temperature, the sensor was tested in the water flow setup. The results suggest the response of the sensor at different ambient temperature are similar except a “DC offset” by the ambient temperature.

## Chapter 4

# Reducing power/temperature dependency and multiplexing of the fibre optic thermal anemometer

### 4.1 Introduction

In the previous chapter, a pure fibre optic thermal anemometer was described. The sensor composed of a 5 mm section of high absorption fibre with an FBG inscribed in it. The FBG measured the temperature fluctuation of the high absorption fibre and the temperature information can be converted into the corresponding flow speed. The response of the sensor against ambient temperature change was also studied. The results showed the temperature of the sensor was only offset by the amount of temperature changed. Which means  $\Delta T$ , which is  $T - T_a$ , is nearly constant. To mitigate the effect of the temperature change, an extra FBG would be needed to measure to ambient temperature change. Another method to measure ambient temperature is by switching off the pumping light source. This turns the high absorption fibre based thermal anemometer into a normal FBG for temperature measurement. The measured temperature is affected by not only the ambient temperature fluctuation, but also the fluctuation in pumping. One way to reduce the fluctuation in the measured results is to finely control the output power of the pump laser.

Another issue of the high absorption fibre based thermal anemometer is serial multiplexing. Due to the high absorption of the fibre over a wide band of wavelength, serially multiplex more sensors would not be feasible.

In this chapter methods to tackle the above-mentioned problems will be described. To reduce the pump power and ambient temperature dependency of the high absorption fibre based thermal anemometer, a pulsed operation is used. Instead of measuring directly the temperature of the sensor as in the constant power operation described in the last chapter, the time constant of the falling temperature when the pump power is switched off from the sensor is used. Simulation and experiment results prove the effectiveness of the scheme in reducing the power and temperature dependency. To enable serial multiplexing of more sensors, the reflection wavelength of the FBG is moved from 1500-1600 nm to 800-900 nm, where the attenuation is shown to be much smaller than attenuation around 1500-1600 nm.

## **4.2 Equations for pulse operation**

In previous chapter, the high absorption fibre based thermal anemometer described was powered by a pump laser with constant and continuous optical output. The temperature of the high absorption fibre was shown to be affected by the ambient temperature. The response of the sensor was also mathematically and experimentally shown to be dependent on the absorbed power. These results suggested that for the sensor system to give accurate measurement result, monitoring the fluctuation of ambient temperature and pump laser output power is essential.

To reduce the ambient temperature and pump power dependency, pulse operation can be used. In pulse operation, instead of a constant supply of optical power, the optical output of the pump laser is modulated on and off. This can be achieved by modulating the supply current of the pump laser or by the use of an optical switch to modulate the optical output of the pump laser.

The transient response of the sensor is to be analyzed. The Biot number is a dimensionless number that indicates the temperature drop within a solid body relative to the temperature difference between the temperature of solid body's surface and the ambient fluid [68]. Equation (4.1) gives the expression for the Biot number for cylindrical coordinate.

$$Bi = \frac{0.5hr}{k} \quad (4.1)$$

$h$  is the convection coefficient,  $r$  is the radius,  $k$  is the thermal conductivity of the body. In case for an optical fibre, the Biot number is  $Bi=0.5hr_{cladd}/k_{fibre}$ , where  $r_{cladd}$  is the cladding radius and  $k_{fibre}$  is the thermal conductivity of the fibre.

To estimate the transient response of the sensor, lumped capacitance method is used. To yield acceptable results, the temperature gradient in the solid body has to be relatively small when compared to the difference between body's surface temperature and the fluid. So, for the lumped capacitance method to be valid, the Biot number  $Bi$  should be less than 0.1.

In a control volume, the rate of energy stored is equal to the rate of energy generated in the volume plus the rate of energy input to the system minus the rate of energy leaving the volume. This gives

$$\frac{dE_{st}}{dt} = \frac{dE_{in}}{dt} + \frac{dE_g}{dt} - \frac{dE_{out}}{dt} \quad (4.2)$$

$E_{st}$  is the energy stored,  $E_{in}$  is the energy input,  $E_g$  is the energy generation and  $E_{out}$  is the energy that leaves the system. In the pulse operation of the high absorption fibre, the falling temperature of the fibre when the pump laser output is cut off by the

optical switch is measured, so no energy generation in and energy input to the fibre.

Equation (4.2) is modified to

$$\rho V c \frac{dT}{dt} = -hA(T - T_a), \quad (4.3)$$

where  $\rho$ ,  $V$ , and  $c$  are the density, volume and specific heat capacity of the high absorption fibre,  $A$  is the surface area of the high absorption fibre and  $T_a$  is the ambient temperature of the fluid. Integrate equation (4.3) gives

$$\frac{\rho V c}{hA} \int_{T_i}^T \frac{1}{T - T_a} dT = - \int_0^t dt$$

$$\frac{T - T_a}{T_i - T_a} = \exp\left(-\frac{hA}{\rho V c} t\right). \quad (4.4)$$

According to equation (4.4), the temperature of the high absorption fibre drops exponentially and the thermal time constant of the temperature drop is

$$\tau_t = \frac{\rho V c}{hA}. \quad (4.5)$$

Equation (4.5) indicates that the decay of the temperature of the high absorption fibre is a function of the convection coefficient  $h$ , density  $\rho$ , volume  $V$  and specific heat capacity  $c$  of the fibre. The convection coefficient  $h$  is related to the flow speed  $v$  by equation (3.39) given in the previous chapter.

Table 4.1. Physical properties of air and optical fibre

<b>Fluid – Air at Room Temperature</b>	
Density $\rho$ (kg/m <sup>3</sup> )	1.184
Kinematic Viscosity $\nu$ (m <sup>2</sup> /s)	$1.589 \times 10^{-5}$
Prandtl Number $Pr$	0.707
Thermal Conductivity $k$ (W/m/K)	0.0236
<b>Optical Fibre (Silica)</b>	
Density $\rho$ (kg/m <sup>3</sup> )	2220
Specific Heat Capacity $c$ (J/kg·K)	745
Thermal Conductivity of Fused Silica at Room Temperature $k$ (W/m/K)	1.38
Core Radius (Single Mode) $r_{core}$ (m)	$4.15 \times 10^{-6}$
Cladding Radius $r_{cladd}$ (m)	$62.5 \times 10^{-6}$

Table 4.2. Biot number of the sensor at different flow speed. The values are calculated by equation (4.1) and values in table 4.1.

Flow Speed (m/s)	Biot Number
1	0.0079
2	0.0106
3	0.0127
4	0.0144
5	0.0160

Table 4.1 gives the physical and thermal properties of air and silica at room temperature and pressure for the theoretical calculation. Table 4.2 shows the Biot number of the high absorption fibre at different flow speed. The numbers were

calculated by values given in table 4.1. At flow speed of 5 m/s, the Biot number is 0.016, which is far below 0.1. This indicates the lumped capacitance method is valid.

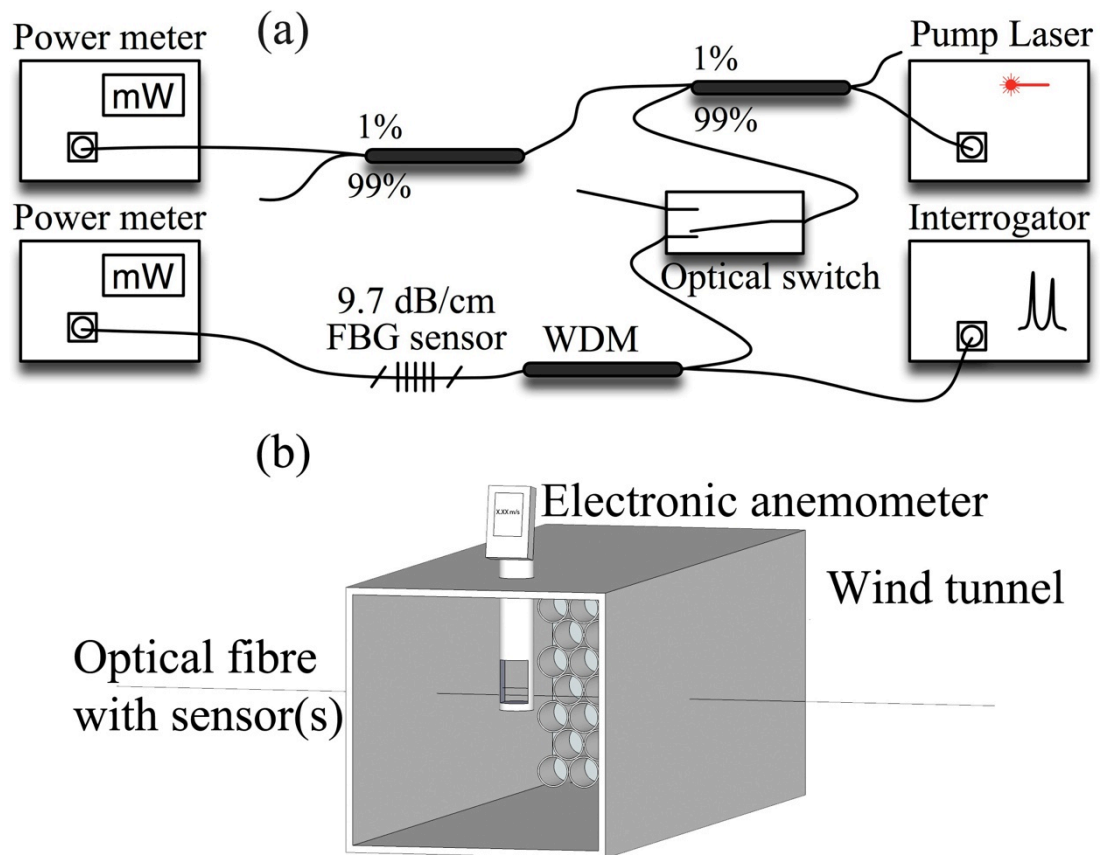


Figure 4.1. (a) Optical setup of the experiment. (b) Wind tunnel experimental setup.

Figure 4.1a shows the optical connection of the high absorption fibre. The core diameter of the fibre is  $8.7 \mu\text{m}$ , cladding diameter is  $125 \mu\text{m}$ . The attenuation of the fibre used is  $9.7 \text{ dB/cm}$  at  $1550 \text{ nm}$ . In the experiment,  $5 \text{ mm}$  section of the high absorption fibre was used. An FBG was inscribed throughout the whole length of the fibre. Both ends of the high absorption fibre were connected to corning SMF28 standard single mode fibre. The pump laser used was an IPG Laser GmbH PYL-2-1455-R. The output wavelength is  $1455 \text{ nm}$  and the measured maximum output power was  $1.2 \text{ W}$ . About  $0.01\%$  of the laser output power was fed into an ILX Lightwave FPM-8200H power meter to monitor the output power level of the pump

laser. 99% of the laser output enter an Agiltron Incorporated LBHP-120121111 high power optical switch at where the laser light is modulated on and off. The optical switch was controlled by a self made controller board. The modulated laser light then enter a wavelength division multiplexor (WDM) which combine the modulated pumping laser light and the output from the interrogator. The pump laser and the probing light from the interrogator enter the high absorption fibre. The FBG reflects certain wavelength back through the WDM to the interrogator. The remaining light after the high absorption fibre is measured by an ILX Lightwave FPM-8210 power meter.

Figure 4.1b shows the setup to measure air flow speed. A wind tunnel was built to reduce the turbulence. A commercial DC fan was used. The 5 mm section high absorption fibre thermal anemometer was placed in the centre of the wind tunnel. A Testo 405-V1 electrical hot-wire anemometer was placed behind the high absorption fibre thermal anemometer for flow speed reference. The measured flow speed was between 1 m/s and 5 m/s.

### 4.3 Simulation and experimental results

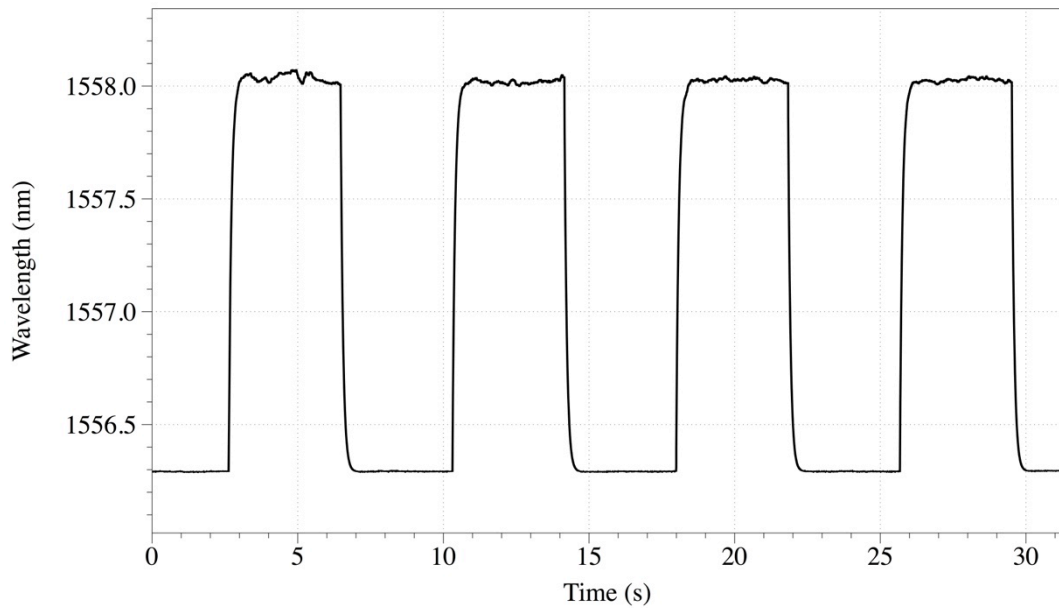


Figure 4.2. Pulsation of sensor's wavelength when the optical switch is open for about 3.8 s, a time long enough to allow the high absorption fibre to reach steady state.

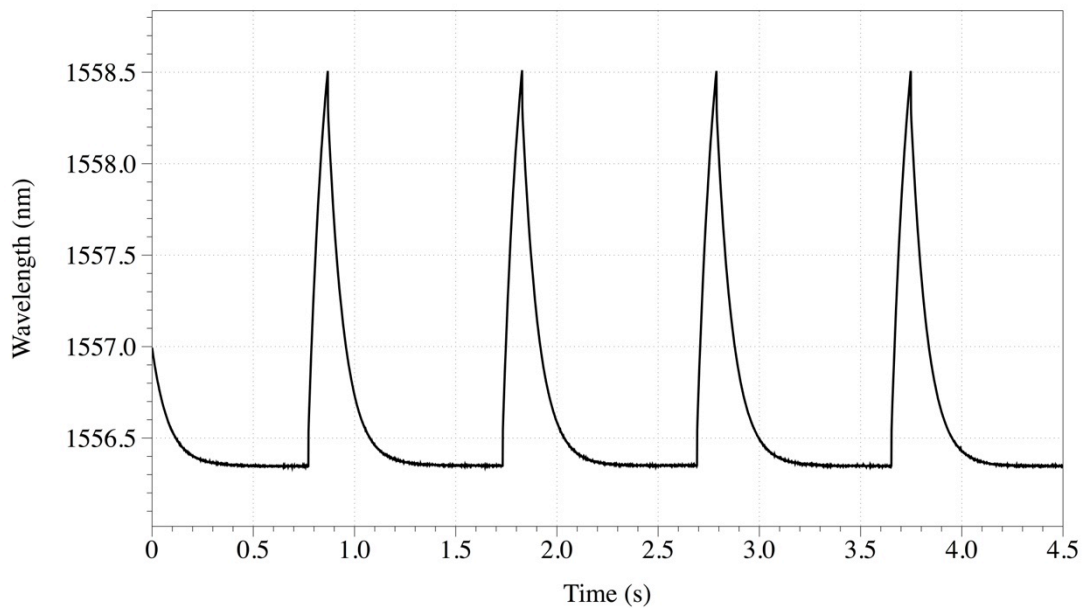


Figure 4.3. Pulsation of sensor's wavelength when the open time of the optical switch is about 95 ms, which is short compared to the open time described in Figure 4.2 and the high absorption fibre cannot reach steady state

Figure 4.2 and 4.3 depict the wavelength change of the FBG inscribed in the high absorption fibre when the optical switch is modulating the pump laser light on and off. Figure 4.2 shows the pulsating wavelength change of the FBG when the on-time

of the optical switch is long enough to allow the temperature of the high absorption fibre to reach steady state. The switch cut off the pump laser output to let the high absorption fibre cools. Figure 4.3 gives the pulsating wavelength change of the FBG when the on-time of the optical switch is shorter then enough for the high absorption fibre to reach the steady state before the optical switch cut the pump laser light. The on-time of the switch is about 95 ms.

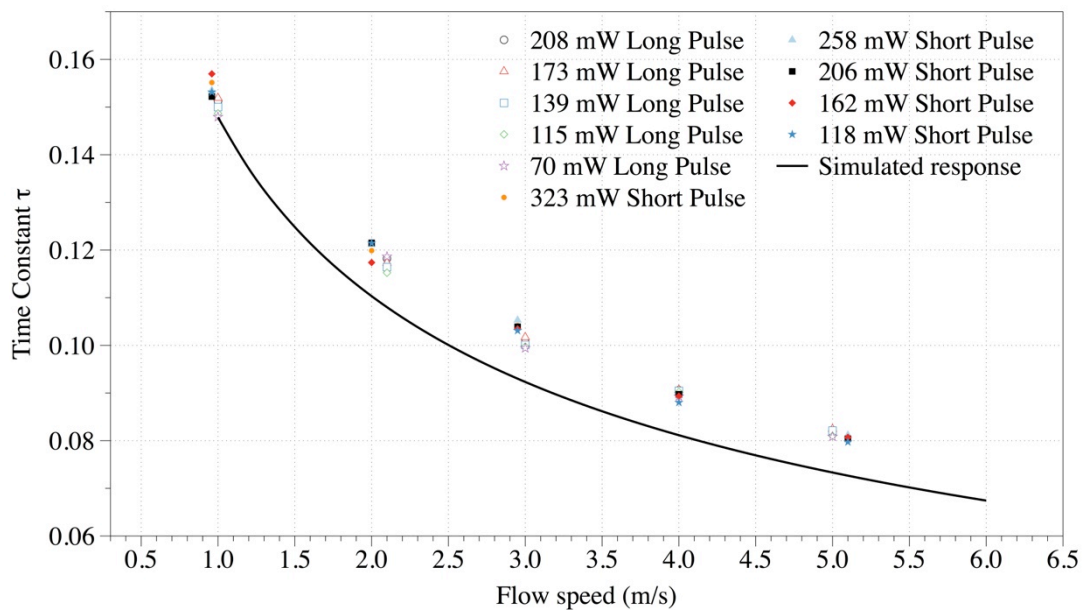


Figure 4.4. Experimental and simulated response of the falling edge time constant when the sensor's temperature is allowed to reach steady state (long pulse) and too short to reach steady state (short pulse)

Figure 4.4 shows the effect of allowing the sensor's temperature to reach steady state (long pulse) or unable to reach steady state (short pulse) at different absorbed power levels. According to the figure, for the long and short on pulses and for different absorbed power levels, the results shows no distinctive trend in drifting in any particular direction. There is only one simulated response as equation (4.5) is independent of absorbed power level. The simulated response match well with the experimental results, which shows the validity of equation (4.5).

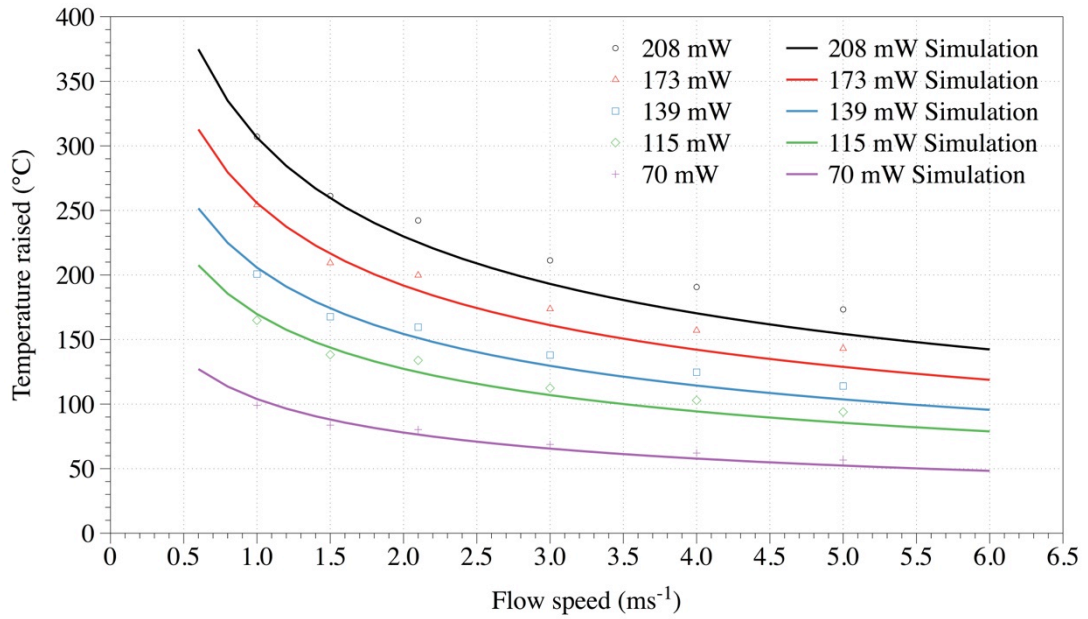


Figure 4.5. Experimental and simulation results of the high absorption thermal anemometer in constant power operation

Figure 4.5 shows the experimental and simulation results of the high absorption thermal anemometer when it is in constant power operation. When compare this with Figure 4.4 where the sensor was in pulse operation, there is a significant trend of drift as the absorbed power increases. These results suggested that the pulse operation can significantly reduce the dependency of the sensor on the level of absorbed power. As equation (4.5) was shown to be valid for the high absorption fibre thermal anemometer, ambient temperature change should not yield significant effect on the measured time constant  $\tau$ .

#### 4.4 Serial multiplexing

The attenuation of the high absorption fibre is high near 1550 nm. The attenuation of the fibre used ranges from 3 dB/cm to 9.7 dB/cm. High attenuation results in difficulty in serial multiplexing of the sensors as the light from the interrogator will experience high attenuation in the round trip, especially if the sensor is placed at the last. One solution to the issue is to move the centre wavelength of the FBG to 800-

900 nm. A self designed interrogator operating in the range 800-900 nm was used to read the sensor. The attenuation of the high absorption fibre used are 3 dB/cm, 7 dB/cm and 9.7 dB/cm. Their attenuation at 850 nm were measured to be 0.07 dB/cm, 0.22 dB/cm and 0.24 dB/cm respectively, which are much smaller than the attenuation at 1550 nm. The low attenuation around 850 nm makes multiplexing several sensors possible.

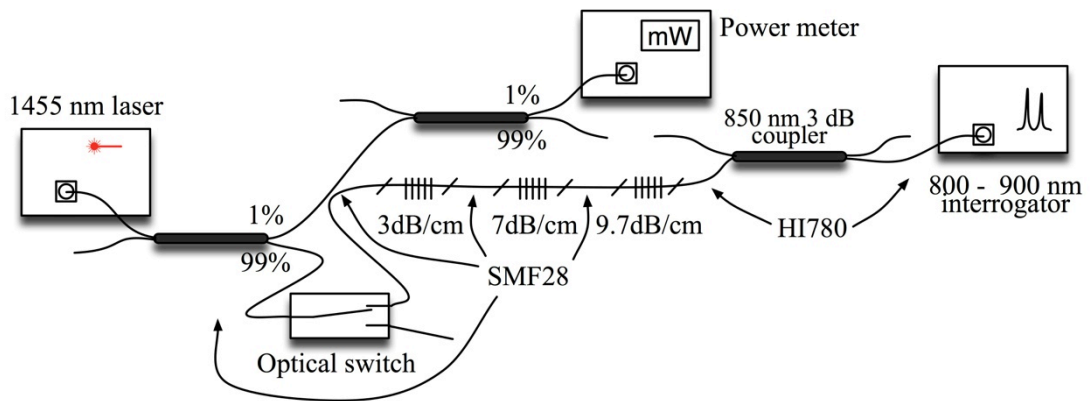


Figure 4.6. Experimental optical connection of the serially multiplexed sensor working in around 850 nm

Figure 4.6 shows the experimental optical connection for the 850 nm serially multiplexing of three high absorption fibre thermal anemometers. The output power of the pump laser was 600 mW. About 0.01% of the laser output was directed to an ILX FPM-8210H optical power meter to monitor the output power of the pump laser. The remaining 99% then pass through an optical switch, which was controlled by a self-built controller board. The modulated pulsating light then enter an array of high absorption fibre. The 3 dB/cm high absorption fibre was placed closest to the optical switch, followed by the 7 dB/cm high absorption fibre. The 9 dB/cm high absorption fibre was the furthest away from the optical switch. The reflection wavelength of the FBGs in these high absorption fibre were 837.9 nm, 847.5 nm and 851.8 nm respectively. Their absorbed optical power were 173 mW, 233 mW and 126 mW

respectively. After the array of sensor was a 3 dB coupler at 850 nm. The coupler was based on HI-780 optical fibre and the insertion loss at 1455nm at one of the ports was very high, which makes it function like a WDM. An interrogator function in the range of 800-900 nm was connected to this 3 dB coupler's port where the insertion loss at 1455 nm is high. The 847.5 nm and 851.8 nm (7 dB/cm and 9.7 dB/cm high absorption fibre) thermal anemometers were put inside the wind tunnel to test the flow response. The 837.9 nm sensor (3 dB/cm high absorption fibre) was kept outside the wind tunnel. Figure 4.7 shows the spectrum of the three serially connected FBGs. The lower amplitude of the 837.9 nm peak is due to weaker inscribed FBG.

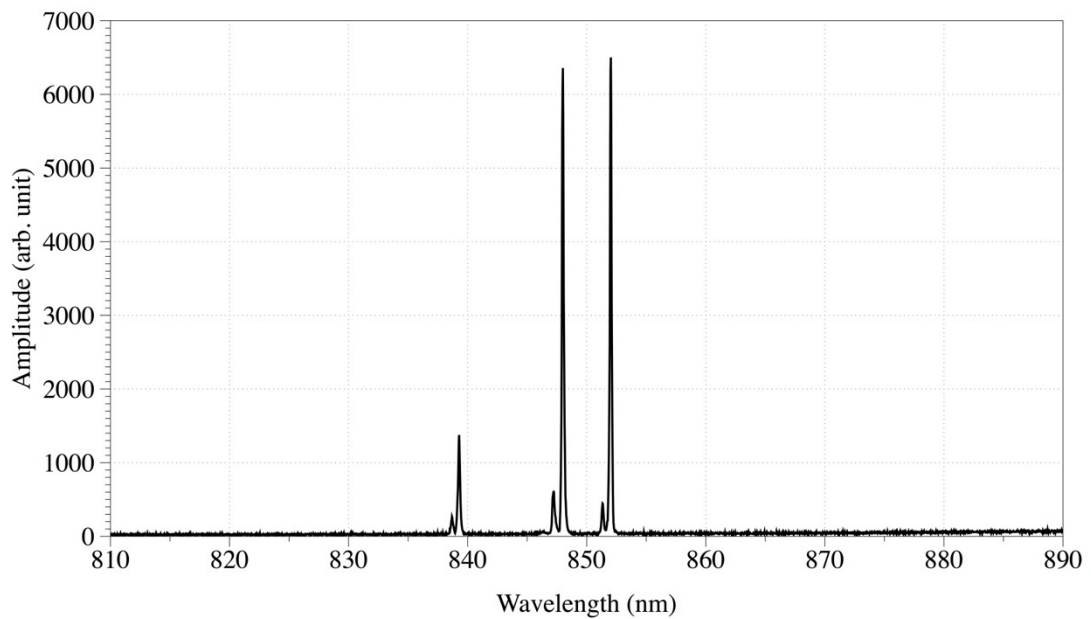


Figure 4.7. Reflection spectrum of the sensor array

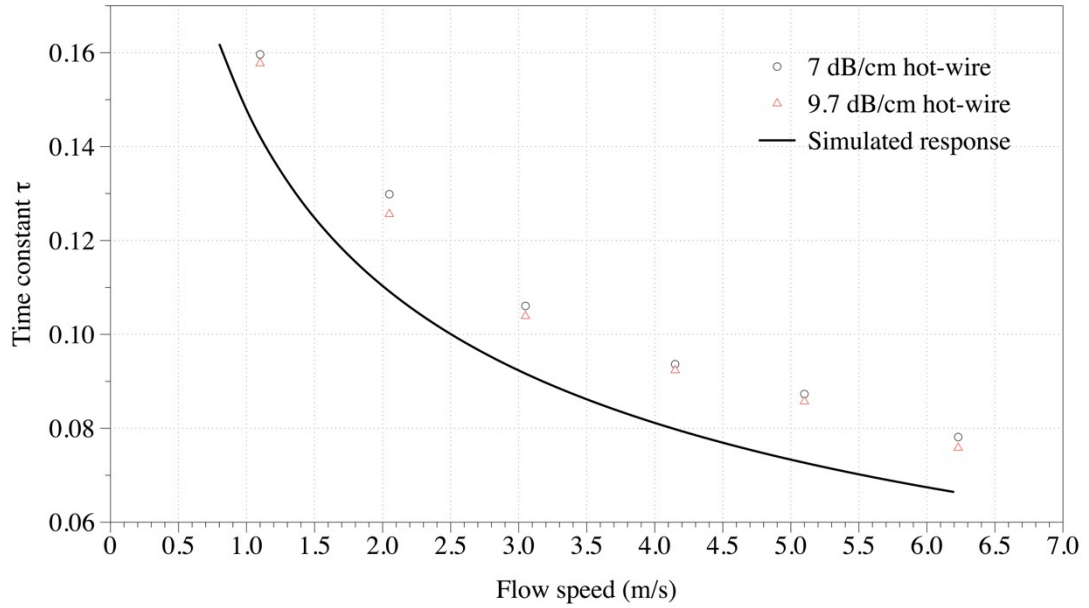


Figure 4.8. Experimental results of the multiplexed sensor in pulse operation

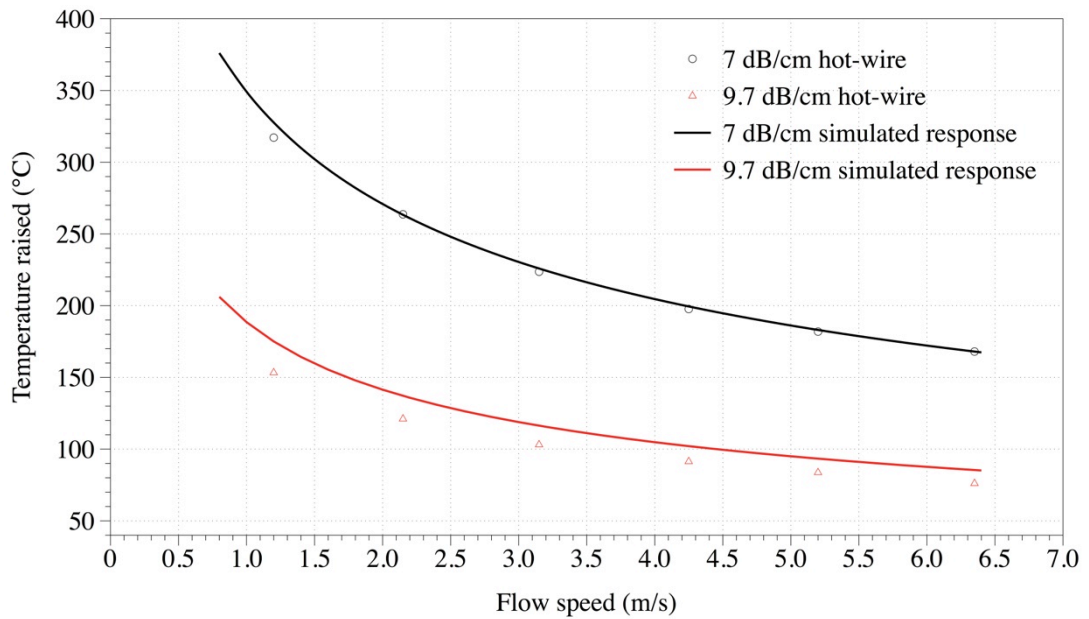


Figure 4.9. Experimental results of the multiplexed sensor in constant power operation

Figure 4.8 shows the experimental results in pulse operation. The time constants of the two sensors measured are similar to each other. Figure 4.9 shows the results when the sensors were in constant power mode. It can be shown that in constant power operation, the differences in readings of the two sensors at the same flow speed are higher than pulse operation. In the wind tunnel setup, there are several

sources of error. As the wind tunnel was not professionally built, the flow in it could still have some turbulence. The flow speed at different location might be slightly different. Every time, the sensors are not placed exactly at the same position. In multiplexing work, the two sensors were placed one in front of the other. This might also affect the flow of air, which could cause error.

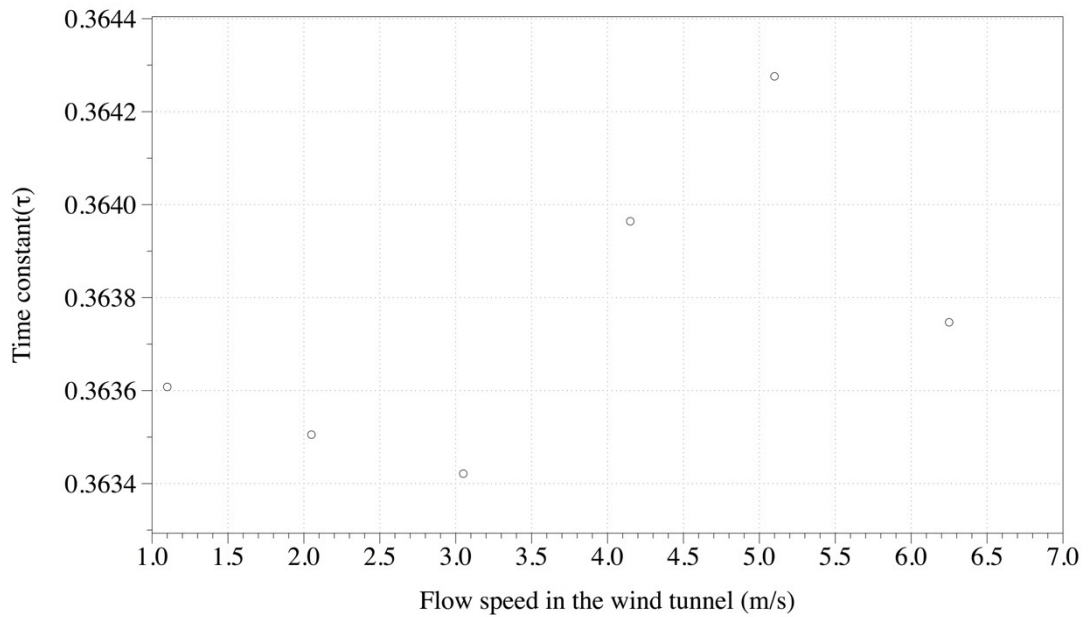


Figure 4.10. Fluctuation in time constant of the 837.9 nm (3 dB/cm high absorption fibre) sensor

To demonstrate the time constant of the sensor array is dependent only on flow speed, the FBG sensor at 837.9 nm was placed outside of the wind tunnel. Figure 4.10 shows the fluctuation in time constant of the 837.9 nm sensor when the flow speed of air in the wind tunnel was varying. The fluctuation of the time constant is less than 1% and display no clear relationship to the flow inside the wind tunnel.

Figure 4.11 gives the reflection spectrum of the FBGs after the experiment. The reflectivity of the sensor drops only a little bit.

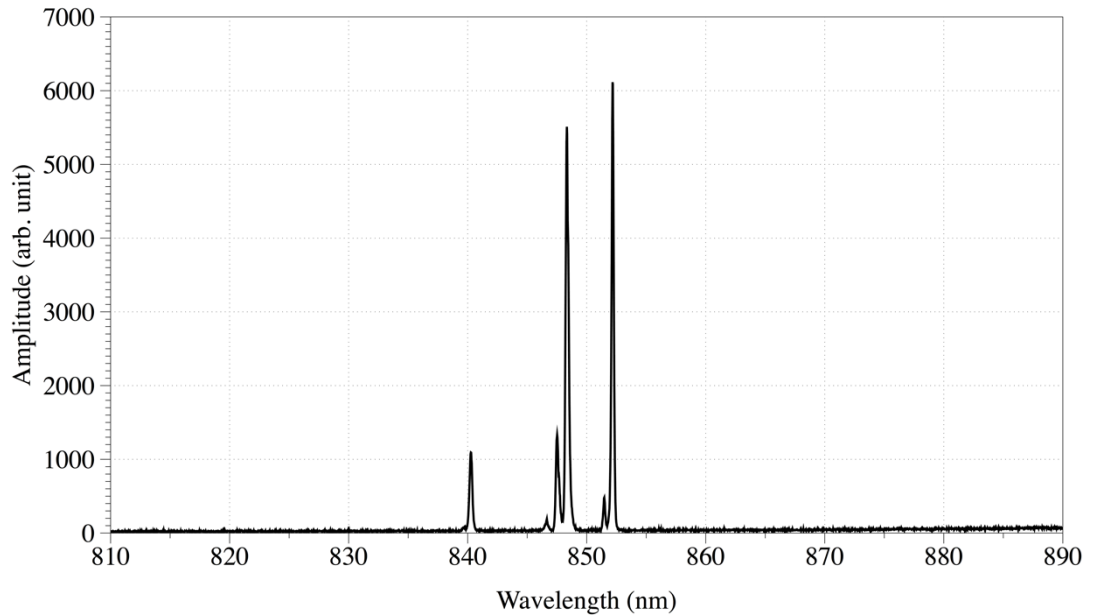


Figure 4.11. Reflection spectrum of the FBGs after the experiment

## 4.5 Conclusions

To reduce the power and temperature dependency of this pure fibre optic thermal anemometer, pulse operation was demonstrated. This method measures the time constant of the falling temperature's curve when the pump laser power is cut off. The results were as expected to be much less power dependent than constant power operation. Pulse operation can also prolong the life of the sensor as the sensor is not kept at elevated temperature all the time. Multiplexing of three sensors were demonstrated. Using FBGs with reflected wavelength in the range of 800-900 nm avoids the high attenuation around 1550 nm. Pulse operation help keep different sensors to have similar response and less power and temperature dependency.

## **Chapter 5**

# **High sensitivity and low cost Sagnac loop based pressure sensor**

### **5.1 Introduction**

In the previous chapter, a flow sensor design based on fibre Bragg grating (FBG) was demonstrated. The reflected wavelength of the FBG shifts when the temperature of the sensor changes. In this chapter, a pressure sensor design based on Sagnac interferometer is demonstrated. Sagnac interferometer is an effective sensor configuration [69]. The two counter propagating beams interfere with each other and cause an interference pattern [47]. The birefringence of a polarization maintaining fibre (PMF) is sensitive to pressure applied on it [56-57]. This suggests that PMF can be a candidate for Sagnac loop based pressure sensor. However, at the same time, it is also a good candidate for temperature measurement [58]. The temperature sensitivity of PMF is caused by the difference in thermal coefficient between the silica cladding and the boron-doped stress applying parts [58], which makes it a good temperature sensor. Polarization maintaining photonic crystal fibre (PM-PCF) has a pure silica structure and hence has much lower birefringence-temperature sensitivity [70-72].

The shift of a Sagnac interferometer's transmission spectrum has been used to measure pressure change [62-63]. The operation wavelength of these reported sensors were all around 1550 nm and 1300 nm and measurements were carried out using optical Spectrum Analyzer (OSA). One problem of measuring with an OSA is

the slow scanning rate and the high cost. Another alternative is to use optical fibre interrogator based on tunable laser. These interrogators are very expensive too and the scanning rates are not high if the full spectrum is read and analyzed.

An idea of moving the operation wavelength from 1550 nm to the range 800-900 nm is to be introduced. The benefits of operation in the range of 800-900 nm is that CCD based optical fibre interrogator can be used. The benefits of CCD based optical fibre interrogator is the high full spectrum read out rate and the lower cost when compare to the 1550 nm optical fibre interrogator. The moving from longer wavelength to the shorter wavelength also yield nearly three times increase in pressure sensitivity.

In other reported works [62-63], spectral shift of the Sagnac loop were measured. One of the maximum of the sensor's interference pattern was measured. If this maximum shifts beyond the spectrum range, a new maximum has to be used. The new maximum shows different sensitivity than the previous one. Thus, this limits the measuring range of the sensor system. The range limitation can be solved if the phase of the sinusoidal waveform like spectrum is measured instead of the actual wavelength shift. Experiments show both spectral shift and phase shift method give similar accuracy but the measuring range of the phase shift method is not limited by the spectral width of the optical light source and the optical fibre interrogator's measuring spectral width.

## 5.2 Principle

The transmission spectrum of a Sagnac interferometer is [62]

$$T = \frac{1}{2} [1 - \cos(\delta_0 + \delta_1)], \quad (5.1)$$

where  $\delta_0$  and  $\delta_1$  are given by

$$\delta_0 = \frac{2\pi B_0 L}{\lambda}, \quad (5.2)$$

$$\delta_1 = \frac{2\pi (K_p \Delta P) L}{\lambda}. \quad (5.3)$$

The pressure value used below are all relative values, so  $B_0$  is the birefringence of the PM-PCF at the initial pressure value.  $\Delta P$  is the applied pressure, and can be replaced by  $P$  as it is a relative pressure.  $L$  is the length of the PM-PCF used in the Sagnac loop.  $K_p$ , which is the birefringence-pressure coefficient, can be expressed as [9]

$$K_p = \frac{\partial B}{\partial P} = \frac{\partial n_s}{\partial P} - \frac{\partial n_f}{\partial P}, \quad (5.4)$$

where  $n_s$  is the refractive index of the slow axis and  $n_f$  is the refractive index of the fast axis.

The pressure induced path length change is very small and negligible [60]. So, the total phase difference can be expressed as

$$\delta = \delta_0 + \delta_1 = \frac{2\pi L}{\lambda} (B_0 + K_p P) \quad (5.5)$$

$K_p$  changes linearly with pressure, so equation (5.5) can be expressed as

$$\delta = \frac{2\pi L}{\lambda} \left( B_0 + \frac{\Delta B}{\Delta P} P \right), \quad (5.6)$$

where  $\Delta B/\Delta P$  is the linear relationship between the birefringence and pressure. The transmission spectrum equation (4.1) can now be expressed as

$$T = \frac{1}{2} \left\{ 1 - \cos \left[ \frac{2\pi L}{\lambda} \left( B_0 + \frac{\Delta B}{\Delta P} P \right) \right] \right\}. \quad (5.7)$$

In equation (5.7), the only varying term is  $(2\pi L/\lambda)(\Delta B/\Delta P)P$ . Equating this term to  $2\pi$  tells the amount of pressure change when there is a period change of the phase of the transmission spectrum's sinusoidal like waveform transmission spectrum.

$$\frac{2\pi L}{\lambda} \cdot \frac{\Delta B}{\Delta P} \cdot P_0 = 2\pi$$

$$P_0 = \frac{\lambda}{L} \cdot \frac{\Delta B}{\Delta P}. \quad (5.8)$$

$P_0$  is the pressure range that can be represented by a period of the sinusoidal like waveform of the transmission spectrum. The pressure per unit radian is  $P_0/2\pi$ . So, for using phase shift to measure pressure change, the phase of the electronic sinusoidal waveform of the output from the CCD based interrogator is linearly dependent on pressure.

$$\frac{\delta_P}{P} = \frac{2\pi}{P_0} = \frac{2\pi L}{\lambda} \cdot \frac{\Delta B}{\Delta P}. \quad (5.9)$$

In equation (5.9),  $\delta_P/P$  represent the change in phase in radian per unit pressure. This tells that the phase shift sensitivity is independent of the pressure. As this method is not dependent on the absolute wavelength, the bandwidth of the light source is not the limiting factor for the measurement range.

Spectral shift was used in some others' publications [62][63]. To find the sensitivity, the spacing between maxima and minima is first found by [60]

$$S = \frac{\lambda^2}{|G|L}. \quad (5.10)$$

where  $G$  is the group birefringence. According to equation (4.8), a period of sinusoidal like waveform represent a pressure range of  $(\lambda/L)/(\Delta B/\Delta P)$ . So, the pressure sensitivity of the spectral shift method is

$$\frac{\Delta\lambda}{\Delta P} = \frac{S}{P_0} = \frac{\lambda}{|G|} \cdot \frac{\Delta B}{\Delta P}. \quad (5.11)$$

Equation (5.11) shows that the sensor length is not a factor in affecting the spectral shift method's pressure sensitivity. According to [59], the value of group birefringence  $|G|$  of the PM-PCF that was used is  $9 \times 10^{-4}$  at 1550 nm and  $2 \times 10^{-4}$  at 850 nm.  $\Delta B/\Delta P$  are similar at both wavelength and are about  $2.36 \times 10^{-6}$ . The sensitivity improvements by moving from 1550 nm to 850 nm can be shown by

$$\left. \frac{\Delta\lambda}{\Delta P} \right|_{\lambda=850nm} / \left. \frac{\Delta\lambda}{\Delta P} \right|_{\lambda=1550nm} = \frac{850/2}{1550/9} = 2.47. \quad (5.12)$$

Equation (5.12) indicates the expected sensitivity improvement is 2.47 times. However, by tracking the wavelength shift, the pressure measurement is limited to only few MPa. This is because spectral range is limited by the bandwidth of the light source, which is usually few tens of nanometers. An alternative is to apply fast Fourier transform (FFT) to the output spectrum of the CCD based interrogator to obtain the spatial frequency. The spatial frequency is given by

$$f = S^{-1} = \frac{|G|L}{\lambda^2}. \quad (5.13)$$

$f$  is the spatial frequency.

$$\Delta f = \frac{L}{\lambda^2} \frac{\Delta G}{\Delta P} \Delta P. \quad (5.14)$$

Equation (5.14) indicates that the frequency change is linearly dependent on the pressure change. So, we can determine the pressure  $P$  by carrying out FFT on the CCD based interrogator output electronic spectrum waveform. Since the whole sinusoidal like waveform is used for the calculation, the measurement range is not limited by the light source.

### 5.3 Experimental setup

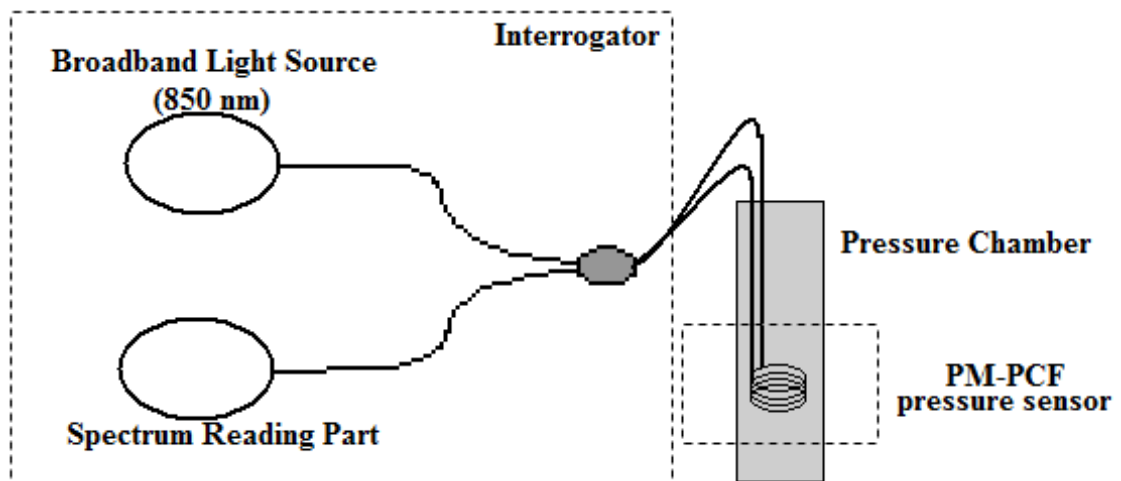


Figure 5.1. Experimental setup of the pressure sensor system

Figure 5.1 shows the experimental setup schematic of the pressure sensor system. A CCD based interrogator was used. Inside the interrogator are a broadband light source, a spectrum reading part and a 3 dB coupler. The two ends of the PM-PCF were both spliced to SMF28 standard single mode fibre. The two ends were then connected to the 3 dB coupler. The PM-PCF used was Blaze Photonics PM-1550-01, which was the same as the one used in [59]. Two sensors were made. The lengths of the PM-PCF of the two sensors were 38 cm and 68.8 cm. The fibres were coiled up to reduce the physical size. The sensors were then put inside an oil pressure chamber.

The light source in the CCD based interrogator is centred at 850 nm. The spectral reading parts is mainly composed of a reflection type diffraction grating and a linear array CCD. The physical resolution is 24 pm/pixel and the maximum scanning rate is 250 Hz. The power consumption of the interrogator is about 1.5 W and can be powered by a single computer USB port. The low power consumption results in high mobility so it can be used for quick outdoor measurement.

## 5.4 Experimental results

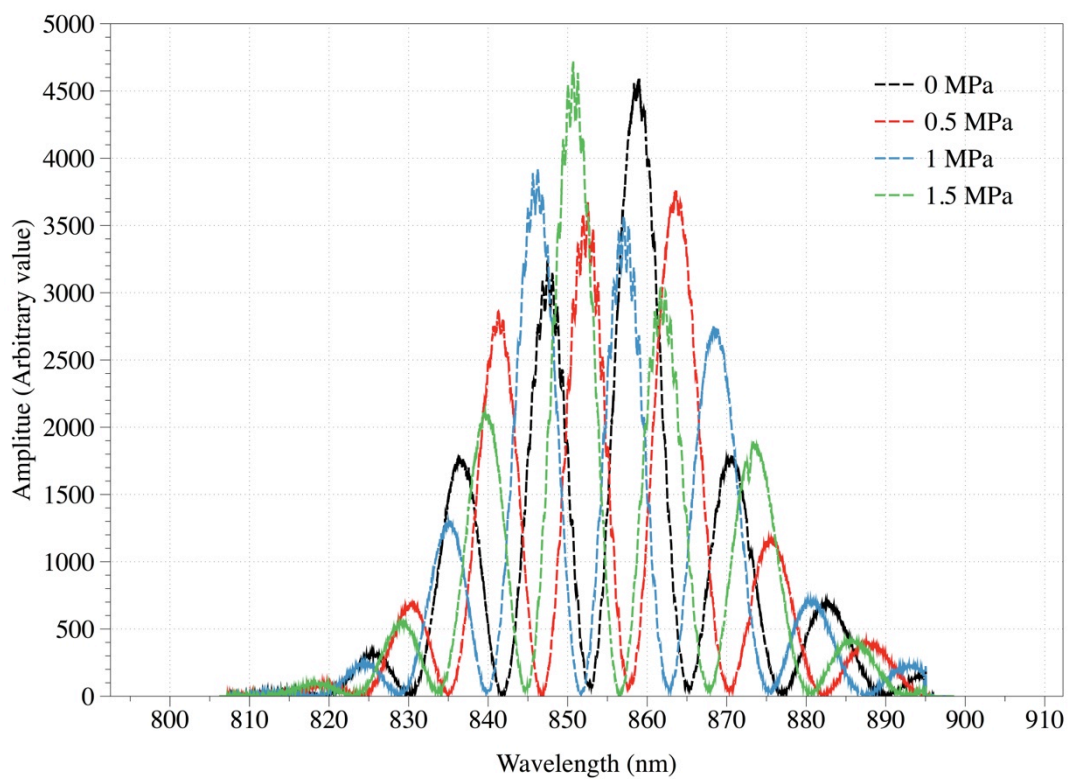


Figure 5.2. Spectrum of the 38 cm long PM-PCF based Sagnac loop at different pressure value

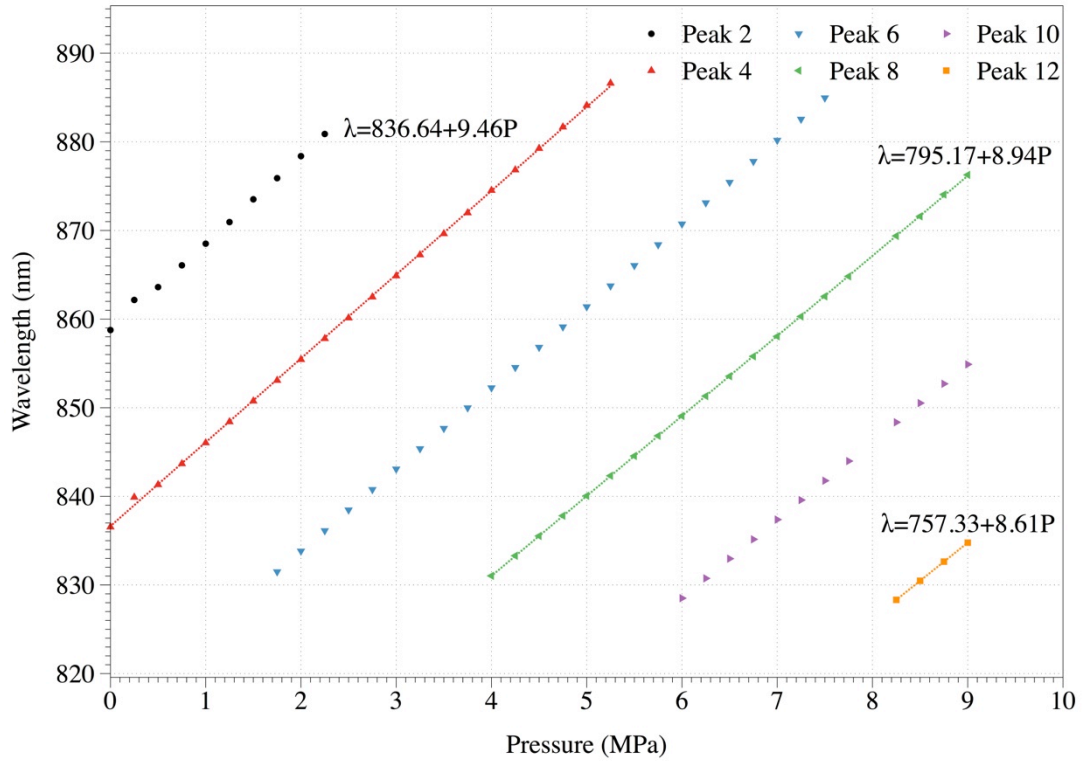


Figure 5.3. Shift of spectral peak against pressure shift of the 38 cm long sensor

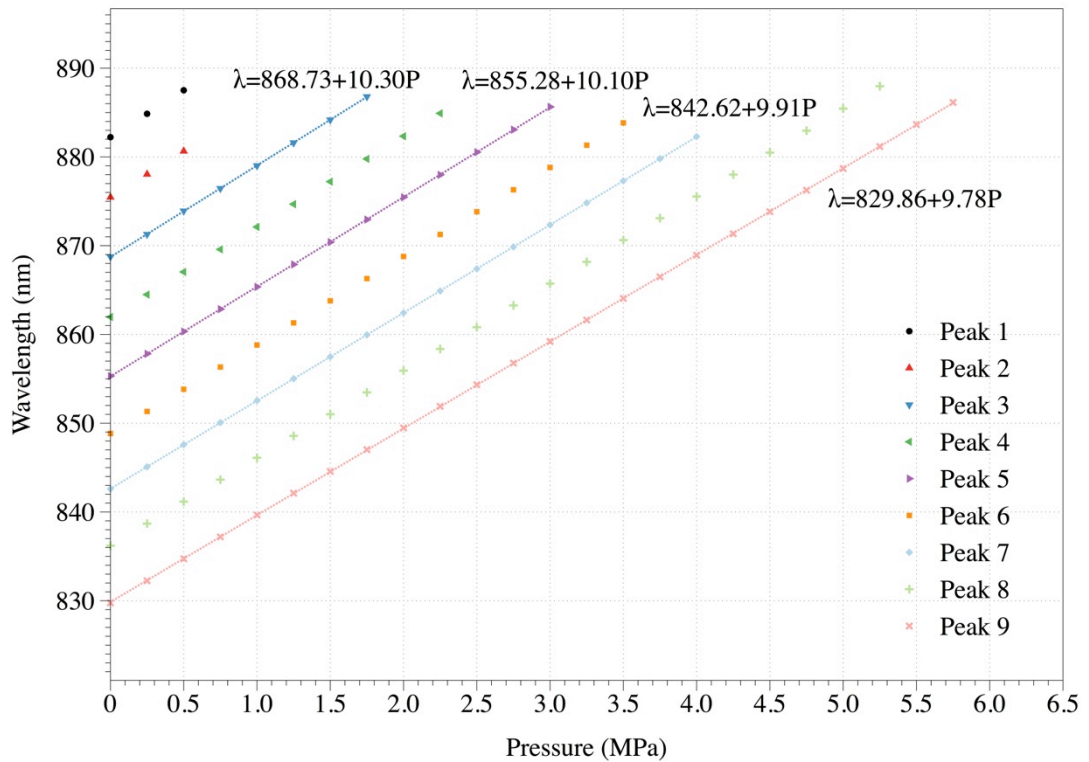


Figure 5.4. Shift of spectral peak against pressure shift of the 68.8 cm long sensor

In the experiments, the sensors were kept inside an oil pressure chamber. The pressure was increased by a step of 0.5 MPa. Figure 5.2 gives the transmission spectrum of the 38 cm sensor from 0 MPa (initial reference pressure) to 1.5 MPa. Figure 5.3 and 5.4 shows the spectral peaks shift against the pressure shift of the 38 cm and 68.8 cm long sensor respectively. The sensitivities of the 38 cm and the 68.8 cm long sensor in the range 0-5 MPa are 9.46 nm/MPa and 9.78 nm/MPa respectively. The sensitivities are similar to each other and so agree with equation (5.11). According to [63], the pressure sensitivity of the same type of fibre in the spectral shift method working around 1550 nm is about 3.42 nm/MPa. This means moving the operation wavelength to around 850 nm give approximately 2.77 times improvement in pressure sensitivity than 1550 nm, which is quite close to the estimation in equation (5.12). Simply moving the wavelength to 850 nm improves the sensitivity by nearly 300%. In Figure 5.3 and 5.4, pressure sensitivity of different peaks are shown. According to the figures, the sensitivity changes when different peaks are monitored. Different peaks are required to be monitored if the pressure range to be measured is very wide. But as all peaks have different sensitivity, the reliability of the sensor is reduced when the pressure varied over a wide range.

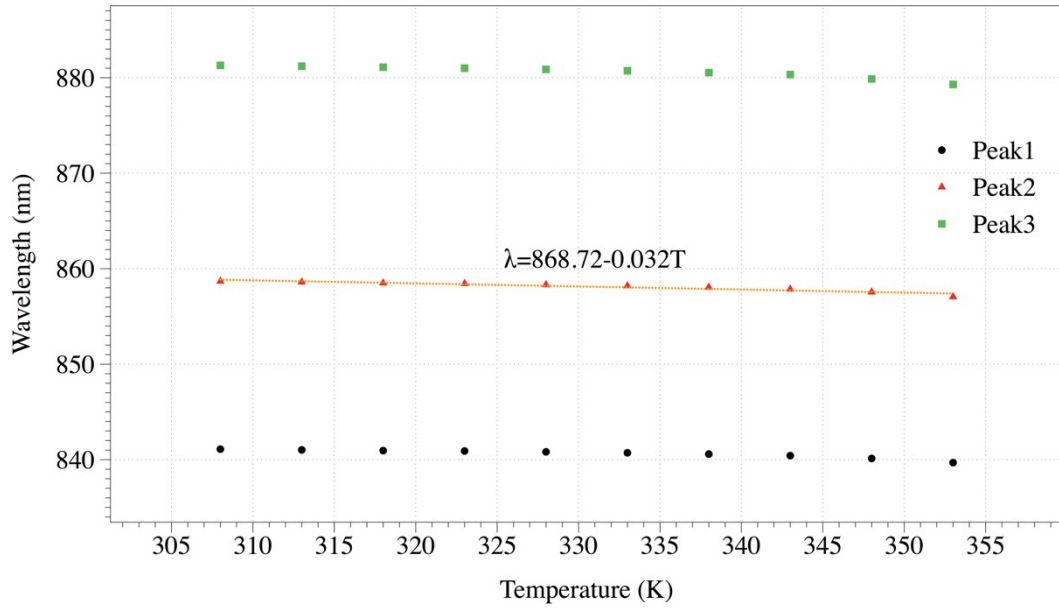


Figure 5.5. Spectral peaks wavelength shift against temperature shift of a 25 cm long PM-PCF sensor

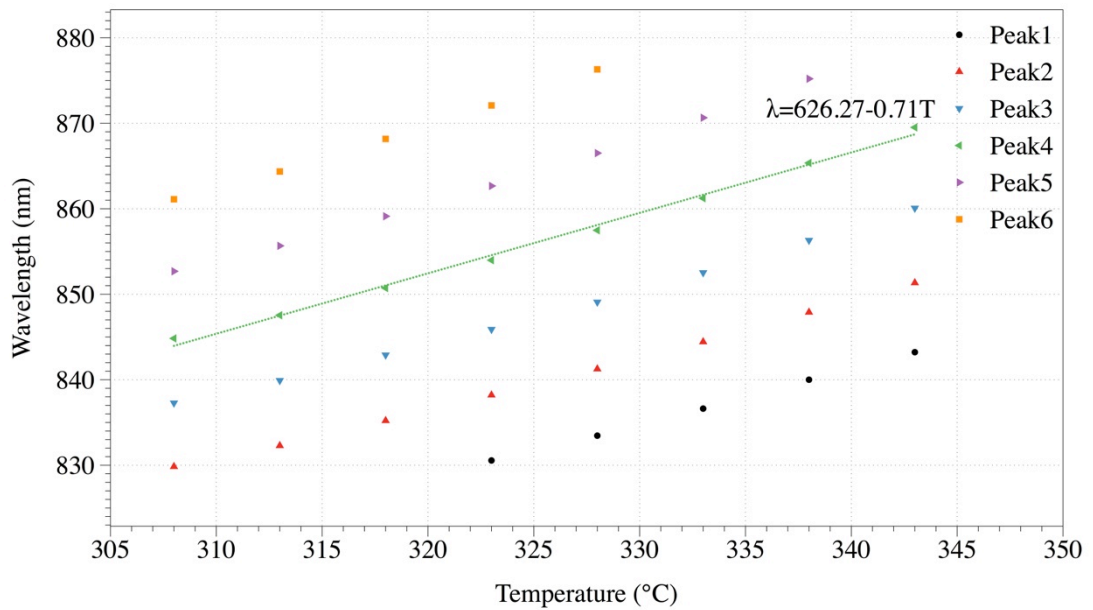


Figure 5.6. Spectral peaks shift against temperature shift of a 21 cm long PM780-HP sensor

The temperature sensitivity of the PM-PCF sensor at 850 nm was also evaluated. Figure 5.5 gives the temperature sensitivity of the PM-PCF Sagnac loop. The temperature sensitivity is about -0.032 nm/K, which is only about 0.34% of the pressure sensitivity. Figure 5.6 shows the spectral peak shift against temperature of a polarization maintaining fibre (PMF) sensor at around 850 nm. The PMF fibre used

was Thorlabs PM780-HP panda PMF. The temperature sensor of this PMF based Sagnac loop is -0.71 nm/K, which is much higher than the PM-PCF based sensor.

To obtain the group birefringence of the PM-PCF section, fast Fourier transform (FFT) is used. FFT converts the spatial domain signal into spatial frequency domain. Obtaining the spatial frequency value can give the group birefringence of the PM-PCF. The number of data points obtained from the CCD is 3840, the data points are treated as a frame of waveform. Directly doing FFT to this array of numbers results in low spatial resolution. Zero padding was used to enhance the spatial resolution. In the experiment, the data sequences obtained were zero padded to 384,000 points. Excluding the low frequencies components around the DC, the frequency with peak amplitude were found. The spatial frequency in the unit  $\text{nm}^{-1}$  can be obtained by

$$f = \frac{f_f}{N \cdot R}, \quad (5.15)$$

where  $f$  is the spatial frequency with unit  $\text{nm}^{-1}$ ,  $f_f$  is the spatial frequency obtained directly after FFT,  $N$  is the number of data points used for FFT,  $R$  is the physical resolution of the CCD in unit  $\text{nm}/\text{pixel}$ .

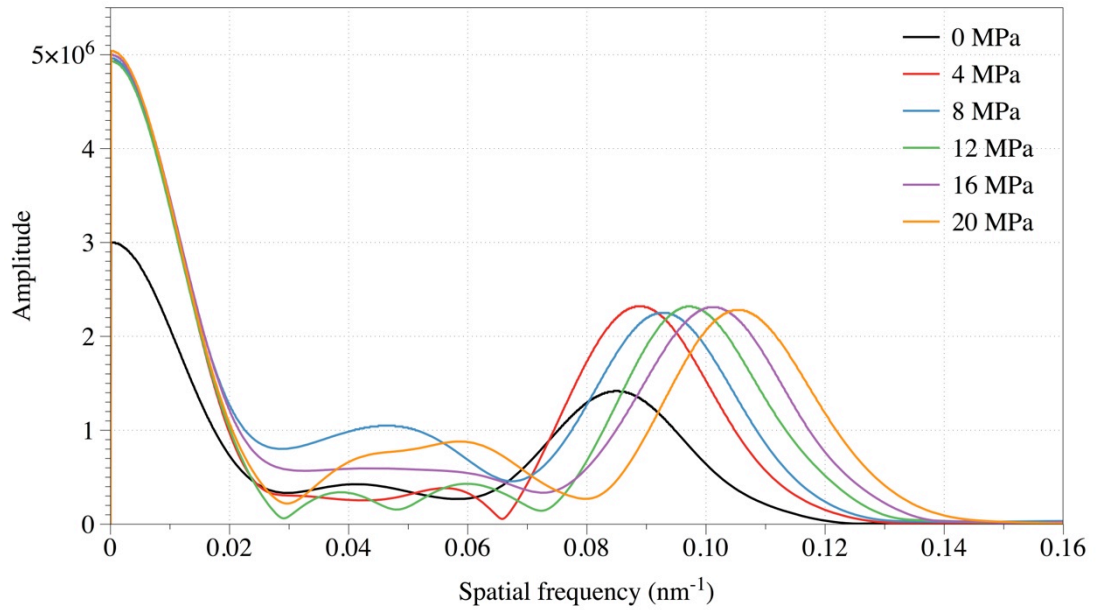


Figure 5.7. Spatial frequency spectrum of the 38 cm sensor at different pressure value. (Low frequencies components only)

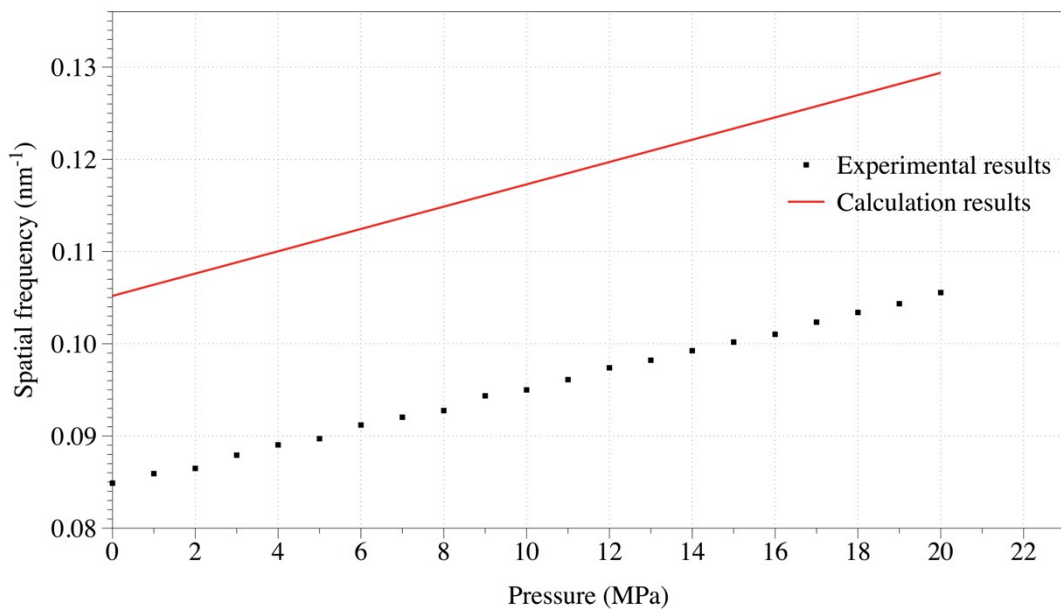


Figure 5.8. Experimental and calculation results of the 38 cm long sensor's frequency shift

Figure 5.7 shows the spatial frequency spectrum of the 38 cm long sensor. The peak spatial frequency gradually shifts to the higher side while the pressure increase. Figure 5.8 shows the sensor's peak spatial frequency change against pressure. The experimental data show a linear relationship with pressure. The calculated result shows similar linear relationship but there is an offset in the spatial frequency values.

This could be due to the variation in the differences in the group birefringence between the sample of the PM-PCF and the value used for calculations, which are obtained from [59]. By obtaining the spatial frequency of the sensor, the group birefringence can be found by applying equation (5.13). Figure 5.9 shows the group birefringence of the 38 cm and 68.8 cm long sensor obtained by the FFT method and equation (5.13). The two sensor gives similar response. The benefits of using the spatial frequency or the group birefringence to measure pressure change is that the range is not bounded by the bandwidth of the light source. But according to Figure 5.9, the data points are not as linear as the spectral shift method, which results in larger error.

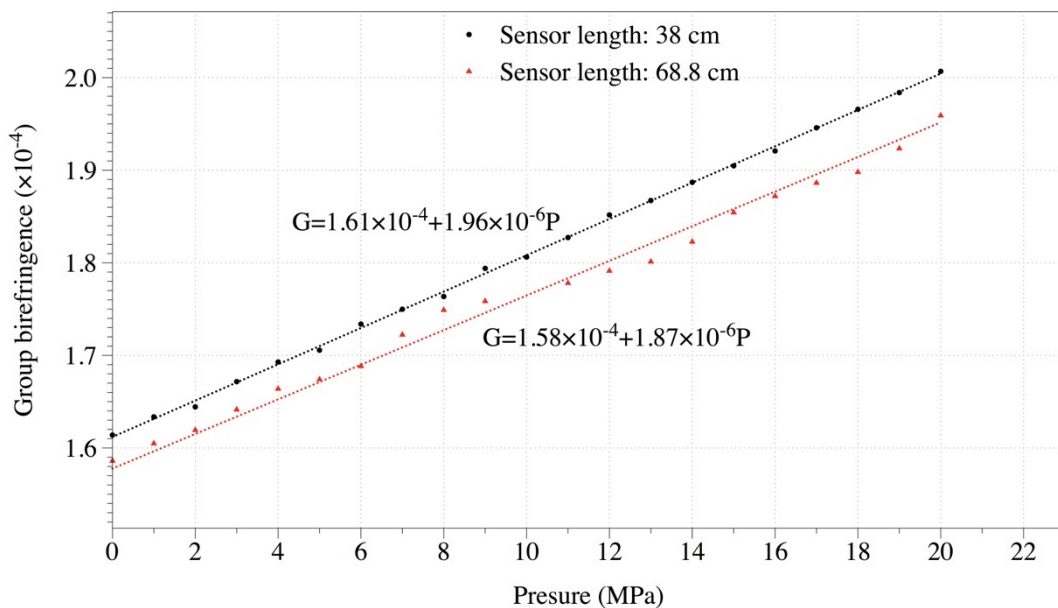


Figure 5.9. Group birefringence of the 38 cm and the 68.8 cm long sensor at different applied pressure

Doing FFT to the data points not only yield the peak spatial frequency, but also phase. The phase of the peak spatial frequency is calculated by finding the two nearest integer valuea of the spatial frequency and then uses the corresponding phase

values to do linear interpolation to obtain the value. Using the above process, Figure 5.10 can be obtained.

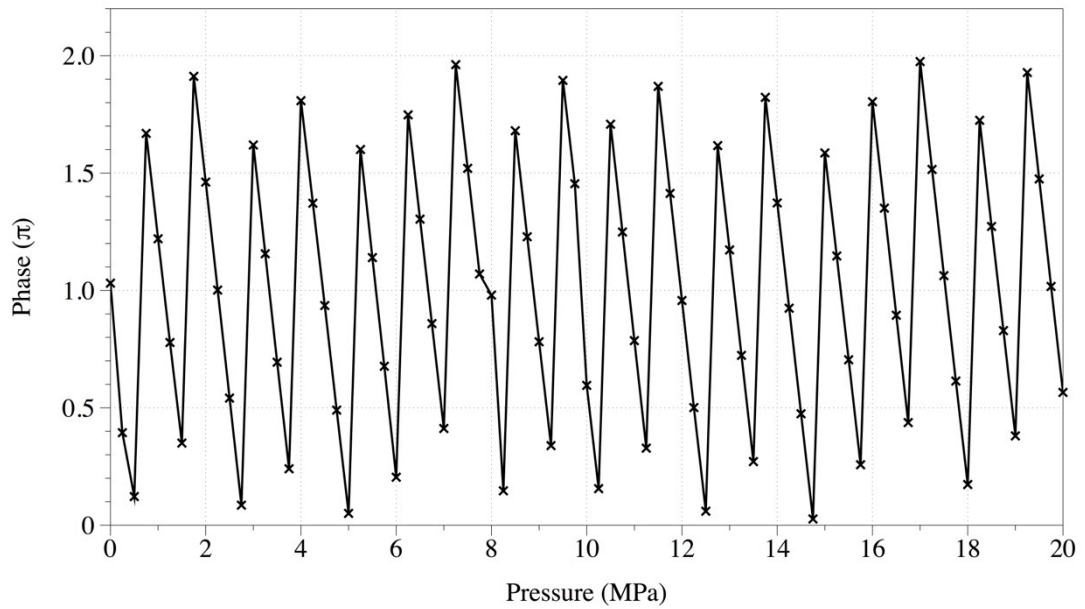


Figure 5.10. Phase shift of the 38 cm long sensor

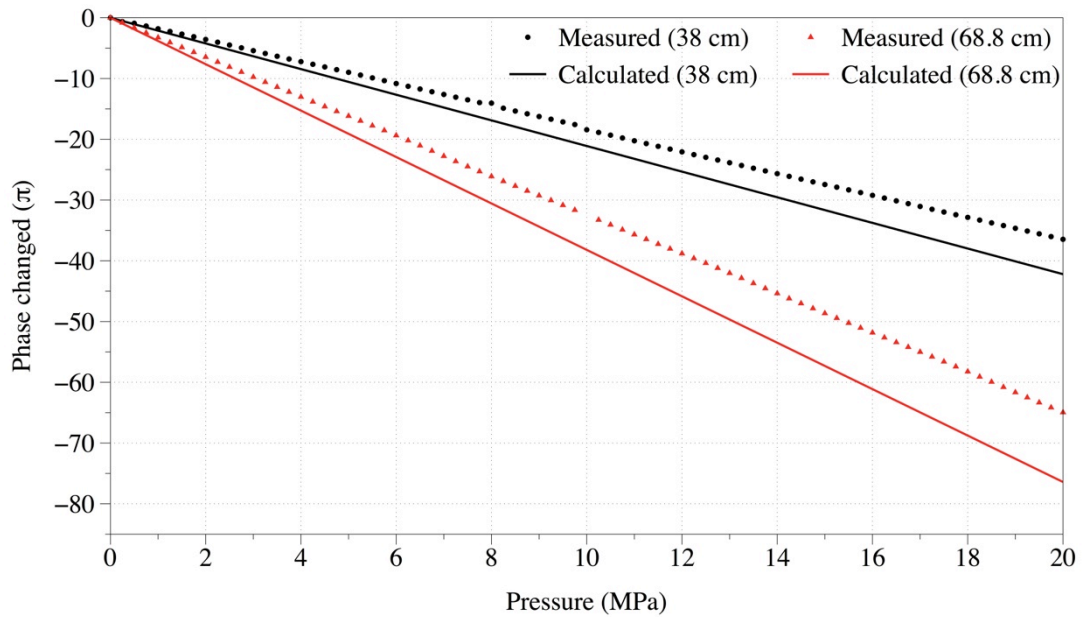


Figure 5.11. Experimental and calculated phase (concatenated) of the sinusoidal waveform at different pressure

Figure 5.10 shows the phase shift of the spectrum's sinusoidal like waveform of the 38 cm long sensor. The phases are within 0 and  $2\pi$ . Figure 5.11 shows the

accumulated phase change of the 38 cm and the 68.8 cm long sensor. Phase decreases as pressure increases and increases as pressure decreases. For calculation using equation (5.11) with values from [59], the pressure sensitivity of the 38 cm long sensor is  $-2.11\pi$  rad/MPa and for the 68.8 cm long sensor is  $-3.82\pi$  rad/MPa. The measured pressure sensitivity of the 38 cm sensor is  $-1.82\pi$  rad/MPa and is  $-3.24\pi$  rad/MPa for the 68.8 cm sensor. Using the measured results and equation (5.11), the linear relationship between birefringence and pressure,  $\Delta B/\Delta P$ , of the 38 cm and 68.8 cm long sensors are found to be  $2.04 \times 10^{-6}$  and  $2.00 \times 10^{-6}$  respectively. The phase change method is capable to offer unlimited measuring range if the rate of change of pressure is not very rapid. For the 38 cm long sensor, a  $\pi$  change in phase represents 0.55 MPa pressure range. As the rate of the optical fibre interrogator is 250 Hz, the pressure fluctuation rate that would cause phase ambiguity is  $0.55 \times 250 = 137.5$  MPa/s. For the 68.8 cm long sensor, the rate that cause phase ambiguity is  $0.31 \times 250 = 77.5$  MPa/s. These pressure fluctuation rates are extremely high and extremely rare in real applications.

Figure 5.12 shows the standard deviation of the two sensors' experimental results obtained by the two measurement methods. The spectral shift and phase shift methods show similar accuracy except in the range 4.25-5.25 MPa the spectral shift method of the 38 cm sensor is much worse than the phase shift method. For all the data samples obtained, the spectral shift and phase shift worst-case accuracy of the 38 cm long sensor is  $\pm 3.47$  KPa and  $\pm 0.67$  KPa respectively. The spectral shift and phase shift worst-case accuracy of the 68.8 cm long sensor is  $\pm 0.47$  KPa and  $\pm 0.4$  KPa respectively. The results indicate that phase shift method shows slightly better accuracy than the spectral shift method. As the pressure sensitivity of the phase shift method is linear, at least up to the tested pressure range, while the spectral shift

method require monitoring of different peaks with different sensitivity, the phase shift method outperforms the spectral shift method when measuring over a wide pressure range.

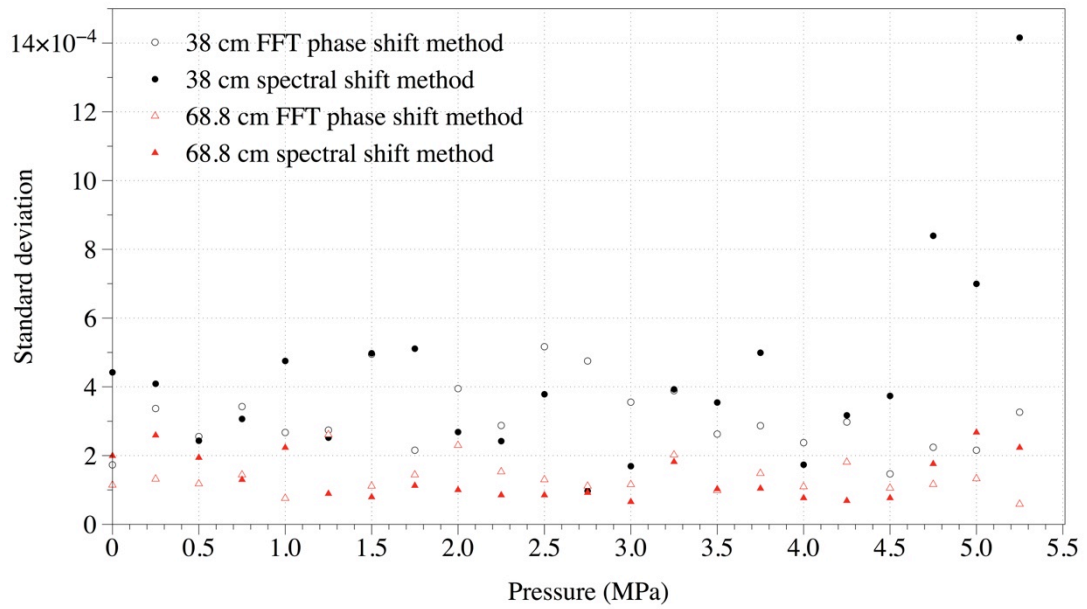


Figure 5.12. Standard deviation of the measured samples by spectral shift and phase shift method

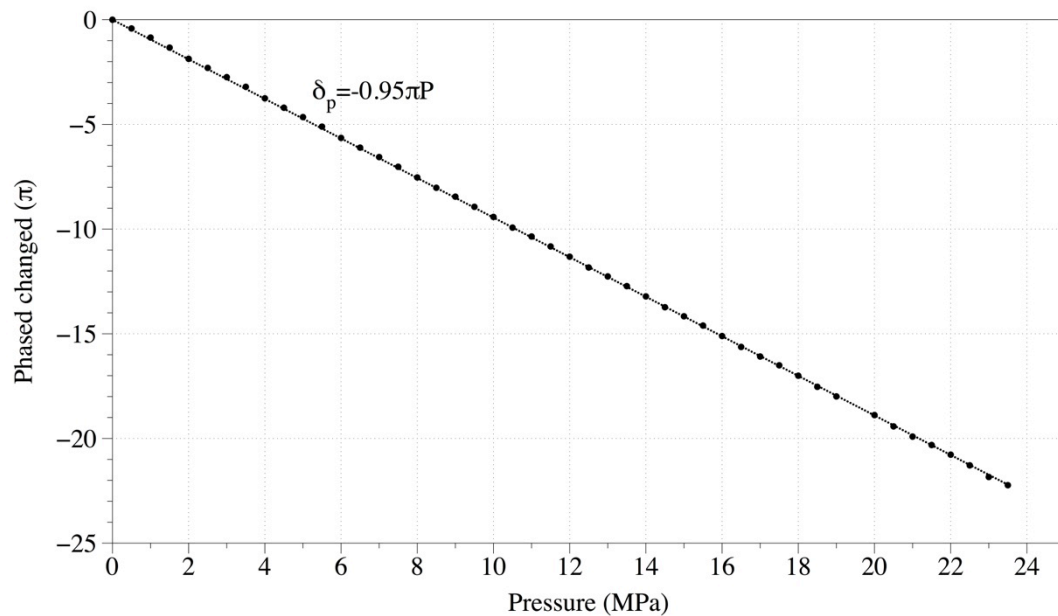


Figure 5.13. Phase change of the 38 cm long sensor working at 1550 nm

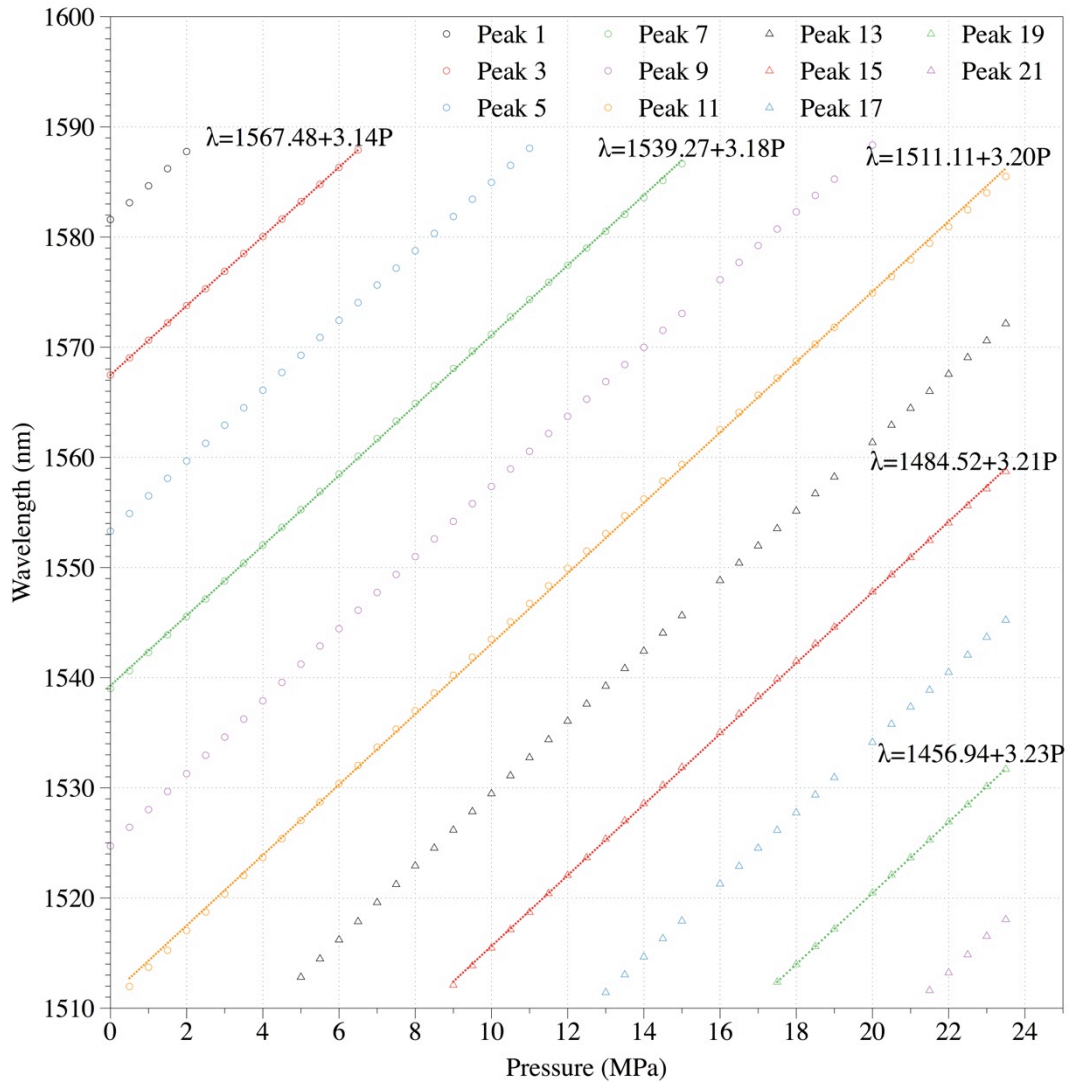


Figure 5.14. Peaks shift of the 38 cm PM-PCF Sagnac loop pressure sensor working at 1550 nm

Further study of the phase shift method was done by moving the sensor's operating wavelength to 1550 nm. The length of the PM-PCF used was about 38 cm. According to [59], the birefringence and pressure relationship  $\Delta B/\Delta P$  at both 850 nm and 1550 nm are similar. So, using  $\Delta B/\Delta P=2.00 \times 10^{-6}$  and put into equation (5.11) gives the estimated pressure sensitivity at 1550 nm to be  $-0.98\pi$  rad/MPa. In the experiment, a Micron Optics, Inc. SM125-500 optical fibre interrogator with scanning frequency of 2 Hz was used. Figure 5.13 shows the concatenated phase change of the 38 cm long sensor at 1550 nm. The measured sensitivity is  $0.95\pi$

rad/MPa, which is very close to the estimated sensitivity. The figure also shows linear phase change throughout the whole experimented pressure range. Figure 5.14 shows the peaks shift of the spectral shift method. As the same in the experiments at 850 nm, different peaks are required to be monitor in order to have a wide operation range. Different peaks have different pressure sensitivity, which will affect the reliability of the sensor if a wide pressure range is measured.

To compare the accuracy of the two methods at 1550 nm, 10 samples were taken at 0 MPa. Results are shown in Figure 5.15. The accuracy of the spectral shift and phase shift method are  $\pm 6.11$  KPa and 3.77 KPa respectively. The accuracy of the phase shift method is slightly better than the spectral shift method, but worse than operation at 850 nm.

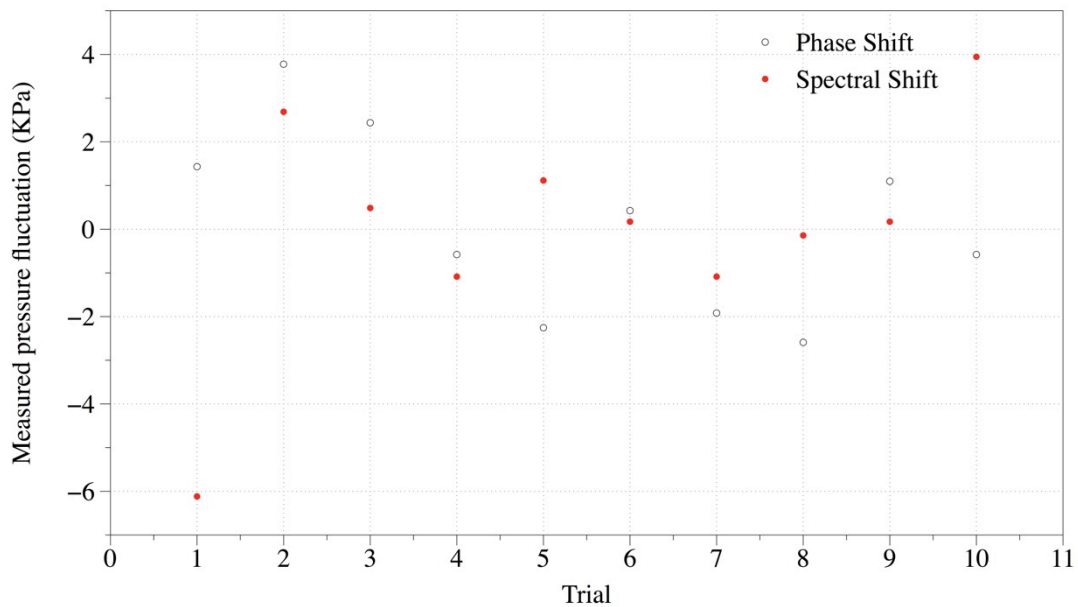


Figure 23. comparison of the measured pressure fluctuation of the sensor at 1550 nm by the two methods

## **5.5 Conclusions**

A new method to extend the measuring range and enhance the accuracy of the PM-PCF based Sagnac loop pressure sensor was introduced. By measuring the phase change of the optical fibre interrogator's output sinusoidal like wavelength spectrum, the measuring range can be extended and experiments show a slight improvement in accuracy when compared to the spectral shift method. The problem of the spectral shift method in measuring wide pressure range is that each peak has limited pressuring range caused by the bandwidth of the light source. Measuring wide pressure range requires monitoring of different peaks at different pressure range. But as shown in the experimental results, different peaks have different pressure sensitivity. So, the spectral shift method cannot provide a very reliable result. On the other hand, the phase shift method shows linear relationship between the phase and the pressure throughout the whole measuring range. The results of different sensor length or operation wavelength all show linear relationship. This linear pressure sensitivity gives the sensor a very wide operation range.

# Chapter 6

## Conclusions & Future work

### 6.1 Conclusions

Flow and pressure measurement are essential in many different applications including oil and gas industry. The use of traditional electronic based sensors is often limited in harsh environment. To tackle the problem caused by the challenging working conditions, optical fibre based sensors can be used. Optical fibre sensors offer benefits like insensitive to EMI, high working temperature, the ability to withstand high pressure and very low attenuation. These characteristics make optical fibre sensor an ideal candidate for harsh working environment in oil and gas industry where the pressure and temperature are both high and often the sensors are located far away from the measuring devices.

In this thesis, two types of fibre optic sensors were studied, flowmeter and pressure sensor. Both of the sensors are based purely silica fibre without any extra metal, which could be corroded when exposed to certain kind of chemicals.

The flowmeter presented is based on the principle of convective heat transfer, in which the change in fluid's flow rate affect the temperature of the sensor. The physical construction of the sensor is just a piece of optical fibre. The optical fibre itself converts the optical energy carried inside it into thermal energy. FBG is inscribed on the fibre to measure the temperature change. Two operation modes were proposed, constant power and pulsed operation. Constant power is the operation mode used in traditional electric based thermal anemometer. However, its operation depend on absorbed pump power and ambient temperature. Calibration and

temperature monitoring are necessary for the proper operation of the sensor. The second proposed mode of operation, the pulsed operation, was not reported in traditional electric based thermal anemometer. The study in the thesis has shown that this operation mode can help to reduce ambient and power dependency of the sensor.

The proposed fibre optic thermal anemometer in constant power mode was studied experimentally and theoretically. The experimental sensor system is based on a 5 mm section of cobalt doped high attenuation fibre. FBG is inscribed in the sensing fibre to sense the temperature change. The high absorption fibre absorbs the 1455 nm pumping laser light and converts the optical energy to thermal energy. When the airflow speed is zero, the temperature of the sensor can reach nearly 600 °C with 330 mW absorbed power. Experiments at different absorbed power were conducted to measure the response of the sensor and the results were fit with equation (3.1). The sensitivity of the sensors were found to decrease when the flow speed increases.

Equation (3.1) is based on the empirical results obtained from experiments. In order to estimate sensor's response with physical parameters, equations that use physical parameters of the sensor's material and the measuring fluid were developed. The benefit of having these equations is that the response of sensors of different design can be estimated before it is being built. Simulation results based on the developed equations were compared with experimental results and they agree well with each other, indicating the validity of the equations. The sensitivity of the sensors was found to be sensitive to the absorbed power and the outer diameter of the fibre. Both simulation and experimental results prove that the core diameter does not contribute to sensitivity significantly. Increase in core diameter by ~502 % cause the sensitivity to increase only by ~0.5 %.

The possibility of using the sensor for water flow measurement was investigated experimentally. The sensor structure is basically the same as that used in airflow measurement except that an extra tiny silica tube that enclose the high absorption fibre is included. This protects the fibre from the strain caused by the flowing water. The results shows much lower sensitivity than that obtained airflow measurement. This is due to the larger outer diameter (the silica tube) and the high thermal conductivity of the target fluid.

Experiments indicated the measured temperature is dependent not only on flow speed, but also on the absorbed power and ambient temperature. Fluctuation in the later two factors is common and need to be tackled. Pulsed operation is proposed to reduce the sensor's sensitivity to ambient temperature and laser power fluctuation. In the proposed pulsed operation, the pump laser output power is modulated on and off. The temperature of the sensor rises when the pump laser output is on and the temperature drops when the laser output is off. The time constant of the falling temperature is used to calculate the actual airflow speed. Equations were developed and the calculation results were compared with the experimental results. Results agree well with each other and the experimental results also indicate a very slight absorbed power dependency when compared to the constant power operation.

Another experiment was conducted to evaluate the ability of serially multiplexing the sensors. Three sensors were serially multiplexed. Two of them were placed in the wind tunnel and one was kept in an enclosed box. The FBGs inscribed in the sensors were all around 850 nm. The reason of using FBGs around 850 nm instead of 1550 nm is that the attenuation of the high absorption fibre is much smaller at wavelengths around 850 nm. The two sensors kept in the wind tunnel had different level of absorbed power but their responses were close to each other and agreed with the

calculated results. The sensor, which was kept in the enclosed box, showed no significant relationship to the other two sensors. These experiments and calculations show that the pulsed operation can reduce the sensor's dependency on pump power and also ambient temperature fluctuation.

The pressure sensor studied in the thesis is based on the Sagnac interferometer and is also purely optical fibre based. For downhole pressure measurement, the sensors are usually placed deep underground and very far away from the measuring device and the pressure and temperature are often high, optical fibre is an ideal candidate. When hydrostatic pressure varies, the birefringence of the optical fibre used changes. A CCD based optical fibre interrogator is used for spectral reading. Variation in group birefringence results in spectral shift. Measurement of spectral shift tells the pressure variation. Another method that measures the phase change of the sinusoidal spectrum of the sensor was proposed. The purpose of this measurement method is to extend the measurement range.

A pressure sensor that offers improved sensitivity and extend measuring range is studied experimentally. The pressure sensor's is based on a Sagnac loop configuration using Blaze Photonics PM-1550-01 PM-PCF. The physical construction is similar to the one reported in [62] but the operation wavelength is changed to around 850 nm. This movement in wavelength enables the use of CCD based optical fibre interrogator. The benefits of using CCD based optical fibre interrogator is that the measurement speed is high and cost is low comparing with 1550 nm operation. A new method is proposed that can extend the measurement range comparing with the previously proposed schemes. The full transmission spectrum of the sensor is used. The spectrum is a sinusoidal like waveform. FFT is applied to the waveform and the peak frequency and the corresponding phase is

founded. The phase change of the sinusoidal like waveform is used to measure the pressure variation. Equations were developed to estimate the response. According to the equations, the pressure sensitivity of sensor is constant, which means it is unrelated to the applied pressure. Unlike the spectral shift method, experimental results show that different spectral peaks have different sensitivity and each peak has a limited pressure range. The experimental results of the proposed phase measuring method shows constant pressure sensitivity up to 20 MPa, which is the maximum pressure applied in the experiment. The accuracy of the two sensors based on phase shift method has been shown to be better than that obtained using spectral shift method for the same sensors. The results indicate that the propose phase shift method has an extended measuring range and also a slightly better accuracy.

The proposed flow sensors and pressure sensors were tested at a wavelength of 850 nm. This suggests that instead of using a different measuring system, the 2 sensors can both be measured by using the same interrogator. This is a benefit in applications like crude oil extraction where you need to measure the flow of the injected superheated steam while measuring the pressure of the crude oil.

## **6.2 Future work**

The flow sensor presented in the thesis can be used for harsh working conditions. It also offers reduced pump laser power and ambient temperature sensitivity comparing with previous proposed schemes. Future work on flow sensitivity improvement is recommended. According to the equations developed, the sensitivity of the sensor is related to the outer diameter. One way to increase the flow sensitivity of the sensor is to reduce the outer diameter of the sensing fibre. Another way to increase the sensitivity is to increase the absorbed power. The emitting area of high power lasers

is often large. Methods to increase the amount of optical power that can be coupled to the sensing fibre, like modification of the structure, worth investigation. High absorbed power would be useful in measuring fluid with high thermal conductivity like water.

In chapter 3 and 4, constant power and pulse operation were introduced. Pulse operation offers less pump power and ambient temperature dependency. But this comes at a cost that the measurement time required is longer than constant power operation. This means that operation is capable in average flow speed measurement but not the instant flow speed as in constant power operation. It would be worth testing a hybrid system that combines the two operation methods. This might enjoy the benefits of both operation modes.

The pressure sensor proposed in chapter 5 shows good sensitivity and wide measuring range. The pressure range tested was up to 20 MPa. It is worth experimenting with the pressure range to about 100 MPa, which a conventional pressure sensor is capable. Further work on multiplexing is recommended. Multiplexing of the sensors while maintaining the measurement accuracy is essential in industrial use. Studies and experiments on techniques that can maintain measurement accuracy while increasing the number of sensors to be multiplexed in the system should help significantly increase the application areas of the pressure sensor systems.

Another possible exploration is the use of polymer fibre to replace the silica fibre. Generally, polymer materials have smaller Young's modulus than silica, which means the deformation of the fibre structure due to the applied hydrostatic pressure is more pronounced. This should give even higher pressure sensitivity than silica.

## References

- [1] T. Erdogan, "Fiber Grating Spectra," *J. Lightwave Technol.*, vol. 15, pp.1277-1294, 1997.
- [2] K. O. Hill, Y. Fujii, D. C. Johnson, B. S. Kawasaki, "Photosensitivity in Optical Waveguides: Application Filter Fabrication," *Appl. Phys. Lett.*, vol 32, pp.647-649, 1978.
- [3] K. O. Hill, "Photosensitivity in Optical Fiber Waveguides: From Discovery to Commercialization," *IEEE J. Sel. Top. Quant. Electron.*, vol. 6, pp. 1186-1189, 2000.
- [4] G. Meltz, W. W. Morey, W. H. Glenn, "Formation of Bragg Gratings in Optical Fiber By a Transverse Holographic Method," *Opt. Lett.*, vol. 15, pp. 823-825, 1989.
- [5] K. O. Hill, B. Malo, F. Bilodeau, D. C. Johnson, J. Albert, "Bragg Gratings Fabricated in Monomode Photosensitive Optical Fiber By UV Exposure Through a Phase Mask," *Appl. Phys. Lett.*, vol. 62, pp.1035-1037, 1993.
- [6] D. K. W. Lam, B. K. Garside, "Characterization of single mode optical fiber filters," *Appl. Opt.*, vol. 20, pp. 440-445, 1981.
- [7] A. Othonos, K. Kalli, "Photosensitivity in Optical Fibers," in *Fiber Bragg Gratings: fundamentals and applications in telecommunications and sensing*, Norwood, MA: Artech House, Inc., 1999, pp.9-16.
- [8] P. J. Lemaire, R. M. Atkins, V. Mizrahi, W. A. Reed, "High pressure H<sub>2</sub> loading as a technique for achieving ultrahigh UV photosensitivity and Thermal Sensitivity in GeO<sub>2</sub> doped optical fibres," *Electron. Lett.*, vol. 29, pp. 1191-1193, 1993.

- [9] J. Albert, B. Malo, F. Bilodeau, D. C. Johnson, K. O. Hill, Y. Hibino, M. Kawachi, "Photosensitivity in Ge-doped silica optical waveguides and fibers with 193-nm light from an ArF excimer laser," *Opt. Lett.*, vol. 19, pp. 387-389, 1994.
- [10] B. Malo, D. C. Johnson, F. Bilodeau, J. Albert, K. O. Hill, "Single-excimer-pulse writing of fiber gratings by use of a zero-order nulled phase mask: grating spectral response and visualization of index perturbations," *Opt. Lett.*, vol. 18, pp. 1277-1279, 1993.
- [11] L. Dong, W. F. Liu, L. Reekie, "Negative-index gratings formed by a 193-nm excimer laser," *Opt. Lett.*, vol. 21, pp. 2032-2034, 1996.
- [12] A. Othonos, K. Kalli, "Properties of Fiber Bragg Gratings," in *Fiber Bragg Gratings: fundamentals and applications in telecommunications and sensing*, Norwood, MA: Artech House, Inc., 1999, pp. 96-99.
- [13] A. D. Kersey, M. A. Davis, H. J. Patrick, M. LeBlanc, K. P. Koo, C. G. Askins, M. A. Putnam, E. J. Friebele, "Fiber Grating Sensors," *J. Lightwave Technol.*, vol. 15, pp. 1442-1463, 1997.
- [14] T. Erdogan, V. Mizrahi, P. J. Lemaire, D. Monroe, "Decay of ultraviolet-induced fiber Bragg gratings," *J. Appl. Phys.*, vol. 76, pp. 73-80, 1994.
- [15] S. Kannan, J. Z. Y. Guo, P. J. Lemaire, "Thermal stability analysis of UV-induced fiber Bragg gratings," *J. Light. Technol.*, vol. 15, pp. 1478-1483, 1997.
- [16] J. E. Hardy, J. O. Hylton, T. E. McKnight, C. J. Remenyik, F. R. Ruppel, "General concepts of flow and flow instrumentation," in *Flow measurement methods and applications*, New York, NY: John Wiley & Sons, Inc., 1999, pp. 1-26.

- [17] A. T. J. Hayward, "Differential pressure meters," in *Flowmeters: A basic guide and source-book for users*, London, United Kingdom: The Macmillan Press Ltd., 1979, pp. 33-43.
- [18] C. Gulaga. Vortex Shedding Meters. CB Engineering Ltd. Calgary, Alberta, Canada. [online] Available: [www.cbeng.com/resources/whitepaper/vortexmetersforgas.pdf](http://www.cbeng.com/resources/whitepaper/vortexmetersforgas.pdf)
- [19] R. C. Baker, "Volumetric flowmeters," in *An introductory guide to flow measurement*, London, United Kingdom: Professional Engineering Publishing Ltd., 2002, pp. 72-108.
- [20] V. Hans, H. Windorfer, "Comparison of pressure and ultrasound measurements in vortex flow meters," *Measurement*, vol. 33, pp. 121-133, 2003.
- [21] A. T. J. Hayward, "Rotating mechanical meters," in *Flowmeters: A basic guide and source-book for users*, London, United Kingdom: The Macmillan Press Ltd., 1979, pp. 53-55.
- [22] A. T. J. Hayward, "Other volumetric flowmeters," in *Flowmeters: A basic guide and source-book for users*, London, United Kingdom: The Macmillan Press Ltd., 1979, pp. 68-87.
- [23] P. Freymuth, "History of thermal anemometry," in *Handbook of fluids in motion*, Ann Arbor, MI: Ann Arbor Science Publishers, 1983, pp.79-91
- [24] A. E. Kennelly, C. A. Wright, J. S. Van Bylevelt, "The convection of heat from small copper wires," *Trans. Am. Inst. Elect. Eng.*, vol. 28, pp. 363-393, 1909.

- [25] L. M. Fingerson, "Thermal anemometry, current state, and future directions," *Rev. Sci. Instrum.*, vol. 65, pp. 285-300, 1994.
- [26] L. V. King, "On the convection of heat from small cylinders in a stream of fluid: Determination of the convection constants of small platinum wires with applications to hot-wire anemometry," *Phil. Trans. R. Soc. Lond. A*, vol. 90, pp. 563-570, 1914.
- [27] J. R. Weske, "A hot-wire circuit with very small time lag," NACA Tech. Note 881, Feb. 1943.
- [28] C. G. Lomas, "Electronic circuitry," in *Fundamentals of hot wire anemometry*, Cambridge, United Kingdom: Cambridge University Press, 1986, pp. 84-98.
- [29] H. H. Brunn, "Basic principles of hot-wire anemometry," in *Hot-wire anemometry: Principles and signal analysis*, Oxford, United Kingdom: Oxford University Press, 1995, pp.19-70.
- [30] Y. Yeh, H. Z. Cummins, "Localized fluid flow measurements with He-Ne laser spectromeyer," *Appl. Phy. Let.*, vol. 4, pp. 176-178, 1964.
- [31] R. J. Adrian, R. J. Goldstein, "Analysis of a laser Doppler anemometer," *J. Phys. E: Sci. Instrum.*, vol. 4, pp. 505-511, 1971.
- [32] J. Knuhtsen, E. Olldag, P. Buchhave, "Fibre-optic laser Doppler anemometer with Bragg frequency shift utilizing polarisation-preserving single-mode fibre," *J. Phys. E: Sci Instrum.*, vol. 15, pp. 1188-1191

- [33] W. Peng, G. R. Rickrell, Z. Huang, J. Xu, D. W. Kim, B. Qi, A. Wang, "Self-compensating fiber optic flow sensor system and its field applications," *Appl. Opt.*, vol. 43, pp. 1752-1760, 2004.
- [34] P. Lu, Q. Chen, "Fiber Bragg grating sensor for simultaneous measurement of flow rate and direction," *Meas. Sci. Technol.*, vol 19, pp. 1-8, 2008.
- [35] J. H. Lyle, C. W. Pitt, "Vortex shedding fluid flowmeter using optical fibre sensor," *Electron. Lett.*, vol. 17, pp. 244-245, 1981.
- [36] J. S. Barton, M. Saoudi, "A fibre optic vortex flowmeter," *J. Phys. E: Sci. Instrum.*, vol. 19, pp. 64-66, 1986.
- [37] S. Webster, R. McBride, J. S. Barton, J. D.C. Jones, "A passive signal processing technique for monomode fibre optic vortex shedding flowmeters," *Meas. Sci. Technol.*, vol. 2, pp. 223-228, 1991.
- [38] L. K. Cheng, W. Schiferli, R. A. Nieuwland, A. Franzen, J. J. den Boer, T. H. Jansen, "Development of a FBG vortex flow sensor for high-temperature applications," in *Proc. of SPIE*, vol. 7753, pp. 77536V-1 – 77536V-4, May 2011.
- [39] S. R. Philip, "Fiber optic thermal anemometer," U.S. Patent 4 621 929, Nov. 11, 1986.
- [40] L. C. Bobb, J. P. Davis, A. Samouris, D. C. Larson, "An optical fiber hot-wire anemometer," in *Proc. of SPIE*, vol. 567, Feb. 1990.
- [41] D. W. Lamb, G. A. Woolsey, "Characterization and use of an optical fiber interferometer for measurement of electric wind," *Appl. Opt.*, vol. 34, pp. 1608-1616, 1995.

- [42] K. P. Chen, B. McMillen, M. Buric, C. Jewart, W. Xu, "Self-heated fiber Bragg grating sensors," *Appl. Phys. Lett.*, vol. 80, pp. 143502-1 – 143502-3, 2005.
- [43] C. Jawart, B. McMillen, S. K. Cho, K. P. Chen, "X-probe flow sensor using self-heating active fiber Bragg gratings," *Sens. Actuators A*, vol. 127, pp. 63-68, 2006.
- [44] P. Caldas, P. A. S. Jorge, G. Rego, O. Frazão, J. L. Santos, L. A. Ferreira, F. Araújo, "Fiber optic hot-wire flowmeter based on a metallic coated hybrid long period grating/fiber Bragg grating structure," *Appl. Opt.*, vol. 50, pp. 2738-2743
- [45] M. K. Davis, M. J. F. Digonnet, R. H. Pantell, "Thermal effects in doped fibers," *J. Lightwave. Technol.*, vol. 16, pp. 1013-1023, 1998.
- [46] M. K. Davis, M. J. F. Digonnet, "Measurements of thermal effects in fibers doped with cobalt and vanadium," *J. Lightwave. Technol.*, vol. 18, pp. 161-165, 2000.
- [47] B. Culshaw, "The optical fibre Sagnac interferometer: an overview of its principles and applications," *Meas. Sci. Technol.*, vol. 17, no. 1, pp. R1-R16, Jan 2006.
- [48] V. Vali, R. W. Schorthill, "Fiber ring interferometer," *Appl. Opt.*, vol. 15, pp. 1099-1100, 1976.
- [49] J. Blake, P. Tantaswadi, R. T. de Carvalho, "In-line Sagnac interferometer current sensor," *IEEE Trans. Power Deli.*, vol. 11, pp. 116-121, 1996.
- [50] Y. Liu, B. Liu, X. Feng, W. Zhang, G. Zhou, S. Yuan, G. Kai, X. Dong, "High-birefringence fiber loop mirrors and their applications as sensors," *Appl. Opt.*, vol. 44, pp. 2382-2390, 2005.

- [51] G. B. Hocker, "Fiber-optic sensing of pressure and temperature," *Appl. Opt.*, vol. 18, pp. 1445-1448, 1979.
- [52] Y. Zhao, Y. Laio, S. Lai, "Simultaneous measurement of down-hill high pressure and temperature with a bulk-modulus and FBG sensor," *IEEE. Photon. Technol. Lett.*, vol. 14, pp. 1584-1586, 2002.
- [53] Y. Zhu, A. Wang, "Miniature fiber-optic pressure sensor," *IEEE Photon. Technol. Lett.*, vol. 17, pp. 447-449, 2005.
- [54] S. H. Aref, H. Latifi, M. I. Zibaii, M. Afshari, "Fiber optic Fabry-Perot pressure sensor with low sensitivity to temperature changes for downhole application," *Optics Commun.*, pp. 322-330, 2007.
- [55] Z. Ran, Z. Liu, Y. Rao, F. Xu, D. Sun, X. Yu, B. Xu, J. Zhang, "Miniature fiber-optic tip high pressure sensors micromachined by 157 nm laser," *IEEE. Sens. J.*, vol. 11, pp. 1103-1106, 2011.
- [56] W. J. Bock, A. W. Domański, "High hydrostatic pressure effects in highly birefringent optical fibers," *J. Lightwave Technol.*, vol. 7, pp. 1279-1283, 1989.
- [57] K. S. Chiang, "Pressure-induced birefringence in a coated highly birefringent optical fibre," *J. Lightwave Technol.*, vol. 8, pp. 1850-1855, 1990.
- [58] A. N. Starodumov, L. A. Zenteno, D. Monzon, E. De La Rosa, "Fiber sagnac interferometer temperature sensor," *Appl. Phys. Lett.*, vol. 70, pp. 19-21, 1997.
- [59] M. Szpulak, T. Martynkien, W. Urbańczyk, "Effects of hydrostatic pressure on phase and group modal birefringence in microstructured holey fibers," *Appl. Opt.*, vol. 43, pp. 4739-4744, 2004.

- [60] G. Statkiewicz, T. Martynkien, W. Urbańczyk, “Measurements of modal birefringence and polarimetric sensitivity of the birefringent holey fiber to hydrostatic pressure and strain,” *Opt. Commun.*, vol. 241, pp.339-348, 2004.
- [61] T. Martynkien, G. Statkiewicz-Barabach, J. Olszewski, et. al, “Highly birefringent microstructured fibers with enhanced sensitivity to hydrostatic pressure,” *Opt. Express*, vol. 18, pp. 15113-15121, 2010.
- [62] H. Y. Fu, H. Y. Tam, L. Y. Shao, X. Dong, P. K. A. Wai, C. Lu, S. K. Khijwania, “Pressure sensor realized with polarization-maintaining photonic crystal fiber-based Sagnac interferometer,” *Appl. Opt.*, vol. 47, pp. 2835-2839, 2008.
- [63] H. Y. Fu, C. Wu, M. L. V. Tse, L. Zhang, K. C. D. Cheng, H. Y. Tam, B. Guan, C. Lu, “High pressure sensor based on photonic crystal fiber for downhole application,” *Appl. Opt.*, vol. 49, no. 14, pp. 2639-2643, May 2010.
- [64] P. C. Schultz, “Optical absorption of the transition elements in vitreous silica,” *J. Am. Ceram. Soc.*, vol. 57, pp. 309-313, 1974.
- [65] F. P. Oncropera, D. P. Dewitt, T. L. Bergman, A. S. Lavine, “The heat diffusion equation,” in *Introduction to Heat Transfer*. New York, NY: John Wiley & Sons, Inc., 2011, pp. 68-109.
- [66] S. W. Churchill, M. Bernstein, “A correlating equation for forced convection from gases and liquids to a circular cylinder in crossflow,” *J. Heat Transfer*, vol. 99, pp. 300-306, May. 1977.
- [67] A. Sugawara, “Precise determination of thermal conductivity of high purity fused quartz from 0° to 650°C,” *Physica*, vol. 41, no. 3, Mar. 1969.

- [68] F. P. Oncropera, D. P. Dewitt, T. L. Bergman, A. S. Lavine, "Transient Conduction," in *Introduction to Heat Transfer*. New York, NY: John Wiley & Sons, Inc., 2011, pp. 280-376.
- [69] D. B. Mortimore, "Fiber loop reflectors," *J. Lightw. Technol.*, vol. 6, no. 7, pp. 1217-1224, July 1988.
- [70] A. Michie, J. Canning, K. Lyytikäinen, M. Åslund, and J. Digweed, "Temperature independent highly birefringent photonic crystal fibre," *Opt. Express*, vol. 12, no. 21, pp. 5160-5165, Oct. 2004.
- [71] D. H. Kim and J. U. Kang, "Sagnac loop interferometer based on polarization maintaining photonic crystal fibre with reduced temperature sensitivity," *Opt. Express*, vol. 12, no. 19, pp. 4490-4495, Sep. 2004.
- [72] X. Dong, H. Y. Tam, and P. Shum, "Temperature-insensitive strain sensor with polarization-maintaining photonic crystal fibre based Sagnac interferometer," *Appl. Phys. Lett.*, vol. 90, no. 15, 1511130, Apr. 2007.